Studies on the Solar Chromospheric Network

A Thesis
Submitted for the Degree of
Doctor of Philosophy
in the Faculty of Science

By
R. Srikanth

DEPARTMENT OF PHYSICS
INDIAN INSTITUTE OF SCIENCE
BANGALORE – 560 012, INDIA

April 1998

DECLARATION

I hereby declare that the matter embodied in this thesis is the result of the investigations carried out by me at the Indian Institute of Science, Bangalore, and the Indian Institute of Astrophysics, Bangalore, under the supervision of Prof. Jagdev Singh and Prof. Som Krishan. This work has not been submitted for the award of any degree, diploma, associateship, fellowship, etc., of any other university or institute.

Candidate

R. Srikanth

(R. Srikanth)

Supervisors

(Prof. Jagdev Singh)

(Prof. Som Krishan)

Bangalore

Date: 27/4/98

Dedication:
for my Parents

MYSTIC RHYTHMS: *by* **RUSH**

So many things I think about
When I look far away
Things I know – things I wonder
Things I'd like to say
The more we think we know about
The greater the unknown
We suspend our disbelief
And we are not alone –

Mystic rhythms – capture my thoughts
And carry them away
Mysteries of night escape the light of day
Mystic rhythms – under northern lights
Primitive things stir
The hearts of everyone

We sometimes catch a window
A glimpse of what's beyond
Was it just imagination
Stringing us along?
More things than are dreamed about
Unseen and unexplained
We suspend our disbelief
And we are entertained

Mystic rhythms – capture my thoughts
And carry them away
Nature seems to spin
A supernatural way
Mystic rhythms – under city lights
Or a canopy of stars
We feel the powers and we wonder what they are
We feel the push and pull of restless rhythms from afar

PowerWindows

Contents

Acknowledgements

I am grateful to my thesis supervisor Prof. Jagdev Singh for guiding me to the thesis problem, and for his patient and helpful advice throughout my thesis work. I am thankful to Prof. Som Krishan for his kind help at various stages during my work. I thank Prof. G. Padmanabhan, Director, Indian Institue of Science, for the nice facilities at IISc. I thank Prof. Ramnath Cowsik, Director, Indian Institute of Astrophysics, for the nice facilities at IIA. I thank Mrs. Vagishwari, and Mrs. Christina Louis of IIA library.

Thanks are due to Dr. K. P. Raju for his valuable collaboration in many problems and for proof-reading my thesis draft. I thank Prof. M. H. Gokhale for suggesting that the lifetime-scale relationship of supergranules can be accounted for by a diffusion process. Prof. C. Sivaram's deep insight into a wide variety of fundamental physical problems has been a great inspiration to me. I thank Prof. K. R. Sivaraman and Prof. K. V. K. Iyengar for their kind encouragement.

I thank my friend Mangala Sharma for many useful discussions, not least the ones on the quantum mechanics of spooks! I am grateful to my friend B. S. Ramachandra, my discussions with whom on philosophy, physics and poetry provided me with much food for thought! My thanks to my friends Ramesh, Raghavan, Gurumurthy and Swathy Prabhu for the many profound philosophical discussions. I thank Jyotsna for sharing a lot of info on lingustics and poetry!

I thank Krishna, Sankar and Angom for enlivening discussions and for putting up with my excursions into philosphical exotica. Preeti's enthusiasm for X-files was a great filip to the scientific spirit! I thank also my friends Bhargavi, Geetanjali, Geetha, Sivarani, Swara, Nirmalya, Dharam, Rajguru and Sridharan for various talks.

My thanks are due to Sonjoy, Nayak, Pandey, and Jana. I thank also my friends Kabhi, Bagchi, Ramesh, Arun, Pavan and Partho.

Abstract

This thesis is a study of morphological and dynamical properties of the chromospheric network cells. It investigates how the size, lifetime and dynamics of cells are related to each other and to activity level. The data for the observations consisted of an almost uninterrupted time-series of Ca II K filtergrams obtained in 1989-1990 local summer in Antartica, and of spectroheliograms from Kodaikanal Solar Observatory.

Morphological properties of individual cells like size, shape and intensity contrast have been studied by visual inspection of individual cells. Shape of cells was quantified using the concept of area compactness of cells. It was found that smaller cells tend to have a regular polygonal or circular shape. We also found that the relative maximum contrast of intensity for larger cells tends to be greater. The mean intensity contrast in the cells is shown to be about 14%. The length-scale derived by direct inspection serves as a useful cross-check against estimates obtained by more complicated techniques like autocorrelation and tessellation.

Length-scales of network cells has been derived using the autocorrelation technique. The dependence of length-scales on latitude was studied using data from the Kodiakanal solar observatory spectroheliograms obtained during solar minima in the 1914-1974 period. The scales show a North-South symmetry. Under a wide-bin latitude averaging, there also emerges a poleward fall in cell sizes. A simple physical model is proposed to incorporate

both rotational and magnetic influence on cell sizes. Using peak width of the autocorrelation function as a measure of cell-wall thickness, we found that there was no correlation between thickness of walls and cell size.

Lifetime of cells was derived using cross-correlation technique. It is noted that the cross-correlation function does not fall monotonously, but is sometimes marked by small undulations, whose origins are as yet not clear. The influence of activity level on lifetimes was studied. We found that lifetimes are considerably longer near active regions. The cross-correlation and auto-correlation functions were used to estimate the diffusion rate of chromospheric fine-structures in quiet and enhanced network regions. The longer lifetimes near active regions is attributed to smaller diffusion rates in these regions.

The relationship between cell lifetimes and sizes has been studied using data obtained from 82 windows in the quiet Sun. The functional form of the relation has been determined by comparing the frequency functions of the two parameters. We found that lifetimes vary linearly with cell area, suggesting that diffusion process is responsible for the evolution of cells. The diffusion constant derived from this relation has been shown to be compatible with the diffusion rate for fluxtubes derived earlier.

The "steepest descent" algorithm has been used to tessellate the quiet chromosphere region. The algorithm minimizes the intensity I along the direction of the minimum gradient. The properties of the tiles derived in this manner have been studied. The geometric relation between these tiles and Ca K network is considered. It is shown that the tiles correspond not to cells but often to discrete mangetic elements.

Nomenclature

Abbreviation	Term
AC	autocorrelation
CC	cross-correlation
CN	chromospheric network
CNC	chromospheric network cell
FWHM	full width at half maximum
QS	quiet Sun
SG	supergranule
SM	Secondary maximum (of autocorrelation)

Chapter 1

Introduction

1.1 The Sun

The Sun, as is well known, is our nearest and dearest star: nearest, because at a mean distance of 1.496 $\times 10^8$ km, is closer than any other star; dearest because the supply of heat from the Sun, $\sim$ 1360 W m^{-2}, ultimately sustains and nourishes all biological life at Earth!

The Sun is a main sequence star, classified G2V, in the Hertzsprung-Russell diagram (Stix 1990). The primary source of luminosity in the Sun is Hydrogen burning. Table 1.1 summarizes some parameters of the Sun.

The T_{eff} of the Sun is obtained by fitting a black-body spectrum to the mean intensity $\bar{I}(\lambda)$. The spectrum is marked by many Fraunhofer (absorption) lines, especially on the blue side and beyond UV 3500Å. The red Hα (6563Å) (Labs & Neckel 1962) and blue Ca II resonance doublets K (3934 Å) and H (3968 Å) (Linsky & Avarett 1970) are prominent Fraunhofer lines.

The predominant continuum emission from the Sun is from the photosphere which is a thin layer about 500 km thick. Opacity here is low enough for photons to escape from here into outer space. For example, about 200 km above the visible photospheric limb has optical depth $\tau_c = 3.7\overset{\times}{1}\overset{\wedge}{0}^{-3}$). Underlying the photosphere are the convection zone, the radiation zone and

Parameter	value
Luminsity	3.85×10^{26} W
Mass	1.98×10^{30} kg
Mean density	1.403 gm cm^{-3}
Radius	6.9×10^{8} m
surface gravity	274 m s^{-1}
T_{eff}	5 700 K

Table 1.1: Some parameters of our Sun

finally the core which houses the nuclear engine, the Heart of the Sun. In any wavelength optical depth $\tau_\lambda = 1$ is reached at most just a few kilometers into the photosphere. Information regarding deeper layers can infered on basis of indirect evidence from helioseismology and theoretical modeling. Overlying the photosphere are the rarefied chromospère and the corona.

Modern understanding of the Sun is based on the Standard Model (Vernazza et al. 1970; Stix 1990). The model predicts various parameters such as density, temperature, pressure, ionization, and opacity as a function of radius, as shown in Table 1.2.. It is an idealization of the Sun assuming the following simplifications:

1. Spherical symmetry;

2. Hydrostatic equilibrium: $\partial P/\partial r = -\rho g$.

$r/R_\odot$	$m/M_\odot$	P [Pa]	T [K]	ρ [kg m^{-3}]	$L/L_\odot$
1	1	1.2E+10	5.7E+3	3.0E–4	1.0
0.68	0.97	3.7E+13	2.0E+6	2.2E+2	1.0
0.34	0.7	6.0E+14	5.0E+6	7.5E+3	1.0
0.16	0.23	7.0E+15	1.0E+7	5.0E+4	0.84
0.03	0.03	2.2E+16	1.5E+7	1.4E+5	0.022

Table 1.2: Mass, pressure, temperature, density and luminosity in the Sun. Adapted from Stix (1990)

3. Local thermodynamic equilibrium (LTE): the source function $S_\nu = B_\nu$, where $B_\nu = 2h\nu^3/c^2[exp(h\nu/kT) - 1]$ is the Planck function.

4. convection/mixing occurs only if the Schwarzschild criterion for stability of stratification is violated.

5. Gas pressure $\gg$ radiation pressure, so the perfect gas law $P = \rho\,\mathcal{R}T/\mu$, holds

where P, ρ and g are pressure, density and gravitational field strength, respectively; furthermore, $\mathcal{R}$ and μ are, respectively, the gas constant and the mean molecular weight. More accurate models must incorporate degeneracy pressure due to the partially degenerate electrons, and especially electrostatic pressure which can in some regimes be as high as 10% the gas pressure.

The predominant energy source in the Sun is Hydrogen burning via the p-p (proton-proton) cycle. There are 3 such cycles: pp I, pp II (involving

Lithium) and pp III (involving Boron). The branching ratios for (pp I: pp II + pp III) is 87:13. The total energy release per pp I reaction is 26.732 MeV, that is, 6.683 MeV/nucleon. This means about 3.643 $\times 10^{38}$ protons are converted to He per sec, equivalent to 10^{11} kg s^{-1}!

Energy production as well as mass of the Sun are concentrated in $r \leq 0.3R_{\odot}$, defined to be the core, where the central temperature is about 1.5 $\times 10^{7}$ K. The mode of energy transport in the radiative zone ($0.3R_{\odot} < r < 0.71R_{\odot}$ is radiation. The region between the radiative zone and the photosphere is the convection zone, to be briefly discussed in section 1.2.

1.2 Solar convection

Solar convection is a process whereby internal energy and sometimes latent energy is transported by matter. The mixing length concept is used to model convection. According to this, parcels of hot gas travel a distance before dissolving and depositing their excess heat.

1.2.1 Convective instability and transport

As first shown by Schwarzschild in 1906, a parcel of gas becomes unstable and is driven upwards by buoyant force if:

$$\left(\frac{\partial \rho}{\partial r}\right)_a < \frac{\partial \rho}{\partial r}, \tag{1.1}$$

assuming that the parcel travels sufficiently fast to behave adiabatically. In Eq. 1.1, suffix a refers to adiabatic condition. Assuming pressure equilibrium and also that the mean molecular weight μ varies as a similar function of temperature and pressure both within and outside a parcel, the above equation is rewritten as:

$$\frac{\partial T}{\partial r} < \left(\frac{\partial T}{\partial r}\right)_a, \tag{1.2}$$

The sufficient condition Eq. 1.2 has been shown to be also a necessary condition (Lebovitz 1966).

Upon the onset of convective instability, the material motion grows in amplitude. In a viscous medium, these motions may develop into regular, stationary cells like Bénard cells. In the inviscid stellar gas, they develop into non-stationary turbulent convection.

The mixing length theory was introduced as a model to treat convective turbulence in the 1930–50's (Stix 1990). The mixing length l is analogous to the mean free path of atoms in kinetic theory of gases. It is the distance travelled by a parcel of gas before dissolving. According to this theory (Böhm-Vitense 1958):-

$$l = \alpha H_p \tag{1.3}$$

where H_p is a pressure scale height and α a constant. The temperature excess built up by the parcel over a distance $l/2$ can be shown to be:

$$\Delta T = (\nabla - \nabla')\alpha T/2 \tag{1.4}$$

where $\nabla \equiv (\partial \ln T/\partial \ln p)$, and the prime denotes the quantity modified by radiative losses.

Thus the total flux transported by the parcel is:

$$F_C = \Delta T \rho c_p v, \tag{1.5}$$

where c_p is specific heat at constant pressure and v is the velocity of the parcel. Its motion due to buoyant force is governed by:

$$\frac{\partial^2 x}{\partial t^2} = -g\frac{\Delta\rho}{\rho} \tag{1.6}$$

The above can be manipulated to yield the velocity of convection:

$$v = l\left(\frac{g\delta}{8H_p}(\nabla - \nabla')\right)^{1/2} \tag{1.7}$$

Name	Scales (Mm)	Lifetime	velocity (km s^{-1})
Granulation	1.4	10 min	1.0
Mesogranulation	7	5 hr	0.1
Supergranulation	30	25 hr	0.4
Giant cells	10^3	weeks	0.1

Table 1.3: Typical length-scale, lifetime and horizontal velocity for four scales of convective phenomena in the Sun

1.2.2 Convective scales in the Sun

Convective phenomena in the Sun have been observed at 4 discrete scales: (a) granulation, (b) mesogranulation, (c) supergranulation, and (d) giant granulation. Some properties of these phenomena are summarized in Table 1.3: In the region just below the photosphere, H and He are partially ionized. Thus, photons can be absorbed to excite or ionize the gas, which leads to an increase in opacity. The resultant build-up of latent heat steepens the (negative) temperature gradient, setting up secondary convective processes like the above mentioned. It is not clear, whether these are in fact observed convections or manifestations thereof (Worden 1975). For example, they are possibly convective overshoots, which are convection parcels penetrating into stably stratified layers with subadiabatic environment (Shaviv & Salpeter 1973).

Granulation

Granulation is the smallest scale of solar convective phenomena. It is a non-stationary cellular pattern covering the entire Sun except sunspots. Reminiscent of convective cells, granules are bright cells corresponding to hot upward moving gas, surrounded by prominent dark lanes corresponding to cool downward moving gas. They have a central upflow of about 0.4–1.0 km s^{-1} (Beckers & Morrison 1970; Durrant et al. 1979), a horizontal flow of about 1.0 km s^{-1} and a small dowflow velocity. The length-scale quoted in Table 1.3 refers to the mean distance between the centers of two adjacent granules, ie., includes the scales of cells *and* the lanes. It is believed that inspite of diversity in granular size, the intergranular distance remains stable (Namba & Diemel 1969). They constantly evolve by brightening, moving, fragmenting, disppearing and appearing. Exploding granules is a term used to describe granules that show a ring structure which expands and fragments (Title et al. 1986). The lifetime of granules was derived first using cross-correlation (CC) technique by Bahng & Schwarzschild (1961), who report a value of 6 min. The height extent of the granules is a few hundred km with velocity decreasing with height (Kiel & Canfield 1978; Nesis et al. 1980). Models of granules as convective cells are diverse (Bray et al. 1984). A numerical 3D time-dependent model has been developed by Nordlund (1985).

Granulation is believed to be driven by latent heat in partially ionized H. About 50% H is ionized at 1 000 km below photosphere. Assuming that the horizontal scale of granulation is approximately the same as its depth extent, we can explain the observed scale of granulation.

Mesogranulation

Mesogranules were discovered by November et al. (1981) by studying the velocity divergence pattern in Mg I 5173 Å Dopplergrams. Corroboration came from observations of Oda (1984), who noted that active granules, ie.,

granules that take part in a reproductive series of expansion, fragmentation, formation, etc, tend to cluster together in a network pattern with mesh size of about 10″. Typical vertical velocities are reported to be ± 500 m s^{-1} with rms value of 60 m s^{-1}. Using granules as tracers, a horizontal value of 1 km s^{-1} has been determined (Title et al. 1981; Brandt et al. 1988). Mesogranulation is driven at a greater depth than granulation. It is attributed to the latent heat in partially ionized He I. About 50% He I is ionized at 7 000 km below photosphere. According to mixing-length theory, the horizontal extent of mesogranules will be of the same order, which explains their observed scale.

Supergranulation

Supergranulation is a system of large-scale ($\sim$ 30 000 km) velocity cells observed in the photosphere. It can be observed in various photospheric atomic lines like Na I D1 and D2, Fe I 5578 Å, Fe I 8688 Å, etc. It was discovered by Hart (1954; 1956) as a systematic departure from the rotation field of the Sun, and studied in detail by Leighton and his group (Leighton, Simon & Noyes 1962; Simon & Leighton 1964; Simon 1964) using the photographic Doppler heliogram technique. They argued that it is a the surface manifestation of convective cells in the Sun, presumably originating because of convective instability in the He ionization zone. There are typically 5000 - 10 000 supergranules at any time on the Sun. Supergranulation is possibly a secondary convection rooted at the He ionization zone about 10 000 km below the photosphere. Supergranulation is discussed in greater detail in a later section.

Giant granulation

The largest reported manifestation of convection in the Sun are "giant cells" or "giant granules" (Bumba 1967). Their length-scale is about 10^8 m and horizontal velocity about 100 m s^{-1}. Giant cell motion can be in principle be

studied by using the chromospheric network or its fine structures as tracers. Schröter & Wöhl (1976) and Schwan & Wöhl (1978) have used network mottles as tracers to obtain velocity fields scales much larger than supergranules. Taking solar rotation rate $\Omega_\odot$ to be 3×10^{-6} rad s^{-1}, we find that Rossby number $\mathrm{Ro} \equiv v/L\Omega_\odot < 1$, which is a measure of inertial over Coriolis force, is less than one, suggesting that solar rotational effects cannot be ignored in case of giant cells.

1.3 The Solar chromosphere

The stellar atmosphere is the region of rarefied, loosely bound outer layer of stars characterized by high temperatures and emission lines. Through it the stellar interior makes contact with interstellar matter. There are reasons to expect that most stars have atmospheres. The high temperature of the atmospheres ensures that they do not collapse but have large scale heights.

During total solar eclipses, one sees a diffuse, asymmetric pearly white halo surrounding the solar limb, extending to many solar radii. This is the solar corona, the hotter and more rarefied, outer part of the solar atmosphere. The inner layer, the chromosphere. is seen as a red annulus (due to Hα emission) just at the onset and end of total eclipse. Normally, it is too faint to be observed against the glare of the photospheric light scattered by Earth's atmosphere, and can be seen terrestrially using coronagraphs at high altitudes, or from space in the UV (ultra-violet), X-ray bands and the Fraunhofer lines of Ca II H and K, and Hα and Hβ.

Evidence for outward increase of temperature in the solar atmosphere comes from observations of line emissions from highly ionized atoms. For example, the coronal green line at 5303 Å is from Fe XIV. Many coronal lines have been identified with forbidden lines from highly ionized atoms. The relatively cooler chromosphere is marked by emission lines mostly from singly ionized atoms.

After early confusion, the height of the chromosphere as defined by the Hα region was accepted to be about $h = 5\ 000$ km, with extensions in the range 4 000 km–10 000 km, if pencil-like jets called spicules protruding outside from the chromosphere were considered. However, the chromosphere is nowadays increasingly accepted as the region between the temperature minimum T_{min} ($\tau_c = 10^{-4}$), and the $T = 25000$ K level. According to most models, this falls at $h = 2000$ km, where $h = 0$ corresponds to the $T = 5700$ km level, which corresponds to the visible photosphere.

1.3.1 Morphology

Chromospheric morphology may be divided by manner of observation into: (a) limb features; (b) disk features. It is not always possible to identify disk features with limb features since limb darkening and blurring of disk features towards the limb makes it difficult to follow a disk feature as it crosses (by way of solar rotation) the limb. However, in some cases a definite association has been possible: eg., helmet streamers have been associated with the dark filaments observed on the disk in Hα spectroheliograms.

Limb Morphology

The prominent limb fine structures are spike-like jets called spicules, extending from middle to upper chromosphere. Spicules are about $10'' - 15''$ high and about $1''. - 2''$ thick. Exceptional ones, which are associated with transient activity like flares and eruptions, can be over $50''$ long. Often in such cases they disappear in Hα and appear in the EUV (extreme ultra-violet) range at greater heights. Spicules consist of hot plasma flowing along their axis at about 25 km s^{-1}. They have lifetimes typcially in the 5 - 10 min range. During this time, they rise, and subsequently fade away. On their account, the upper chromosphere is highly inhomogeneous. They are generally hotter than the ambient gas at lower altitudes, but at $h > 5000$ km, they

coexist with hot gases at $\approx 10^6$ K. They are often clustered, with ones in a given cluster pointing in almost the same direction.

Limb observations also allow us to view directly the height extent of the chromosphere, and to obtain other parameters like chemical composition and temperature as function of height.

Disk morphology

The most prominent K line chromospheric feature on the disk is the plages, which are bright regions surrounding dark sunspots. The plages and sunspots together constitute the "active Sun", which are essentially regions of enhanced magnetic activity. Plages usually apprears as clusters of chromospheric "faculae". The corresponding photospheric faculae are almost always not apparent and seen only close to the limb. Faculae are brighter when closer to sunspots. The major feature of QS (quiet Sun) is the chromospheric network, to be discussed later.

At any time, plage contribution to the total K line flux is excess of the fraction of area occupied by them. Pap (1992) estimates that plage contribution to the Lyman α, an upper chromospheric line, is 50%. Plages are usually confined to an equitorial belt extending approximately from 40° N to 40° S. During a sunspot cycle, plages tend to follow the sunspots to lower latitudes as cycle advances. They are relatively long lived (about a month or more). Indeed, their stability has been exploited to determine solar rotation rate (Singh & Prabhu, 1985). Furthermore, integrated fluxes from stars have been used to study activity cycles in them.

In the Hα line, thin ($\sim$ 5 Mm) elongated ($\sim$ 100 Mm), sometimes curved dark filaments are seen in QS. These are in fact prominences seen against the disk. In addition, other dark elongated structures called fibrils are seen to extend from the plages, bending horizontally over the disk. The fibrils are typically 15 Mm long, 1 Mm thick. Axial material flow in fibrils

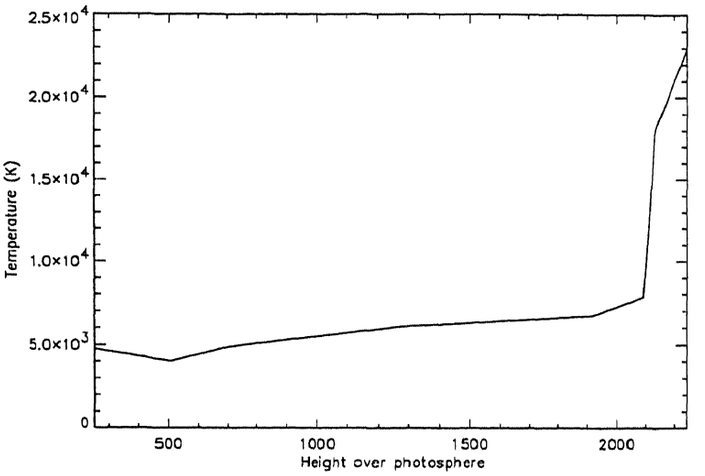

Figure 1.1: Temperature profile of the chromosphere. The temperature rises steeply after $h = 2000$ km, leading to the transition zone.

can be as high as 25 – 30 km s^{-1} which is close to the spicule value. It is thought that fibrils are clusters of dark mottles. The strong fibril field curves back at low heights ($h = 4000$ km) over the photosphere, which is the reason for their elongated appearance seen against the disk. On the other hand, the magnetic fields over spicules and dark mottles are mostly vertical.

1.3.2 Physical conditions

Three striking features of the atmosphere are its: (a) high temperature, under nonthermal conditions, (b) strong magnetic field influence, (c) high temporal and spatial fluctuations.

High temperatures

The solar chromosphere consists of plasma at high temperatures. A profile of the temperature in chromosphere is given in Fig 1.1. As h increases, temperature falls as expected in a radiation-convection model until it reaches

region	h (km)	n (cm^{-3})	T (K)	P = nkT (erg cm^{-1})	B (G)
photosphere	0	10^{17}	6000	8.3×10^4	1 440
chromosphere	1 500	10^{12}	10^4	2.8	8.4
corona	3 000	10^8	10^6	0.028	0.84

Table 1.4: Height h, number density n, T, pressure P, and the equipartition value of magnetic field, **B** for the three layers of solar atmosphere. Adapted from Zirin (1988).

4000 K at $h \sim 500$ km. Then it rises slowly until $T = 7500$ K close to $h \sim 2000$ km. The almost flat profile seen in the chromosphere is due to the thermostatic conditions caused by H ionization. Once all the H is ionized around $h = 2000$ km, temperature rises steeply to 20 000 K - 25 000 K. Earlier models posited a second plateau around 20 000 K, with 25 000 K being the lower temperature boundary of the transition zone that seperates the chromosphere from the corona.

Important role of magnetic fields

The atmosphere has a very low density. Magnetic field stores energy at density $(B^2/8\pi\mu_0)$; it interacts with convection velocity fields and modifies it. The strong influence of magnetic fields in the chromosphere can be judged from the plasma β, the gas pressure to magnetic pressure ratio given by $8\pi\mu_0 P/B^2$. The greater influence of magnetic fields on gas dynamics in the case of the chromosphere and corona than in photosphere may be gauged from Table 1.4.

Magnetic fields affect the chromosphere by channeling energy from below (section 1.4.2) to heat the chromosphere. Indeed, there would be no

chromospheric network without magnetic fields.

High spatial and temporal fluctuations

The atmosphere is highly inhomogeneous, as evidenced by streamers, coronal holes and prominences in the corona, and spicules, flares, plasma jets and umbral flashes in the chromosphere. The spatial fluctuation in the chromosphere can be as high as 100 between brightest and least bright points. Temporal fluctuation factor in intensity can be as high as 2 in just a minute.

1.3.3 Chromospheric heating

The heat budget of the chromosphere is 4×10^3 W m^{-2} in QS and 2×10^4 W m^{-2} in active regions (Withbroe & Noyes 1977). As black-bodies, these correspond to temperatures of the order of 7000 K. These high temperatures cannot be due to thermal heating (conduction, convection, radiation), since that would violate the second law of thermodynamics, which would require a outward fall in temperature. Diverse nonthermal mechanisms have been proposed to account for atmospheric heating: (a) shock wave heating; (b) electrodynamic heating by waves or currents; (c) others mechanisms such as conduction.

Shock wave heating

Granular turbulence in the H convection zone produces low amplitude acoutic waves. The energy density of the wave is given by:

$$e = (1/2)\rho A^2 C_s^2 \tag{1.8}$$

where ρ is matter density, A is amplitude of wave and C_s is sound velocity. As the wave rises into chromosphere, crosses the temperature minimum, e and C_s are approximately constant. Thus $A \sim \rho^{-1/2}$. Assuming vertical stratification of the atmosphere, density $\rho \sim exp(-h/h_0)$, where h_0 is scale height.

As the density drops exponentially, the amplitude becomes abruptly steeped, and the acoustic waves turn into shock waves. Shock waves heat matter by viscous friction (Biermann 1946; Schwarzschild 1948). Since thermal conductivity along the field lines, $k_{||}$, is larger than that across lines, chromospheric regions overlying supergranular edges are preferentially heated, since the edges accumulate magnetic flux (section 1.4).

The acoustic waves will degenerate rapidly into shock waves (Mein & Mein 1980). Hence, acoustic wave heating is expected to be responsible for the heating of lower chromosphere. However, it is generally accepted that shock wave disspiation is responsible for the temperature inversion. Furthermore, it is thought that radiative damping in the photosphere might well remove from the acoustic waves energy that exceeds the entire energy budget of the outer solar atmosphere (above temperature minimum) (Jordan 1981). Acoustic waves are restricted by an upperlimit of $\tau = 3$ min at the T_{min} level (Stein & Leibacher 1974).

MHD wave heating

3 distinct modes of MHD waves are possible: fast, slow and Alfvén, in an atmosphere dominated by magnetic fields. The damping mechanism for Alfvén waves is joule dissipation, while that for fast and slow modes is shock dissipation. In regions of $B < 100$ G, waves from the turbulent zone will predominantly be fast mode (Osterbrock 1961).

Alfvén wave heating was proposed for an incompressible medium first by Parker (1974). Antia and Chitre (1979) have shown that models that include compressibility and thermal dissipation in the plasma show that fast mode magnetoacoustic waves can explain at least some phenomena like umbral flares (Zirin & Stein 1972). The origin of such waves could be the violent buffetting of fluxtubes by granules. A possible conduit for these waves is the bright points (BP) seen in the interior of chromospheric network cells (sec-

tion 1.4), also called K2V grains, which are probably flux-tubes (Sivaraman & Livingston 1982; Kalkofen 1990; Sivaraman 1990). Inspite of the $\tau = 3$-min threshold on acoustic waves, longer period acoustic waves could be seen at chromospheric heights by the conversion of initial transverse waves into acoustic waves at a later stage (Kalkofen 1987). The flux associated with an Alfvén wave is:

$$F_A = 2\rho\langle v^2\rangle v_A, \tag{1.9}$$

where v_A, velocity of Alfvén waves is given by $v_A = B/\sqrt{4\pi\rho_0}$ and where $\langle v^2\rangle$ is the rms of square velocity of the photospheric footpoints. To dissipate Alfvén waves small scale variations (< 1000 km) in the magnetic field would be needed. Preliminary analyses have shown that the BP can provide for the entire chromospheric energy budget. Simultaneous G band and Ca II K images can help verify this, since the former can be used to track and measure rms velocity of BPs whilst the latter to look for related brightenings in chromosphere (Krishnakumar & Venkatakrishnan 1998).

Current heating

Heat is generated when plasma is forced to flow across field-lines. This produces a force according to Lorentz force $\mathbf{v}\times\mathbf{B}$, which causes electrons and ions to move differently. This creates a local charge separation, thereby leading to currents and electric field. These currents modify the ambient magnetic field. Generation of energy is governed by Poynting's theorem:

$$\mathbf{j}.\mathbf{E} = \frac{-c}{4\pi}\nabla.(\mathbf{E}\times\mathbf{B}) - \frac{1}{8\pi}\frac{\partial \mathbf{B}^2}{\partial t^2}. \tag{1.10}$$

The $\mathbf{j}.\mathbf{E}$ energy is dissiplated by Joule heating of cross-field and field-aligned currents and by viscous and mechanical heating. Another form of current heating aries from reconnection of magnetic field lines, also called topological dissipation, first proposed by Levine (1974). In this a number of cross-field current driven neutral sheets are assumed to exist in the atmosphere leading

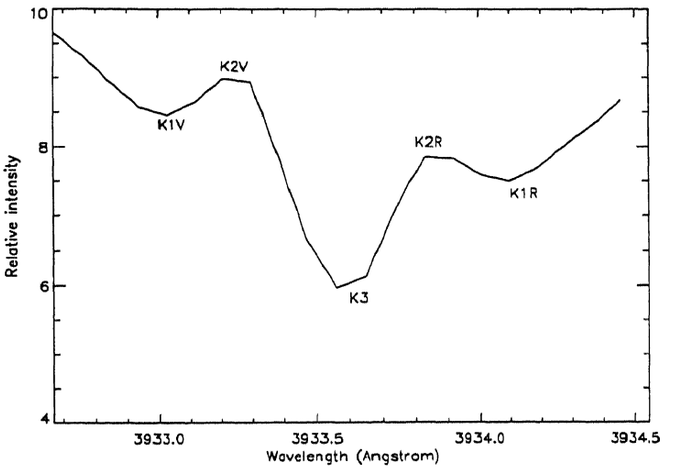

Figure 1.2: Profile of the Ca II K line in quiet chromosphere. Note the strong central self-reversal.

to reconnection, which results in joule heating and particle acceleration (Ionson 1978). Parker has shown that magnetic fields in active regions can build up stresses because of foot point motions in the turbulent zone. Stressed coronal loops then undergo reconnection. Reconnection is not as important to the chromospheric heating scenario as to coronal heating. Other mechanisms of chromospheric heating include radiative damping of acoustic waves, radiative and conductive heating from the corona.

1.3.4 The Ca II K line

Some of the lines originating in the chromosphere are Fraunhofer lines Hα, Hβ, the Ca II resonance doublets K (3934 Å) and H (3968 Å)lines, and the Mg II doublets h (2802 Å) and k (2795 Å). The K and H lines are the deepest and broadest Fraunhofer lines in the visible solar spectrum. They are formed by the 4^2P to 4^2S orbital transition in the Ca II ion. At the line center $\tau = 10^7$ at the photosphere and $\tau = 10^4$ at T_{min}. The entire core of

the K line is formed in the chromosphere and can be used as a chromospheric probe (Linsky & Avrett 1970). The K and H lines are collisionally controlled by the excitation of Ca II ions due to electrons freed by the ionization of H.

As seen in Fig. (1.2), the Ca II K profile shows a two-peaked structure, peaks being K2R (on red side) and K2V (on violet side and usually taller). It is bounded by the K1 valleys. The significant central reversal is typical of the K line in QS. In active regions the reversal is not so marked, and apparently absent over umbral regions (Skochilov & Teplitskaya 1997). This self-reversed doubly peaked profile is sometimes called the K_{232} line profile.

The line profile can be thought of as a height map of temperature in the chromosphere (Stix 1990). As one approaches the line center from the continuum, opacity increases and one sees higher up in the atmosphere, where initially temperature falls. Correspondingly, emission is weaker in the part of the profile leading to the K1 valleys. However, above the T_{min} level, temperature increases with height. Thus the source function is correspondingly more intense, accounting for rise in the line profile leading to K2 peaks. Upto this stage, LTE holds good approximately. The increase in self-absorption towards the line center leads to the self-reversal in the profile.

The techniques for calculating theoretically the shape of the profile are now available. But they are complicated and involve uncertain knowledge of the geometry of the chromosphere (in view of its inhomogeneities) and uncertain velocity structures of spicules etc. The most favored model is the two-component model (Engvold 1967). According to this the profile is built up at sources located in two layers of fluid moving vertically, one upwards and the other downwards. By sufficient adjestment of parameters the required profile is obtained.

1.4 Supergranulation

Some supergranular properties and associated phenomena are discussed in this section. Some of the important SG (mean) properties are summarized in Table 1.5. The values supplied are typical values.

1.4.1 Velocity fields

The convective nature of supergranulation is evidenced by its 3 components of motion: (a) a vertical upflow, (b) horizontal flow, and (c) a downflow, reminiscent of convective phenomena.

Vertical upflow

The vertical upward component appears usually though not always at the supergranular center. Typically, the speed is 50 m s^{-1} (Worden & Simon 1976; Giovanelli 1980; Küveler 1983). The upflow region covers about 5% of the total cell area. The upflow mass flux is typically 1.5×10^{15} m^3 s^{-1}. Vertical flows are difficult to measure accurately because of interference from the 5-minute oscillations and granulation.

Horizontal flow

The vertical upflow feeds into a radial pattern of horizonatal outward flow in the range 0.1 – 0.5 km s^{-1} (Hart 1954, 1956; Leighton et al. 1962; Simon & Leighton 1964; Deubner 1974; Worden & Simon 1976; Giovanelli 1980; Küveler 1982). The maximum horizontal speed is about 500 km s^{-1} occuring at 0.35 the radius (Küveler 1983). What appears to be agreed upon generally is that horizontal flow magnitudes exceed that of vertical flow (Leighton, Noyes & Simon 1962). Furthermore, upflows are much slower than downdrafts. Convective overshoot into the chromosphere has also been observed (November et al. 1979). The horizontal flow appears in chromospheric line

Parameter	value
Size	30 Mm
lifetime	25 hr
central upflow	50 m s^{-1}
horizontal flow	400 m s^{-1}
downflow	100 m s^{-1}

Table 1.5: Some basic SG properties

Si II (1817 Å) lines at about 3000 km s^{-1}. The thickness of horizontal flows is about one photospheric scale height. or, about 1500 km.

Downflow

The vertical downward component, or downdraft, appears usually though not always at the supergranule boundary, at about 50 m s^{-1} (Tanenbaum et al. 1969; Stenflo 1973). The downdraft is concentrated around narrow magnetic fluxtubes in regions of diameters of about 400 km. There are typically 50 such discrete elements surrounding each cell and occupy an area of about 3×10^6 km^2 per cell (Küveler 1983). Skumanich et al. (1975) estimate that the downward velocities are about 0.41 km s^{-1} in regions with fields exceeding 10 G, with an increase with field strength given by 1.6 km s^{-1} G^{-1} about 20 G–120 G.

λ (μ)	h (km)	$\Delta I/I$	ΔT (K)	region
1.72	200-500	.055	230	lower chromosphere
1.18	+10	0.004	-30	visible photosphere
1.64	-50	-0.007	-60	deep photosphere

Table 1.6: Temperature contrast in SG; adapted from Worden (1975)

1.4.2 Temperature structure

Another important parameter of the SGs is the temperature contrast, ΔT, between the strong field regions at the cell boundary and the weak field region in the cell interior. In Table 1.6, temperature differences as inferred from infrared studies are given (Worden 1975). Since infrared radiation falls in long wavelength limit, assuming Planckian spectrum, $\Delta T = T(\Delta I/I)$. Worden suggests that the actual ΔT could be ten times higher when corrected for resolution. We note that negative ΔT in the deep photosphere, as expected of true convective cells.

1.4.3 Magnetic Fields

Magnetoconvection is the key factor that determines the distribution and strength of magnetic fields on solar surface, and hence the architecture of the chromosphere. Four types of magnetic fields may be distinguished:

1. Fields surrounding sunspots
2. Enhanced network fields
3. Quiet Sun network fields

4. Intranet (IN) fields

The sunspots fields are the strongest. The enhanced network fields are stronger than QS fields, and are found in what we have called semi-active regions: where there is evidence both of enhanced activity and the chromospheric network (CN). The IN flux is predominantly carried in bright points (BPs). The magnetic field in the Sun is in a state of dynamic equilibrium, with flux vanishing by cancellations at the cell edges (Wang 1988b). Introduction of new flux was believed to occur at SG upflow region, but Wang (1988b) claims that they are associated with intranetwork ephemeral regions. He estimates that they introduce new flux at about 2.2 $\times 10^{15}$ Mx s^{-1} throughout the surface of the Sun.

The interaction between convection and magnetic fields can be grouped as: (a) effect of convection on magnetic fields, (b) effect of magnetic fields on convection. Perhaps some of the contradictory findings in today's literature regarding interaction of magnetic fields and convective velocity fields, eg., the effect of activity level on supergranular scales, can be resolved if we take into consideration the complicated nature of magnetoconvection depending on the relative strengths of the magnetic and convective velocity fields.

Effect of convection on magnetic fields

Broadly, there are two ways in which convection affects magnetic fields. One is the sweeping of diffuse flux tubes and in the formation of thin flux tubes, the other is the interaction of velocity fields with priorly formed fluxtubes.

It has been suggested that diffusion of magnetic flux, and the redistribution of fields from a decaying active region are effected through SG convective motion (Leighton 1964). However, Smithson (1973) reports that 'random walk' diffusion accounts for only part of the transport of fluxtubes, with step time much smaller than 24 hr. The other component is a sudden motion whereby the fluxtube covers 5000 km—20 000 km during the time-

span of 1–3 hr. Possibly, peculiar motion of granules is responsible for the latter. Furthermore, Worden & Simon (1980) have shown that two aspects of the dynamics of fluxtubes, namely, (a) breaking up of a single tube, and (b) creation of new flux within the cell, cannot be due to SG convective flow pattern.

Parker (1963) first proposed a 2-D supergranular model in which an initial uniform magnetic field is subsequently concentrated by horizontal motions to cell boundary. The model was extended to a 3-D model by Clark and Johnson (1967) assuming hexagonal cells and a Bénard type velocity field. Some of the results were that downflows are about 0.3 km s^{-1} at side centers and 0.5 km s^{-1} at vertices. Upflow at the cell center was estimated at 0.01 km s^{-1}.

Assuming equipartition of magnetic and gas pressure at SG boundary:

$$\frac{1}{2}\rho v^2 = \frac{\mathbf{B}^2}{8\pi\mu_0}. \tag{1.11}$$

Using typical photospheric values: $\rho = 1.9 \times 10^{-4}$ kg m^{-3}, $v = 400$ m s^{-1}, we find that the equipartition value of $\mathbf{B}$ is about 60 gauss. Now it is believed that the field is concentrated into small fluxtubes with diameters 100–300 km (Stenflo 1973; Wiehr 1978) with fields as high as 500–2000 G, created possibly by convective collapse (Venkatakrishnan 1986). Supergranular downflow occurs at the region of these fluxtubes with the quantity of downflow being proportional to field strength (Stenflo 1973; Frazier 1974). Violent buffetting of fluxtubes by granules and convective collapse are believed to be responsible for the production of such kilogauss fluxtubes (Venkatakrishnan 1984).

Effect of magnetic fields on convection

Magnetic fields affect velocity fields by inhibition of convection and by their plasma confinement property. Both in the case of granules and SGs, the effect of the confinement property is to extend lifetimes. Although there

is good reason to believe that magnetic fields affect also length-scales, the nature of the effect has not been clear (Sýkora 1970; Zwaan 1978; Singh & Bappu 1981; Raghavan 1983; Wang 1988b). Some of the dynamical and morphological effects of magnetic fields on SGs are studied in chapters 4 and 5.

1.4.4 The chromospheric network

The chromospheric network was discovered by Deslandres and Hale in 1893. It is a bright network of large ($\sim$ 30 000 km) cells seen in chromospheric lines such as Ca II K and H (Rogerson 1955). The connection between chromospheric network and supergranulation is provided by the magnetic fields (Leighton, Simon & Noyes 1962; Simon & Leighton 1964). The flux tubes swept to the edges of SGs rise into the chromosphere to channelize the acoustic waves produced by granular convection turbulence. The acoustic waves turn rapidly into shock waves and heat the chromosphere overlying the strong magnetic field regions, thereby creating an enhanced emission network overlying the SG edges (section 1.2.2). The network appears dark in the Hα wing because the wing is formed near T_{min}.

In short, chromospheric network acts as a chromospheric level tracer for supergranulation boundaries. The spatial correspondence of CN to supergranular walls (Küveler 1984) is so close that the estimates of lifetime and size given for SGs in Table 1.5 are more or less applicable to CNCs too.

The network as defined by the photospheric magnetic field has a very fine structure. Higher in the atmosphere, as the magnetic field fans out, the structure becomes coarser (Stenflo 1988). So far there are no high resolution chromospheric magnetogram studies because the prominent chromospheric lines are magnetically weak. Hence it is customary to study photospheric lines and extrapolate them into chromosphere. Some magnetically sensitive lines are the photospheric FeI 8688 and also the relatively less strong chromo-

spheric line Ca II 8542. Singh & Bappu (1981) and Raghavan (1981) report small changes in cell sizes during the solar cycle, but no changes in the cell wall thickness.

Measurement of upward height extent of network is hampered by lack of good resolution in UV observations, which is worse than 6″. Still, observations in Lyman α and the He II (304 Å) suggests that the network extends into the upper chromosphere.

At higher resolution ($\sim 2'' - 3''$), three distinct features of the quiet Sun are seen to contribute to the K-line flux: (a) network elements; (b) cell interior, and (c) mixed region:

Network elements

At high resolution, one finds that the walls are made up fluffy components called flocculi. The flocculi are about 5 – 10″ in length and 1 – 2″ in width, with a lifetime in the range 2 hr. They have a tendency to recur at approximately the same spot, so that the cell boundary as a locus of flocculi is much longer lived.

The Hα wing dark network at higher resolution is seen to be composed of so-called dark and bright mottles. (Janssens 1970; Foukal 1990). The dark mottles are about 3″–5″ long and $2'' - 4''$ thick. Bright mottles are slighly smaller and less elongated. The mottles tend to cluster with bright mottles taking up interstitial positions between dark ones to form a complex rosette pattern (Janssens 1970). Dark mottles are usually identified with the K line flocculi, and with spicules seen in the limb (Beckers 1963). A rosette represents a funnel or strand of magnetic field of a single polarity. Indeed, when two rosettes are close enough, the pattern of the mottles is one of attraction or repulsion. The rosette is sometimes referred to as "active region seen in microcosm" (Beckers, 1963; 1964a,b; Noyes, 1967).

The total number of flocculi or dark mottles at any time has been

estimated to be about 3.5×10^5 (Beckers, 1963). Since there are $\sim 5 \times 10^3$ network cells at any time on the solar surface, one estimates that a cell is bounded on an average by $\sim$ 100 flocculi. It is believed that the thin magnetic flux tubes (Stenflo 1980) that crowd the network cell walls occur within the flocculi.

Cell interior and mixed regions

The term cell interior refers to the regions enclosed or almost enclosed by the network pattern. In K line, the interior has a relatively dark background spotted with brighter BPs, which are $\approx 2''$. The following fine structure emerges in the cell interior as seen in Hα wing:- (a) bright interior (corresponding to darker K line image interior); (b) dark grains (corresponding to K line BPs), with lifespan of 5 min.

Upon inspection of a K filtergram, not all of the quiet chromosphere is found to be covered by cells (section 4.2). There are the mixed regions, that show an arbitrary pattern of brighter regions (like network elements) and darker regions (like cell interior), not forming any obviously discernible pattern, as given in Fig. 3.1E.

1.5 Motivation for the present study

In the present work, we have aimed to study lifetime and length-scales of the CN, which can shed light on the morphological and dynamical properties of convective cells in the Sun. These parameters are estimated digitally using the correlation technique. The advantage of the digitial method is that it is faster, more objective, more accurate and more flexible. Length-scales were determined also by visual inspection and a technique of tessellation.

Correlation studies of lifetime and scales help us determine diffusion rate at the solar surface, which is relevant to the understanding of the evolution of features. The nature of the interaction of convective velocity fields

and magnetic fields is not fully understood. In view of this, it is useful to study the dependence of lifetimes and scales on activity level and latitude.

Chapter 2

Observations and data reduction

2.1 Introduction

Many important problems in helioseismology, solar supergranulation, and organization of solar magnetic fields require long and continuous observation of the Sun without interruptions. For example, oscillatory modes in the Sun, whose observations are important in helioseismology, can have time periods of many days. It is of interest to study these phenomena without interruptions due to the day-night cycle. But, nowhere within our country even at summer season do the daylight hours exceed 15 hr.

In specific, study of evolution of deep convective phenomena in the Sun requires continuous monitoring for 2–3 days. Thus it is too long to be measured within a day and too short to be observed on a day to day basis as changes occuring overnight cannot be unambiguously related to features observed the next day. A further disadvantage from the day-night cycle is that it will involve "thermal shocks" associated with daybreak and nightfall (Rogers 1970). Hence, uniform seeing, important for correlation lifetime estimates, may not be possible.

A possible solution would be to set up a network of observing stations at various longitudes. During the International Geophysical Year (IGY), the period from July 1957 to Dec. 1958, a continuous movie was made from Hα filtergrams provided by a worldwide network of small telescopes. Since the film was made from various stations, it was of uneven quality and marked by frequent gaps. In recent times, the Global Oscillation Network Group (GONG) has been set up with the purpose of studying oscillations in the Sun.

Another solution is to observe the Sun from satellites orbiting in high inclination orbits. However, this is an expensive option since booster rockets needed to lauch such a satellite have to be more powerful than those used for equitorial orbits.

Yet another good option to avoid sunset terrestrially is to go to higher latitudes during the local summer. At such places, one can observe the mid-night Sun, weather permitting. The first observations of this kind were made in 1966 by US scientists working at the US military base Thule, Greenland using a 15-cm refractor, Hα filter and a 35-mm movie camera to record a nearly continuous sequence of photographs for 62-hr. Keeping these in mind, it was decided to send an expedition to Antarctica from IIA. The plan was to obtain at least a 2–3 day observations without interruptions to study the evolution of chromospheric network cells.

Data for the study of latitude dependence of cell sizes was obtained from the Kodaikanal solar Observatory of IIA. One of the reasons for using this data is that resolution in the observatory data ($\sim$ 1″) is better than that obtained from Antarctica. Further, long term plage free data, which is desirable for latitude dependence studies (Section 4.4) is readily available. The epoch of observations at Antarctica was during solar maxiumum (1989-90), whereby sunspots and plages are to a good extent unavoidable. In fact, sunspots are needed for image alignment.

2.2 The Antarctic expedition

A 3-member team was selected to install the telescope at Maitri, India's new permanent Antarctic station after Gangotri, and to make observations during the local summer. The team was led by Jagdev Singh, and other members were G. S. D. Babu of IIA and Wahab Uddin of the Uttar Pradash State Observatory (UPSO). The program was financed by the Dept. of Ocean Development.

In 1988, the Indian Dept. of Ocean Development set up a new permanent station Maitri (70°45′38″ S, 11°44′49″ E) in the Schirmacher hill range about 80 km from the Dakshin Gangotri, the old Indian permanent station in Antarctica (70° 05′ N, 12° 00′ S).

Being in higher latitude than the Antarctic circle, the station falls in the region of midnight Sun. In summer, when the snow melts one can use the rocky surface to conduct experiments. It was decided to base the IIA program here. It was to be part of the 9^{th} Indian Antarctic expedition, the first and so far only time that a solar astronomy experiment was part of the Indian Antarctic program (Singh et al. 1994).

2.3 Experimental set-up and observations

2.3.1 Antarctic experiment

The solar telescope used in the program was designed and fabricated entirely in IIA. It consisted of a heliostat with 15 cm aperture mounted on a 2m high pillar. The heliostat mirror collects light from the Sun and directs it in the direction parallel to the rotation axis of Earth. A second mirror at the bottom of the heliostat tube collects light from the above mirror, folds it to feed an objective with focal length f = 300 cm and 10 cm aperture. The converging beam from the objective enters a narrow (1.2 Å) K-line Daystar

filter and the image is recorded by a Minolta X-700 camera. A broad-band blue prefilter was also used to remove possible parasitic light. By means of a push-pull arrangement on the second mirror, the image can be centred on the filter. The heliostat is rotated (24 hr per rotation) by a synchronous motor by means of a worm wheel assembly.

The pass-band for the filter at various temperatures was calibrated for various settings with help of the high resolution spectrograph of the the Kodaikanal solar tower telescope. The camera had the provision to record image epoch on a corner of the film. The resulting filtergrams had an image scale of 66″/mm. Kodak 2415 films of the 35 mm format were used. The size of the image was 28.2 mm, but field-view was was restricted to 2/3 that value by a circular aperture at the focal length of the objective.

During the 50 days of expedition, there were 10 days clear sky conditions. Wind speed on 5 of these days was high ($30 - 50$ kmph), but was quite calm on the other 5 days. It was necessary for the experimental configuration to be stiff when buffetted by such high velocity air motion. Ca II K filtergrams could be obtained on 7 of the 10 days.

On each day, sunshine at the site was available for 20.5 hours in the second week of January, 1990 and about 18 hours towards the end of January, 1990. The lost hours were due to glacial polar ice at the southern horizon which obstructed view for about 2 hours every day. The filtergrams were developed in D-19 developer for 5 minutes at 20° C in a makeshift arrangement aboard the Thuleland ship. The data for 4 days, obtained during quiet and steady atmospheric conditions, are good. Rest of the data was obtained under moderate seeing. Through most of the observations, seeing was determined to be around 2″. The filtergrams bring out well the sunspots, plages and quiet network pattern (Plate 1).

The time-sequence of photographs lasted over 106 hours, spaced at intervals of about 10 min. Exposure times were adjusted according to the time of the day. At early mornings, larger exposures and at noon smaller

No	Parameter	Detail
1	Date	December 1989 to January 1990
2	Region of Sun studied	Predominantly quiet and semi-active region
3	Wavelength	Ca II K (λ3933.67)
4	Seeing	about 2″
5	Bandwidth	1.2 Å
6	Emulsion	Kodak 2415
7	Objective Diameter	10 cm
8	Image Diameter:	28.3 mm
9	Viewfield	A near-circular with diameter about 0.74 of solar disk.

Table 2.1: Parameters of observation for Antarctic experiment

exposures were used. The available exposure times were 1s, 1/2s, 1/4s, 1/8s and 1/16s. A total of 1 200 filtergrams of the Sun in Ca II K line were obtained. In addition, 800 filtergrams in bunches seperated by about 2 hr, with individual filtergrams within the bunch spaced at 30 sec for 3 days were obtained to study solar activity. The longest sequence covered the four and half days January 10–14, 1990. The filtergrams with 4 days of good seeing and half a day of moderate seeing have been used in the analysis. The observational parameters are summarized in Table 2.1.

2.3.2 Kodaikanal experiment

The Kodaikanal solar observatory houses a solar tower telescope and a seperate spectroheliographic apparatus (Bappu 1967). The data for the present analysis comes from one of the spectroheliographs, a K-line spectroheliograph, a 2-prism instrument with spectral dispersion of 7 Å/mm near 3930 Å. It functions with a 60 mm image formed from a 30 cm Cooke photovisual triplet. A Foucault siderostat with 46 cm diameter reflects sunlight

No.	Parameter	Value
1	Time period	solar minima during 1913-1974
2	Region of Sun studied	Plage-free region
3	Wavelength	Ca II K (λ3933.67)
4	Seeing	$\leq 2''$
5	Bandwidth	0.5 Å
6	Emulsion	Ilford 23D50 and others
7	Objective Diameter	0.30 m
8	Image Diameter:	60 mm
9	Viewfield	A near-circular region with diameter of the whole solar disk.

Table 2.2: Parameters of Observation

onto the 30 cm lens. Exit slits centered at K_{232} admits 0.5 Å. Daily disk and prominence spectroheliograms have been obtained with this instrument since 1904.

The data consists of 60 spectroheliograms belonging to the solar minimum phases during the period 1913–1974 which covers 6 solar cycles and 5 minima obtained from the same spectroheliograph. and seeing conditions during observations were about 2″. The observational parameters are listed in the Table 2.2.

The images were digitizied in strips running parallel to the equator using the Photo Digitizing System (PDS) with a resolution of 1.6″. On the whole, 21 latitude strips spaced at the mid-points by 5° were digitized in the range 50° N to 50° , including the equator for each image chosen. The strips that were digitized were 16 mm long on the image (or 480″) running paralled to the equator.

No	Parameter	Value
1	Plate scale of filtergram	30″/mm
3	region scanned	50°N−50° S
3	Axial seperation of strips	5°
4	No. of latitude strips	21
5	Size of scanning aperture in PDS	25×25 μm^2
6	Size of each scanned strip	$480'' \times 15''$
7	Pixel resolution of image	$1.6'' \times 1.6''$/pixel
8	Pixel size of strip	300×9
9	No. of frames scanned	60

Table 2.3: Image and Digitization Parameters

2.4 Data Reduction

Wedge data was obtained for calibration of density against intensity. The data is presented in Fig. 2.1 where log relative intensity is plotted against photographic density. The crosses are actual wedge data points. The density image was converted to intensity image by interpolating the wedge data using spline-3 interpolation (Teukolsky *et al.* 1986) of the Fig 2.1. The conversion was incorporated into the main correlation computing program.

Because of the use of heliostat in the Antarctic observations, the images are rotated with respect to each other. Since cross-correlation must be run for fixed regions of the chromosphere, it is essential to de-rotate the images. While being digitized, the filtergrams were de-rotated by suitable positioning of the scanning platform of the Photo Digitizing System (PDS) machine (PDS manual, Perkin Elmer 1986). Alignment so achieved is crude, and the digitized portions may come from slightly different regions in different images. It must be complemented with further rotational correction during the digital analysis of the images.

The digitized images were stored in (now outdated) magtapes, with

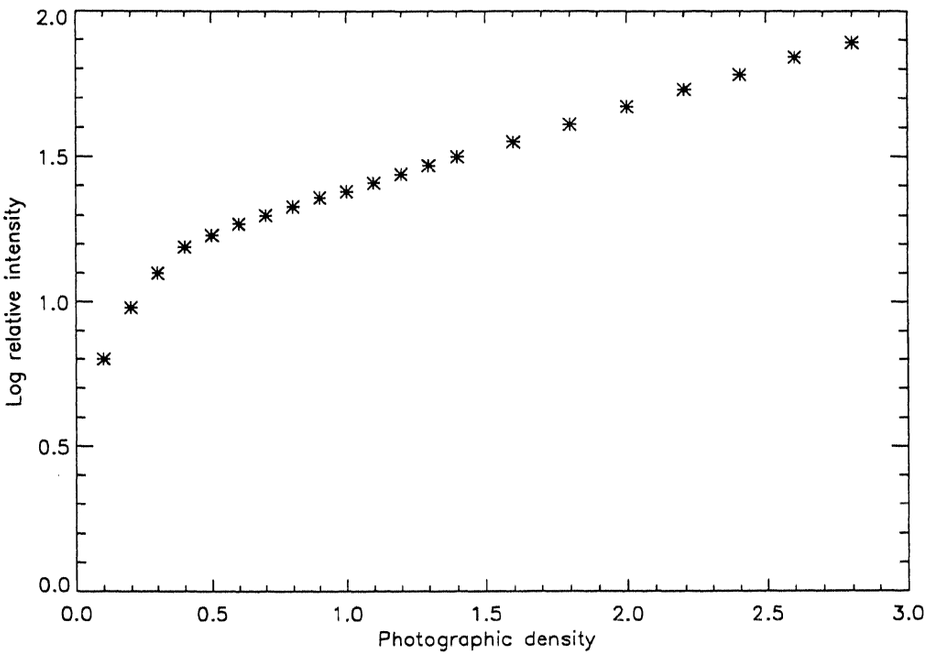

Figure 2.1: Calibration curve obtained using the step-wedge data. The x-axis has photographic density on the film, while the y-axis in units of relative intensity. A spline-3 interpolation was used to convert image density to intesity values prior to analysis.

over 35 images per magtape. The PDS formatted data was converted using a software developed at the Insititute to FITS format which is compatible with the IRAF software package. The digitization produced images of size 601×601 square pixels, which were stored using 2 bytes per pixel, or $601 \times 601 \times 2 \approx 0.7$ Mbyte per image.

The data from magtapes were loaded into the hard disk of the computer systems (Sparc10 and Sparclc) using a Sparc 1/280 magtape drive. The digitized images were inspected for quality: good images generally show up in sharper detail, whereas bad images are fuzzy. Only the better images were retained (more than 80%). Also, images that did not possess more than

No	Particular	Detail
1	Diameter of solar disc on filtergram	28.2 mm
2	Plate scale of filtergram	66″/mm
3	Size of central region scanned	15×15 mm^2
4	Size of scanning aperture in PDS	25×25 μm^2
5	Size of the scanned image	601×601 square pixel
6	Pixel resolution of image	$1.65'' \times 1.65''$/pixel
7	No. of frames scanned	300
8	Mermory occupied by each image	0.722 Mbytes

Table 2.4: Image and Digitization Parameters for the Antarctic data.

two Sunspots were discarded, since at least 2 reference-points are needed to determine how much an image must be rotated/translated for alignment, and only sunspots were used as reference points. Over 50 images were rejected before analysis. Parameters relevant to the image digitization are given in Table 2.4.

2.5 Data Analysis

2.5.1 The correlation function

The correlation function $C(\tau, \Delta)$ quantifies the similarity between two equal numbered data sets. Here τ is the time lapse parameter and Δ is the spatial shift parameter (Chandrasekhar 1955). If normalized, it returns the value 1.0 for identical data sets, the value 0.0 for compeletely unrealated data sets.

It is given by:-

$$C(\tau, \Delta) = N \int_A I(t, r) I(t + \tau, r + \Delta) dA, \tag{2.1}$$

where $I(t, r)$ is the intensity from which the mean has been subtracted and

N, the normalization factor:

$$N \equiv \sqrt{\left(\int_{\infty}^{-\infty} I(t,r)I(t,r)dA\right)\left(\int_{\infty}^{-\infty} I(t+\tau,r+\Delta)I(t+\tau,r+\Delta)dA\right)} \tag{2.2}$$

Each image is labelled by time t, and a point within an image is labelled by position r. The integration is carried over the area A which is common to both images, and the mean to be subtracted from each point on the image is computed from A. A must be statistically large so that $C(\tau,\Delta)$ is independent of A. Correlation with $\tau = 0$ is usually referred to as autocorrelation (AC), or $AC(\Delta)$. Correlation with $\Delta = 0$ is usually called cross-correlation (CC), or $CC(\tau)$.

2.5.2 Digital Analysis

Until recently, correlation as a function of time was obtained using an analog technique originated by Kovacznay (1949). The principle idea in this technique is to pass light through images in register, and use the light transmitted (Rogers 1970) or scattered (Bahng & Schwarzschild 1961) as a measure of correlation. We have analyzed our data on digital computers.

Needless to mention, the importance of digital analysis is that it is more objective, more accurate, faster and more flexible. To compute correlation digitally, Eqs. (2.1) and (2.2) are replaced by discrete:

$$C(\tau,\Delta) = (1/N)\langle \delta I_t(r)\delta I_{t+\tau}(r+\Delta)\rangle, \tag{2.3}$$

where:

$$\delta I(r) = I(r) - \langle I(r)\rangle.$$

where $\langle I\rangle$ denotes the image mean over the common area A, and:

$$N = \left[\langle \delta^2 I_t(r)\rangle\langle \delta^2 I_{t+\tau}(r+\Delta)\rangle\right]^{-1/2} \tag{2.4}$$

Image operations such as multiplication and addition are carried pixel-by-pixel. The input data consisted of the PDS-digitized images.

Chapter 3

Morphological studies on the quiet Chromosphere

3.1 Introduction

Morphological study by visual inspection has important advantages that the statistical methods for study of the chromospheric network lack. It allows us to study size, shape and features of an individual cell, and to follow their evolution. Compared to correlation and Fourier transform methods, it is easy to interpret. Its chief disadvantage is that usually it can't be automated and hence has to be executed relatively slowly; furthermore, it involves an element of subjective bias. Nevertheless, with the advent of many modern image handling software facilities like IRAF, IDL and AIPS, the subjective element is almost trivial.

In the present chapter, we have derived cell scales by visual inspection. Sizes arrived at in this manner may be compared with sizes returned by more complicated methods like correlational analysis (Chapters 4) or tessellation (Chapter 6).

In this chapter we study the size, shape and intensity contrast of cells and their possible inter-relationship. These parameters, especially the latter

two, are best studied by direct inspection. Extensive usage has been made of the IDL and IRAF image-analysis software packages.

3.2 Size and shape of cells

The sizes and shapes of chromospheric network cells come in a great range and variety (Bray & Loughead 1976; Janssens 1970; Sýkora 1970; Singh et al 1994). This is not surprising since they arise as a consequence of the complicated interplay between convective motions and magnetic fields.

The network elements (Section 1.3.3) that enclose the cell are neither regular nor continuous. They vary in thickness and intensity even along the boundary of a given cell. When their intensity drops to a level comparable to that of the cell interior, the wall assumes a broken appearance (Küveler 1984). This happens when the "linear elements" (Janssens 1970), composed of flocculi, do not fully enclose the cell. It is possible that these open cells cause the autocorrelation sizes of cells to be spuriously augmented (Singh & Bappu 1981). Sometimes, the discontinuity is large enough that no obvious cell can be discerned; instead one sees isolated enhanced emission regions, surrounded by a background whose intensity level is similar to that of the cell interior.

A rough sketch of the type of structures we can see on the quiet chromosphere is given in Fig. 3.1. Figures 3.1A and 3.1B are complete cells in that their intensity walls fully enclose them (at low resolution). Figures 3.1C and 3.1D are incomplete cells. Figure 3.1E represents a "mixed region", containing enhanced emission features not obviously arranged in any pattern. They are probably network elements of a now-disappeared cell.

The method used here to study cells combines visual inspection with scanning of the intensity profile. It is similar to the method of scanning a photographic image by a microdensitometer (Simon & Leighton 1964), except that the display and scanning of images was done digitally (using IRAF).

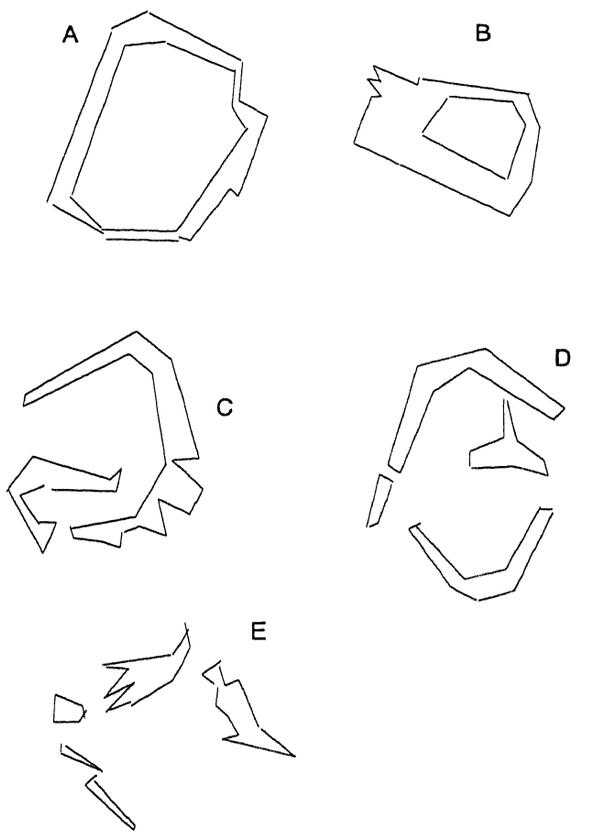

Figure 3.1: Low resolution quiet network elements of the Ca K line. Figures (A) and (B) represent complete cells. Figures (C) and (D) represent incomplete cells, while figure (E) represents elements that pertain to a mixed region.

In order to measure the size and shape of an individual cell, we cut out a rectangular portion of the digital image wholly containing a cell. Intensity scans were made along a series of parallel lines, oriented either parallel to or perpendicular to the width of the image. Consecutive scans were seperated by a pixel width. The choice of orientation depended on the details of the cell features.

At each scan, the two points where the scan intercepts the perimeter of the cell are noted. This is surprizingly easy to identify, inspite of the complicated nature of the cell pattern that emerges under visual inspection. The result of four consecutive scans across the same cell are shown in Fig. (3.2). The two peaks seen at the extremities in each of the plots is considered as cell wall. Each scan is seperated by 2300 km in the direction perpendicular to it. The same relative scaling of intensity holds for all the four sub-images of Fig 3.2. We note the considerable changes undergone by the wall in the relatively small spatial interval seperating them, not only in their geometrical shape but also in their relative intensity. We note the bump seen in Figs 3.2b, 3.2c and 3.2d, which are due to intranetwork BP. That the bump is not a cell wall is best shown by the fact that it lasts only in the 3 scans b,c,d and vanishes before and afterwards. Furthermore, its intensity, although sometimes comparable to the surrounding wall intensity, as in 3.2b, does not appear as a cell wall in the actual images, but rather as a fluffy region of emission inside the cell. In Fig 3.2, the twin peak emissions are seperated by about 30 Mm, though this varies across the cell.

The distance between the two peaks is taken to represent the cell width at that scan. Since successive scans are seperated by a single pixel in the perpendicular direction, each scan is taken to sweep an area with pixel width = 1. The sum of the areas returned by the scans is the area of the cell. From positional information of the walls, the perimeter of cell can be calculated under the assumption that small straight line segments connect the wall positions from scan to scan.

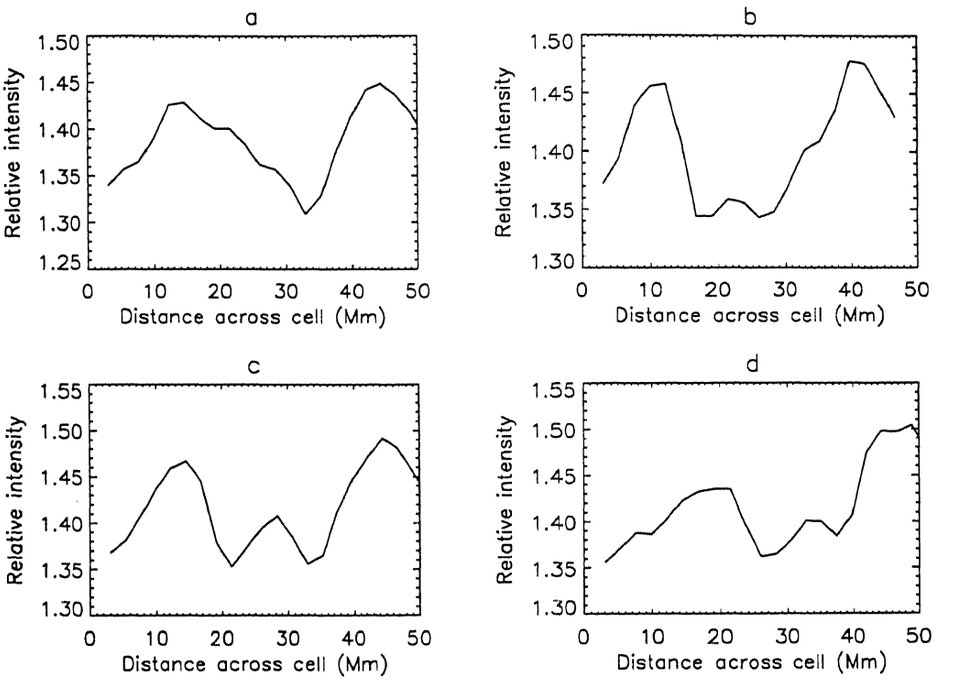

Figure 3.2: Four scans across the same cell. The profiles are seperated by 2300 km in the direction perpendicular to the scans. The two intensity peaks at the extremes are the cell walls. The bump in scans b,c, and d is due to an intranetwork BP.

Occasionally, the wall shows departures from the 2-peaked profile. This is because of the presence of cell intranetwork or network BPs, or the absence of network elements along the scan direction in the region of one or both walls. In these cases, one can usually pinpoint the cell boundary by carefully observing the wall pattern in earlier and later scans, and finding how the pattern changes. If a wall in one scan is seen to correspond closely to two peak emissions in the next scan, the peak that is closer to the wall position may be taken as the wall position in the second scan. Cross-checking with the actual image is very helpful in resolving possible amibiguities and does not appear to require any subjective judgement. However, these complications

make automating the process difficult, if not unreliable.

The two-peak profile vanishes when the scans become tangential to the wall. Usually, this happens twice per cell, at the top and bottom of the scanning range. One encounters a single broad peak, and it is not obvious where the extremities of the cell should lie. Alternatively, an uneven wall might cause more than 2 peaks to appear. At this juncture, the scanning direction is shifted to a direction perpendicular to the present scan orientation. For example, if the earlier scans were horizontal (along x-axis), then let the y-coordinate corresponding to the tangential limit of the scan be say y_0. Vertical scans are used throughout the horizontal range in which the single peak was noted. From the 2-peak profile observed in the vertical scans, we note which range of x-values fall within the cell at $y = y_0$. This represents the required width of the cell at y_0. This procedure must be repeated for one or two more horizontal scans above the y_0 level, in order to ensure that no cell interior points are omitted.

In Table 3.1, we present the characteristic length-scale, maximum length-scale and compactness of 10 QS cells. The characteristic length L is defined so that $L^2 = \Sigma$, the area obtained by the scanning procedure; 'maximum length-scale' refers to the greatest extension of the cell along any direction. The parameter compactness quantifies the circularity of the cell shape. It is also a measure of areal compactness, since the circle can be shown to be the most compact figure in Euclidean 2D space, that is, it packs most area for a given perimeter/circumference. Compactness $\kappa \equiv 4\pi\Sigma/P^2$, which is the ratio of the cell area to the area of a circle with the same perimeter P as the cell. By this definition, the compactness is 1.0 for a circle, 0.785 for a square, and 0.69 for a regular hexagon. Corrugations on the cell wall bring down the compactness of the cell because they increase the perimeter without a commensurate increase in area.

From Table 3.1, we note that the shape of the cells, as judged from mean compactness, is farther away from circular shape than a regular hexagon.

Cell No.	Characteristic length (Mm)	Maximum length scale (Mm)	$\kappa = 4\pi\Sigma/P^2$
1	38.1	46.0	0.62
2	32.4	43.7	0.37
3	27.1	39.1	0.51
4	26.3	39.1	0.52
5	24.7	34.5	0.44
6	24.3	36.3	0.47
7	24.2	34.5	0.67
8	23.8	34.5	0.47
9	21.7	23.0	0.82
10	17.7	18.4	0.96
mean	26.1	34.9	0.59

Table 3.1: Parameters of length and shape for quiet chromospheric cells

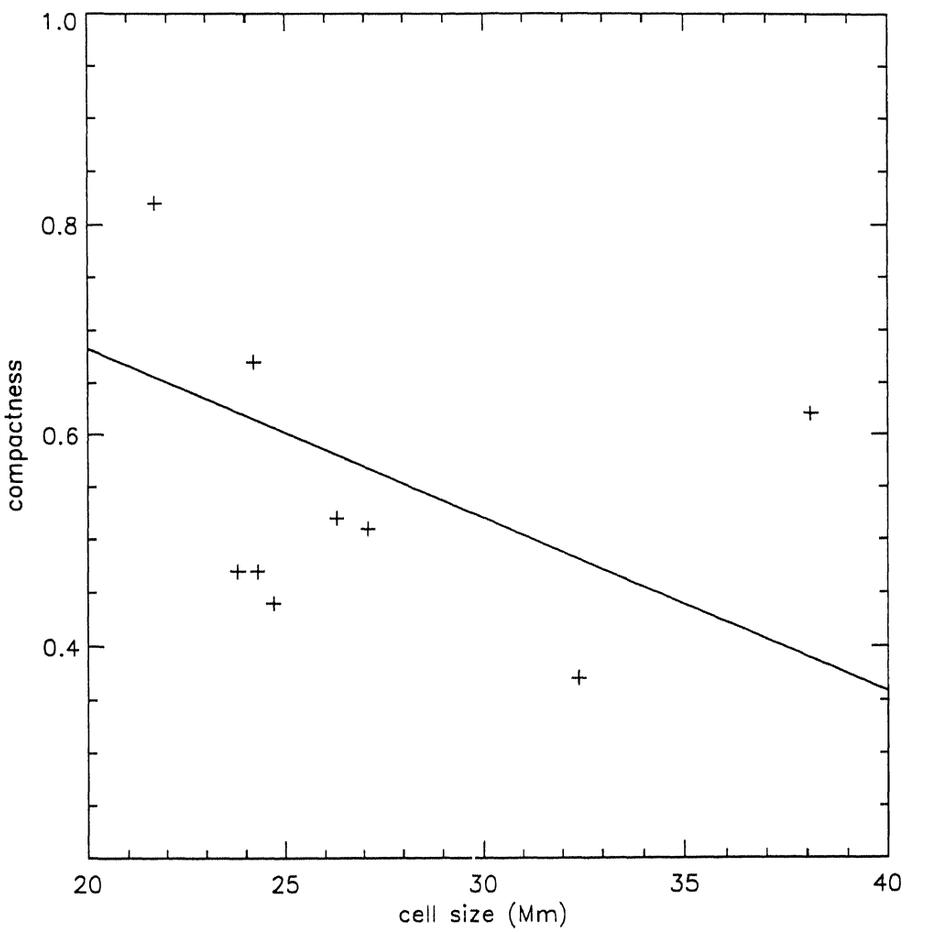

Figure 3.3: Plot of cell compactness vs its characteristic length-scale. The solid line is a linear least squares fit.

The low compactness is not surprising since the size and shape of cells result from turbulent magnetoconvection. Very few cells approach a circle in compactness, though cell no. 4 in Fig 3.4 has an unusually regular shape, which is reflected in its relatively high compactness of 0.82. We found that because of the diffuse nature of the wall, the shape of the cell that emerges upon visual examination can be beguiling. Sometimes, it happens that a cell whose wall appears fairly crooked presents almost rectilinear segments under the scanning procedure. Conversely, apparently straight-edged cells present corrugated and thus uncompact shapes.

A plot of compactness against size, taken from Table 3.1, is given in Fig 3.3. The data shows considerable scatter, but a trend for larger cells to be less compact emerges. Physically, this means larger cells will have more corrugated walls. This suggests an interesting connection between the shape and dynamics of the cell. Smaller cells have smaller sound travel time L/C_s and possibly thus are more likely to iron out irregularities that can corrugate cell boundary.

3.3 Temperature structure of cells

An important parameter of a chromospheric network cell (CNC) is its temperature contrast. According to the usually accepted model of chromospheric heating at the Ca II level, magnetic fields swept to supergranular edges (Simon & Leighton 1964) aid the channeling of acoustic waves produced by H convection zone turbulence. Upon turning into shock waves in the rapidly decreasing chromospheric density, these waves heat the chromosphere (Biermann 1946). Thus, the temperature structure of CNC is crucially dependent on the photospheric magnetic field distribution.

That network cells are not convective cells themselves is evident from the fact that they show intensity enhancements at the cell boundary rather than at the interior. Although it is customary to speak of SGs as convective

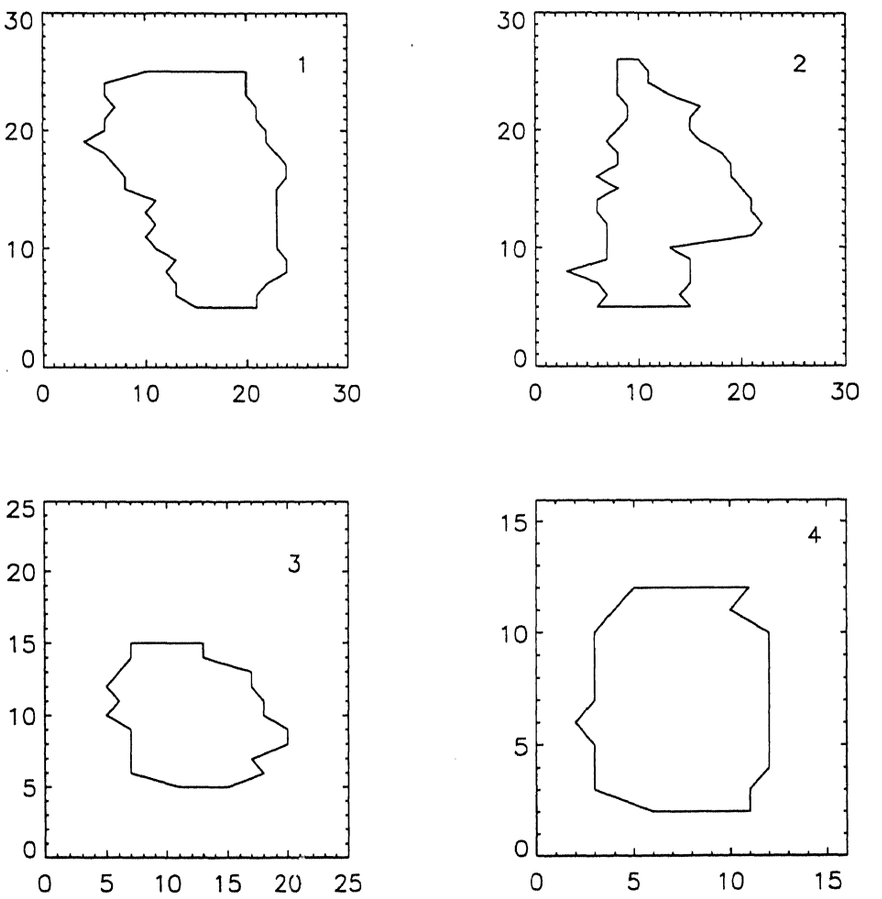

Figure 3.4: Outlines of 4 quiet cells. The last cell shows a surprising degree of regularity, which is reflected in its large compactness of 0.82. Note that the cells are shown on different scales.

cells, and we too refer to them as such, strictly speaking, SGs are probably overshoots of the true convective cells which may be invisible. Worden (1975) notes that the negative temperature gradient of SGs observed at the deep photospheric layers is insufficient to account for any significant fraction of the solar luminosity. Furthermore, it is unlikely that true convection can occur in a well stratified layer like photosphere where radiation is the chief energy transport mechanism.

The maximum relative contrast ΔI, which is a measure of the ratio between the maximum and mean intensity of the cell, is evaluated according to Eq. 3.1. While scanning the images, the intensity of the peaks as well as that of the minimum was noted. The maximum intensity I_{max} for each cell is found by averaging the intensity value of all boundary points. The cell minimum I_{min} value is obtained as the minimum of the scan minima.

$$\Delta I = 2 \times \frac{I_{\max} - I_{\min}}{I_{\max} + I_{\min}} \tag{3.1}$$

The contrast in temperature between the boundary and the mean interior, ΔT, is given for small contrasts by:

$$\Delta T = \frac{\Delta I}{4I} T, \tag{3.2}$$

assuming a Planck spectrum. The band-width of the filter used in the Antarctica data was 1.2 Å, and thus includes the entire K_{232} profile. We estimate that the temperature at which the line forms is about 7000 K (Vernazza, Avrett & Loeser 1981). The data for ΔI obtained by the scanning, and the resultant temperature contrast are given for 10 cells in Table 3.2. The mean temperature obtained by us is corroborates quite well the value of about 230 K quoted by Worden (1975) for the lower chromosphere (Table 1.6).

If we assume that supergranular convection sweeps magnetic flux to cell edges (Simon & Leighton 1964), then the flux at the wall of a cell will be proportional to L^2, where L is the length-scale of the cell. Assuming that

No	Area (10^8 km^2)	contrast (%)	ΔT (K)
1	14.7	18.7	327
2	10.5	14.4	252
3	7.4	13.5	236
3	6.9	13.0	228
4	6.3	12.5	219
5	6.1	12.8	225
6	5.9	9.2	161
7	5.7	10.4	182
8	4.9	16.9	296
10	3.1	14.6	255
mean	7.1	13.5	236

Table 3.2: Cell intensity contrast and temperature contrast as a function of sizes for 10 cells.

the flux is spread out evenly along the circumference, we find the resulting field strength will be proportional to L.

A plot of intensity contrast against cell area, got from Table 3.2, is given in Fig 3.5. The data shows considerable scatter, but a marked trend for larger cells to show greater contrast. This in turn strongly suggests a temperature contrast, and consequently, stronger magnetic fields at cell boundary. This is also in conformance with the observation of Sýkora who noted that network enhancements in the vicinity of very large cells leading eventually to the formation of active regions (Sýkora 1970).

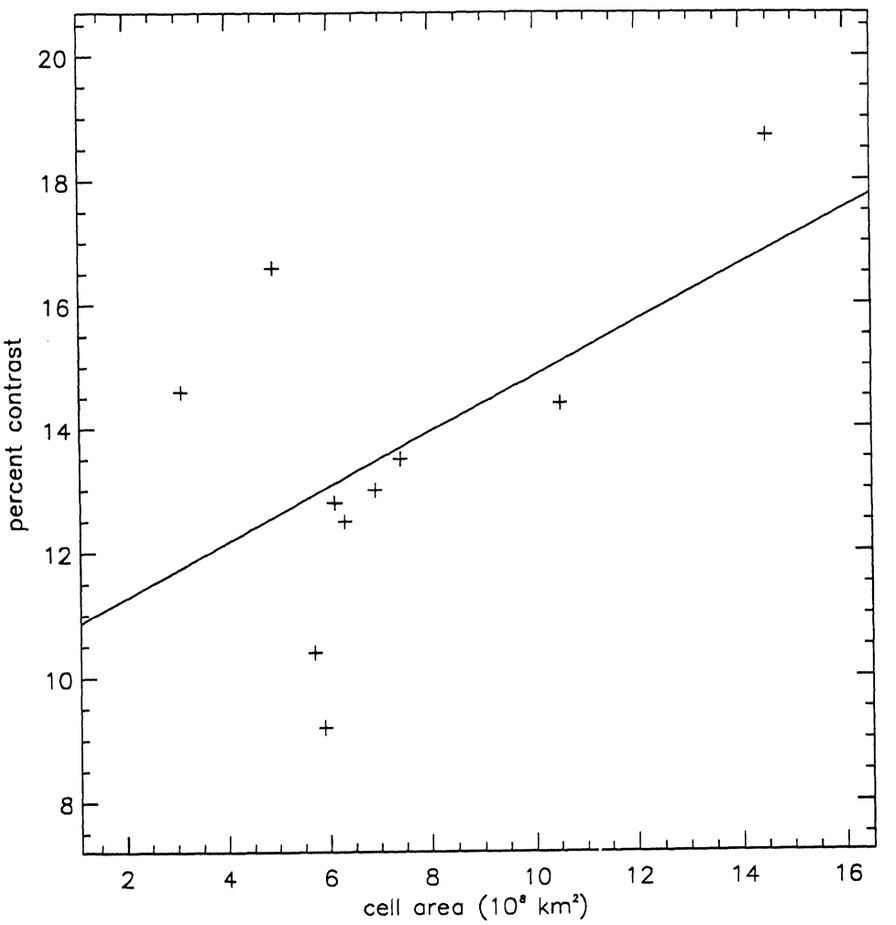

Figure 3.5: Scatter plot of cell contrast against cell size. There appears to be positive trend between the two parameters.

Chapter 4

The chromospheric network length-scale

Knowledge of the interrelation between basic supergranular parameters like size, lifetime and activity level is relevant to the understanding of the convective processes that produce SGs and CNCs and how they interact with magnetic fields. In this chapter we study the CNC length-scales, and their possible dependence on latitude, magnetic fields and solar rotation. Length-scales have been derived using the autocorrelation (AC) method.

4.1 Introduction

The length-scale of SGs has been esimated in many ways including AC, Fourier transformation, and visual inspection. In Table 4.1 we report some estimates in the literature. In much of this report, we do not differentiate between the length-scales of SGs and of CNCs.

Some of the methods employed in determining length-scales are discussed below.

Investigators	Length Scale (Mm)	Method Used
Hart (1956)	26	AC: Hα Dopplergram
Simon & Leighton	32.5	AC: various chromospheric and photospheric lines;
	25	Microphotometer tracing
Janssens (1972)	28	visual inspection: Hα
Duvall (1980)	30	AC: Fe I 8688
Giovanelli (1980)	$\sim$ 30	AC: Fe I 8688
Sỳkora (1980)	32–37	K filtergram AC
Singh & Bappu (1981)	32	AC: K spectroheliograms;
	23	grid counting: K line
Brune & Wöhl (1982)	22–31	visual inspection: Ca K
Raju et al. (1998a)	30-35	AC: Ca K

Table 4.1: Length Scale Estimates of CNCs and SGs

Visual inspection methods

In the method used by Singh and Bappu (1981), the solar disk is projected onto a grid. The number of grid squares enclosed within a pattern is read off as its area.

Brune and Wöhl (1982) have used K line photographs to measure cell sizes by taking diameter measurements along 4 axes (N-S, E-W, NE-SW and NW-SE) using high precision callipers. The cell size was computed as the average of these measurements. Error was estimated by repeating the measurements and noting the differences.

Küveler (1983) has derived SG sizes from Fe I 6301.517 Å Dopplergrams. These photospheric images were intergrated over 10 min to remove 5-min oscillation effects. The velocity cells were obtained by interpretting iso-Doppler contours after interpolating the image with a 2D 5th order polynomial. He finds about 86% correlation between the chromospheric network and the velocity cells.

Autocorrelation length-scales

AC is calculated by setting $\tau = 0$ in Eq. 2.1:-

$$\mathrm{AC}(\Delta) = (1/N) \int_A I(t,r) I(t, r+\Delta) dA, \tag{4.1}$$

Scales are determined as full width at half maximum (FWHM) or secondary maximum (SM) of the AC curve. A host of investigators have used the AC method (section 4.2) to determine length-scales (Table 4.1). It is of interest to note that Singh & Bappu (1981) quote an AC size (32 Mm) larger than the size obtained by inspection (23 Mm). They attribute the discrepancy to the fact that their inspectional method counts only half the wall contribution. In section 4.2, we attribute it to intercellular spaces.

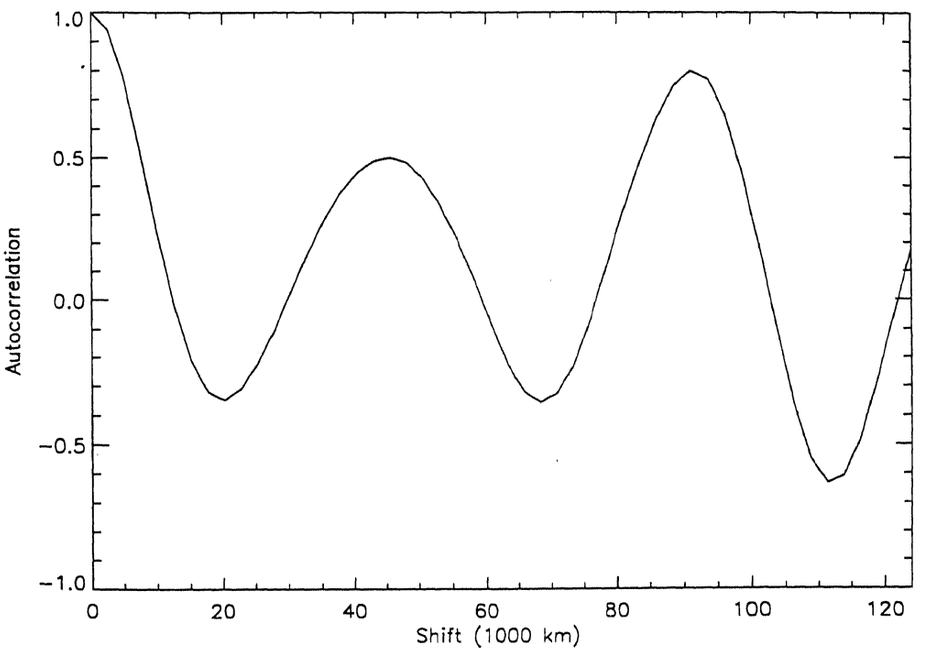

Figure 4.1: Autocorrelation on a narrow strip 320″ × 16″ in area. The narrower and smaller strips show, at times, very good correlation pattern, but are in general less reliable.

By using Fourier transformations

Standard algorithms such as FFT are used to compute the power spectrum of the images. Münzer et al. (1988) have computed mean length-scale using the power-spectrum by weighting spatial frequencies with their power from K line image FFT spectrum.

4.2 Methodology

Choice of region

The total input data consisted of a time-series of images. The region or "window" chosen for a given correlation run was, in general, either quiet, semi-active or active (Chapter 5). The AC technique as applied to obtain cell size was confined to quiet windows. The geometry of non-quiet regions is quite complicated and often irregular, so that length-scales in those regions are best studied by visual inspection.

Size and shape of the autocorrelation window

The correlations were run in small regions of interest, or "windows", cut out from the entire image. We have chosen windows in the range from $160'' \times 160''$ to $230'' \times 230''$. When a window is much smaller than this, it is statistically less reliable. When by coincidence the scatter in size is low, a small window can give a good AC pattern: eg., in Fig 4.1, AC obtained from a rectangular strip $320'' \times 16''$ (500 pixels). The tertiary peak rises as high as 0.75. However, being statistically less stable, small windows often return amorphous AC patterns.

In Fig 4.2 we present a typical autocorrelation pattern of the quiet chromosphere obtained from a larger, $160'' \times 160''$ window (2500 pixels). The undulations in this graph are clearly more broadened and gentler than that in the smaller window, Fig 4.1: its troughs almost never swing to negative value. We find that larger windows more often than not return a well-defined repetitive pattern. For this reason, for statistical studies involving a large number of windows, in which we wish to automate the process of extracting length-scales by a software program, a larger window is preferable. The upper limit restriction to windows comes from the need to keep projection effects low and to confine the window to a given level of activity.

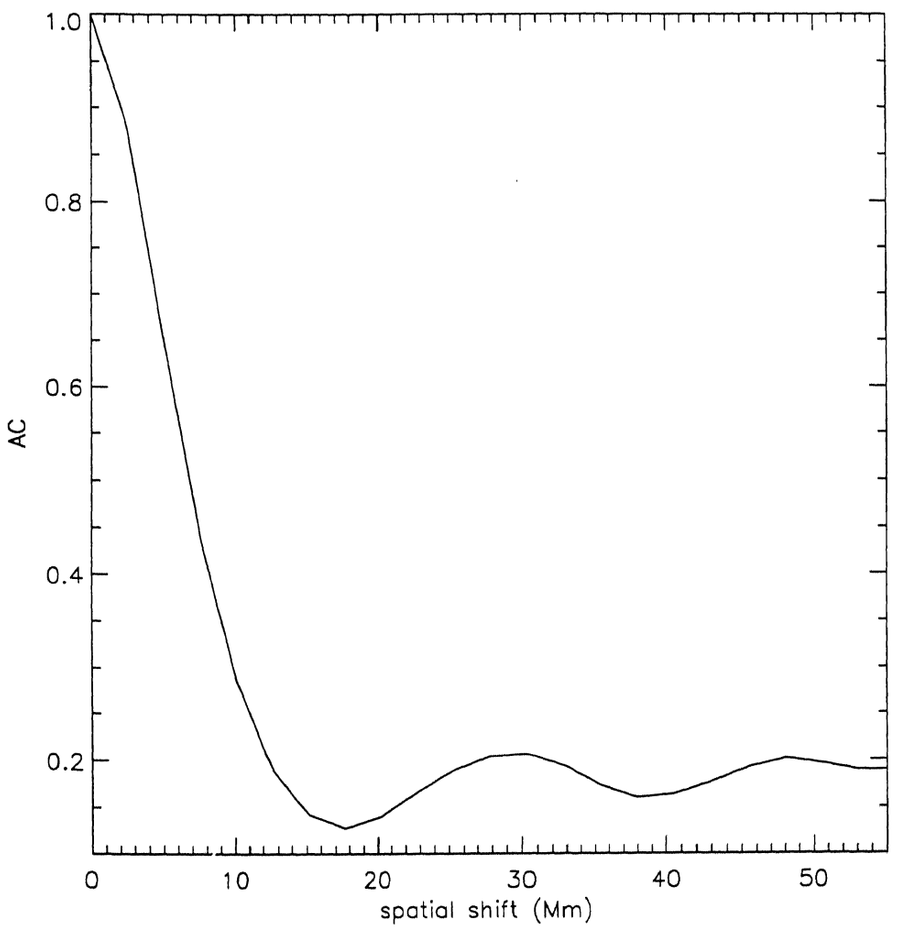

Figure 4.2: Autocorrelation on a window measuring 160″ x 160″ obtained along one axis. Each pixel corresponds to 3.2″.

No.	Parameter	Value
1	Mean cell size	34.1 Mm
2	Most probable cell size	33.5 Mm
3	Maximum cell size	43.8 Mm
4	Minimum cell size	30.6 Mm

Table 4.2: Some AC length-scale parameters of K line CNCs

Computing the autocorrelation length-scale

Computationally, autocorrelation is calculated by evaluating Eq. (2.3) $\tau = 0$:

$$AC(\Delta) = (1/N)\langle \delta I_t(r) \delta I_t(r+\Delta) \rangle, \tag{4.2}$$

where:

$$\delta I(r) = I(r) - \langle I(r) \rangle.$$

and:

$$N = \sqrt{\langle \delta^2 I_t(r) \rangle \langle \delta^2 I_t(r+\Delta) \rangle}$$

Fig (4.2) is a typical quiescent AC pattern. Spatial shift to the secondary maximum (SM) is taken as the length-scale of CNCs (Rogers 1970; Singh & Bappu 1981). The error bar in length scale estimate is 2 300 km, which is the pixel size of the images.

Some of the typical parameters pertaining to cell autocorrelation length-scales found by us are listed in Table 4.2. They corroborate the traditional values listed in Table 4.1.

AC length-scale does not represent the mean size of cells, but the mean size of the cell plus intercell spacing. In other words, it is the mean distance

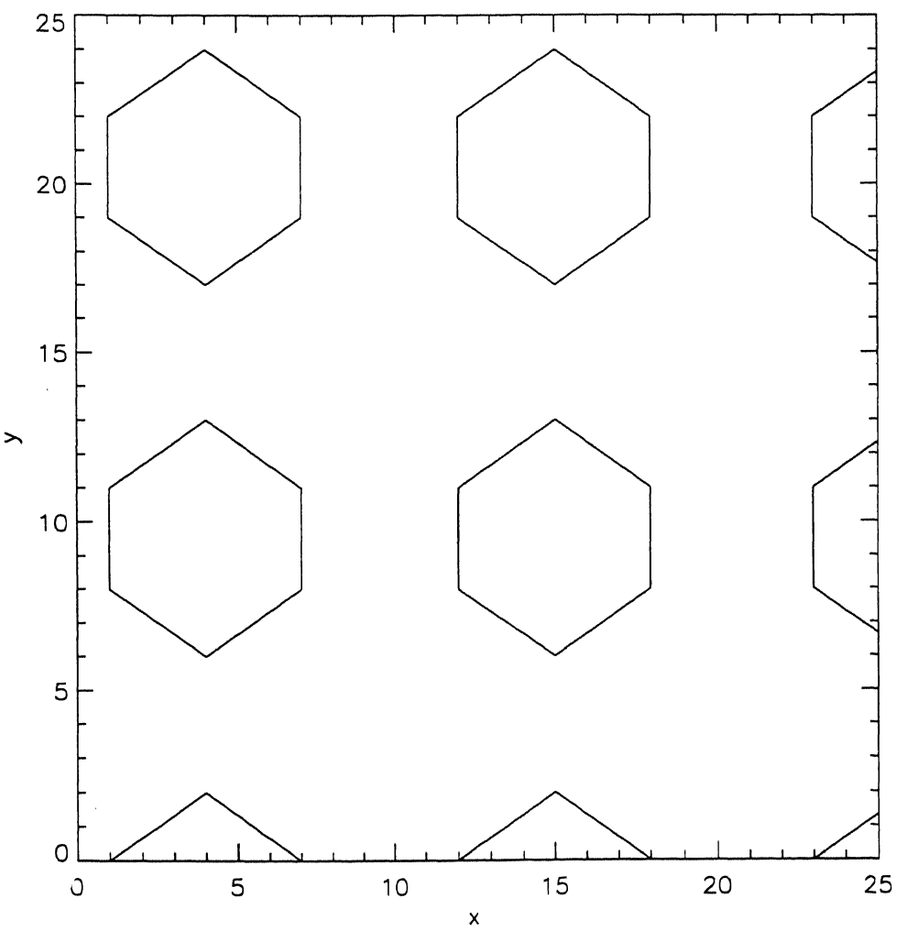

Figure 4.3: Artificial pattern of hexagonal cells with a cell size (maximum width along x-axis) of 6 units and intercell (intercellular space) size of 5 units (minimum distance along line parallel to x-axis connecting two adjacent cells). The cell boundary has a uniform intensity of 5 units, while all other regions– cell interiors and intercells– have intensity 1.

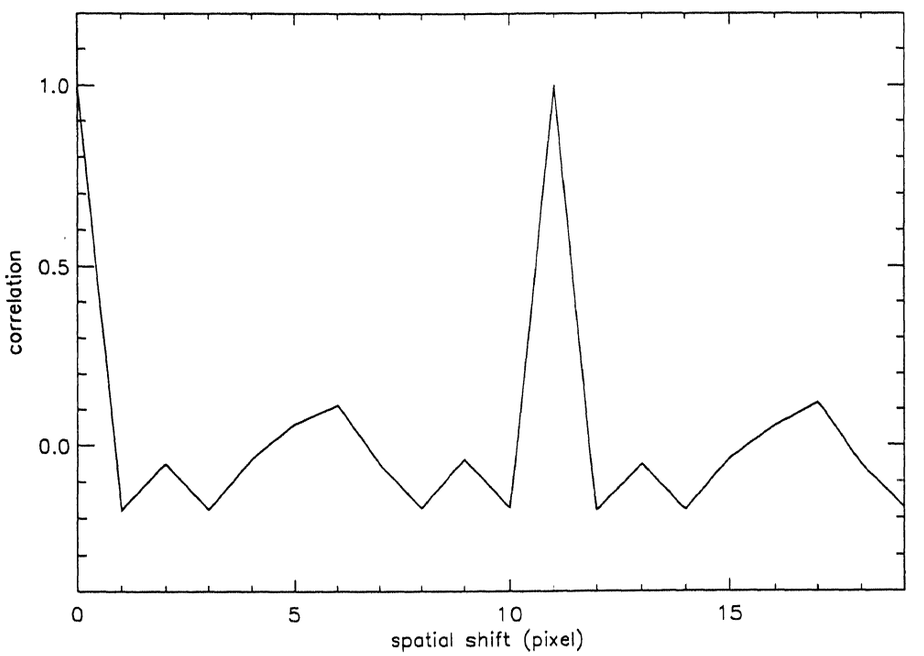

Figure 4.4: AC for Fig 4.3. We note that the SM corresponds not to the cell size but the combined size of the cell and intercell spacing. SM will correspond to actual cell size only if the cells are tightly packed, and thus compeletely tile the surface.

between the centers of adjacent cells. In Fig 4.3, we show an arbitrary pattern of regular hexagonal (for simplicity) cells of uniform size and regular intercell spacing. The size D of the cells along the horizontal direction in the non-tapering part is 6 length units. The intercell width along this line is 5 length units. The walls of the cell are one unit thick with intensity of 5 units. All non-wall regions- both cell interiors and intercells- are of 1 intensity unit.

Fig 4.4 gives the AC derived from Fig 4.3, for spatial shifts along x-axis. We find that although there is a weak signal corresponding to the length-scale of D, a stronger secondary maximum manifests itself at the spatial shift $D + d = 6 + 5 = 11$. If the cells completely tile the surface in a compact configuration, then $d = 0$, and the AC scale equals the size of the cell. Thus, the AC scale represents an upper bound on the cell size. It is worth noting that a similar discrepancy is well attested in the case of granules, where the intergranular size is typically the granular size added to twice dark lane thickness. Probably this explains the discrepancy between length-scales obtained by visual and AC techniques (Simon & Leighton 1964; Singh & Bappu 1981; see Table 4.1).

4.3 Latitude dependence of cell size

In Section 3.2, the observational details for studying size as function of latitude was given. Strips of width 5° running parallel to latitudes were used to derive AC length-scales.

A strip of length L laid parallel to the equator will subtend an angle ϕ_0 at the solar center given by:-

$$Sin(\phi_0) = \frac{L/2}{RSin(\theta)} \tag{4.3}$$

where θ is the latitude position of the strip. According to Eq. (4.3), the strip extends in the limit 14° W to 14° E extension at the equator and extends in the limit 22° W to 22° E at 50°.

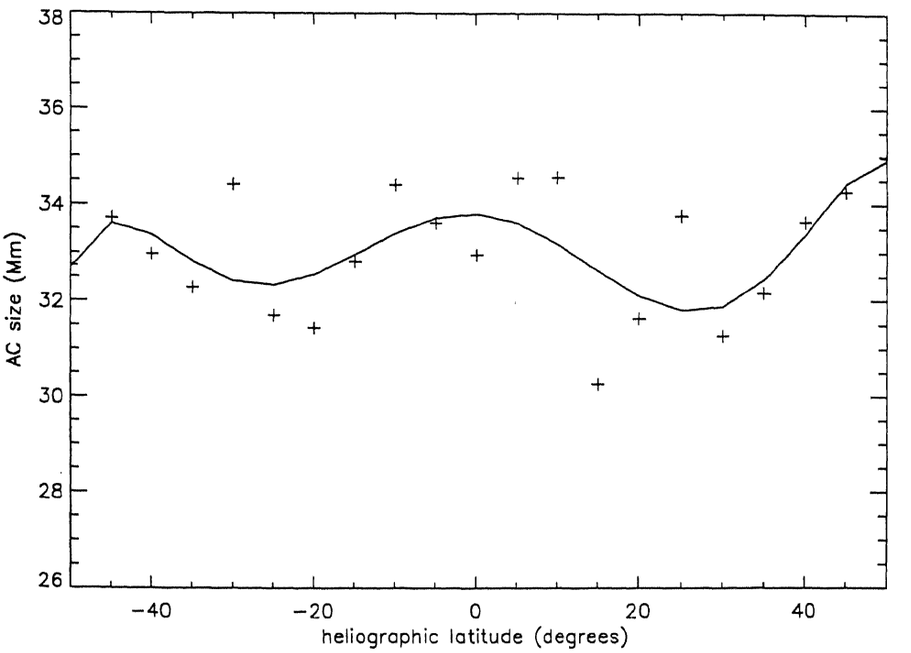

Figure 4.5: Mean cell sizes plotted against heliographic latitude. The solid line represents a 6^{th} order polynomial fit. We find that the fit brings out the north-south symmetry in the data.

The spatial autocorrelation function $AC(\Delta)$ was computed using Eq. (4.2) by sliding the strips along the equator. It was found that the secondary maximum was well defined in over 80% of the cases. The correction to foreshortening was applied after the autocorrelation was measured. The foreshortening correction at a given longitude ϕ is $(\mathrm{Cos}(\phi))^{-1}$ for an infinitessimal area (Raju et al. 1998b).

For the tips of the strip, this factor is, in view of Eq. (4.3) $k = (Cos(\phi_0))^{-1}$ where ϕ_0 is given by Eq. 4.3. The average foreshortening is obtained averaging k, the foreshortening factor over the whole strip. We find the average foreshortening is about 1.6% at the equitorial strip and 4.2% at

50°. Table 4.3 gives the projection-corrected values of mean cell size derived for various latitudes, and the number of measurements at each latitude.

The large standard deviations seen in the cell sizes may be attributed to the intrinsic diversity in supergranular sizes. Fig 4.5 plots the mean cell size values against latitude. The solid line represents a 6th order polynomial fit. It is seen that cell-sizes show a variation with latitude. In specific, there appears in the fit a fairly good North-South symmetry, with global maximum at the equator. A slight asymmetry is seen in that scale values are slightly larger to right extreme than the left extreme. The Table 4.4 was extracted from Table 4.3, to give information regarding occurance of maxima and minima in the 15–30° N and S belts.

The latitudinal distance in each hemisphere between the maximum and minimum in these belts is found to be 10°. The latitude dependence of supergranules is in contrast to granules, for which no such dependence has been reported (Muller 1989).

4.3.1 Magnetic field effect

To explain the latitude dependence of the cell sizes, we must look for phenomena which show a similar property. QS magnetic field is one such. According to the dynamo theory of Parker (1950), the strong magnetic fields associated with sunspots originate in the convective overshoot region between the convection and radiative zones of the Sun. An initial poloidal magnetic field, because of the differential rotation of the Sun, evolves into a toroidal field. The toroidal component runs parallel to latitudes underneath the surface. Tension in the field lines causes portions of it to erupt to the surface through the development of buoyant forces to form sunspot groups and active regions. At the surface, the magnetic field lines are almost vertical, sometimes rising to coronal heights before returning to the surface as the opposite polarity.

At any given epoch of the solar cycle, the birth of sunspots is predomi-

No.	latitude	No. of measurements	Mean size (km)	σ (km)
1	-50	42	32 735	7033
2	-45	37	33 727	8363
3	-40	52	32 976	9178
4	-35	56	32 284	10 370
5	-30	52	34 417	8342
6	-25	51	31 704	8648
7	-20	51	31 433	8694
8	-15	57	32 818	8566
9	-10	52	34 407	9010
10	-5	50	33 626	8453
11	0	48	32 964	9469
12	5	53	34 548	8102
13	10	53	34 560	9926
14	15	56	30 264	7776
15	20	55	31 639	7983
16	25	53	33 768	8651
17	30	51	31 278	8146
18	35	53	32 169	8249
19	40	55	33 653	9934
20	45	36	34 265	8765
21	50	39	34 974	7766

Table 4.3: Correlation sizes of Ca II K network cells as a function of latitude

Extremum of size	value	Latitude
Maximum	34 417	30° N
	33 768	25° S
Minimum	31 433	20° N
	30 264	15° S

Table 4.4: Maxima and minima for the two hemispheres in the 15-30° belt

nantly along one latitude in the 0–30° belt in each hemisphere. The so-called Butterfly diagram traces the locus of birth-regions of sunspots during the solar cycle. At the beginning of solar cycle, sunspots are born predominantly at ±30° and migrate equator-wards. Harvey (1994) has reported that network fields appear to follow active region fields. Thus we can expect QS network fields to show a similar latitude dependence.

The strips used in the analysis were taken during the solar minima. At this time active regions of the new solar cycle are on average born at ±30° and active regions of the past cycle have converged at the equator.

Chandrasekhar (1961) showed that magnetostatic equilibrium requires convective cells in stronger magnetic fields to be smaller. For example, a 15% increase in magnetic field is expected to induce a 5% reduction in cell size. This is also qualitatively consistent with the findings of Singh & Bappu (1981) who have reported a decrease of about 5% in CNC sizes during solar maximum as compared to the minimum. Zwaan (1978) reported that cell sizes decreases close to active regions. In this scenario, a cell size maximum around ±15°, and minima at ±30° and the equator is expected. However, the minima in Table 4.4 are close to ±15°, while the maxima are close to ±30°. Perhaps, more significantly, the equatorial rise remains unexplained.

On the other hand, the observational evidence by Sýkora (1970), Wang

(1988b) and Münzer et al. (1989) suggests that length-scales increase near active regions. If this is true, the equatorial and $\pm 30°$ rises can be attributed to the averaged fields of the new solar cycle and the old one, respectively. The minima around $\pm 15°$ can be attributed to the averaged fields of the intervening weakening of the fields between the two active latitudes. According to Sýkora (1980), active regions originate in the vertices of large SGs since they are likelier to concentrate stronger fields at the vertices. In this scenario, we expect a relative depression in sizes in the intervening belt between the equator to $\pm 30°$. The expected depression occurs somewhat beyond the mid-latitude between these two belts, which is not inconsistent with Table 4.4. Muller & Roudier (1994) have reported a variation with latitude of network BPs. This suggests the existence of other observational parameters dependent on latitude.

4.3.2 Solar rotational effect

In principle, solar rotation can have a latitude effect independently of magnetic fields. Rossby number $\mathrm{Ro} \equiv (v/\omega L)$ gives a measure of dominance of inertial effects over Coriolis force effects. In the solar context: v is horizontal velocity in the cell, ω Sun's rotational frequency and L is a typical cell size. The effect is larger for larger scales. Taking $v = 400$ m s^{-1}, $\omega = 3 \times 10^{-6}$ and $L = 30$ Mm, the Rossby number is about 4.4, which is not too great to exclude an influence of rotation. This produces vortex flows, so that the line of zero-velocity in cells is not perpendicular to the ray connecting the cell to disk center. Such an effect of Coriolis force has indeed been detected (Kucera 1988).

Another latitude effect possibly linked to rotation was first reported by Brune and Wöhl (1982). They have noted a decrease in cell size by about 10% going from the equator to $\pm 60°$. They attribute this observed latitude dependence to rotational effects, though it still not clear how rotation can

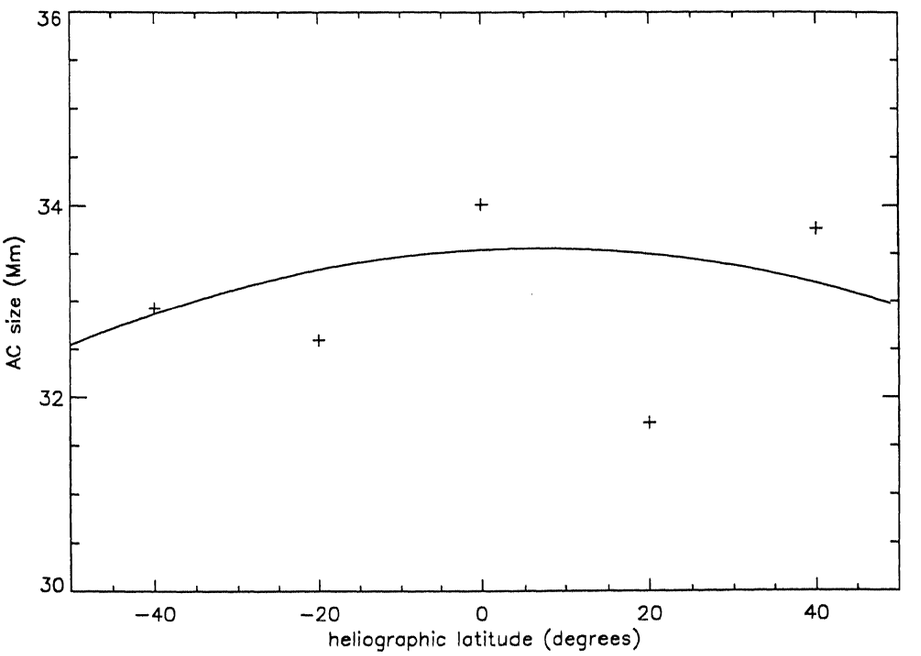

Figure 4.6: Fig 4.5 after a 4-point averaging. Bin size of about 20° used, except at the equator where it 25°. The solid line represents a quadratic polynomial fit.

affect sizes. A similar dependence is noted by Münzer et al. (1988).

Brune & Wöhl use latitude bins of 20°, whereas Fig 4.5 uses a 5° bin. Wide latitude binning is expected to smooth out the effect of magnetic fine structure and leave only rotational effects. To make the results comparable, we performed a 4-point averaging on our data to increase our bin-size four-fold, except the equatorial bin which is 5-point averaged, since the number of data points in Fig. 4.5 is 21, a non-multiple of 4. This results in only 5 data points, with the equatorial belt with bin-size 22.5° and the other four with 20°. Although the number of data points is less, over 200 cell size measurements go into each data point, making the data fairly statistically significant. The result of the 4-point averaging is given in Fig (4.6).

Examination of the data points suggests that the cell sizes fall at higher latitudes. We note the two large dips at $\pm 20°$ corresponding to the effect probably of magnetic fields. A quadratic fit to the plot with suitable weighting to the data-points is given as the solid line determined by: $L = 33550.0 - 4.068 \times \theta - 0.322 \times \theta^2$, where L is cell size in km and θ is the heliographic latitude in degrees. The presence of the small term linear in latitude implies a slight latitudinal asymmetry. The central value is 34 021 km in the data, while the mean value at $\theta = 60°$ is 32 633 km as obtained from the fit. This represents a reduction in cell size by a factor of 4.1% compared to its equatorial value. This corroborates the results obtained by Brune & Wöhl (1982), who found sizes at $\pm 60°$ to be about 0.9 times the equatorial value.

This suggests that cell sizes have a composite dependence on latitude, with magnetic field effects modified by rotational effects. In Fig 4.7 we show a simple model of the combined effect of the two factors. An initally purely magnetically affected size profile (dashed line) and a purely rotationally affected size profile (dotted line) combine to give the resultant (solid line) which is comparable with Fig 4.5.

We have modelled the purely magnetic profile as Gaussian peaks at $0°$ and $\pm 30°$ (Howard & LaBonte 1981; Stenflo 1988; Howard 1988) with FWHM of 11.7 Mm and an amplitude 1000 km. These values were chosen since they fit the observed data in Fig 4.5 fairly well. The purely rotationally affected profiles as coming from only the quadratic (and hence symmetric, for simplicity) part of the fit derived from Fig 4.6.

One observation not explainable by magnetic field effects alone that becomes clear in the composite model is the lower peak heights at $\pm 30°$ than at the equator. According to the model, the values at these latitudes are about 30 600 km, or 0.986 times that of the equatorial value. By averaging the central 5 values in Table 4.3, we estimate the equatorial value to be 34021 km; from Table 4.4 we find the average $\pm 30°$ value to be 32848 km. This

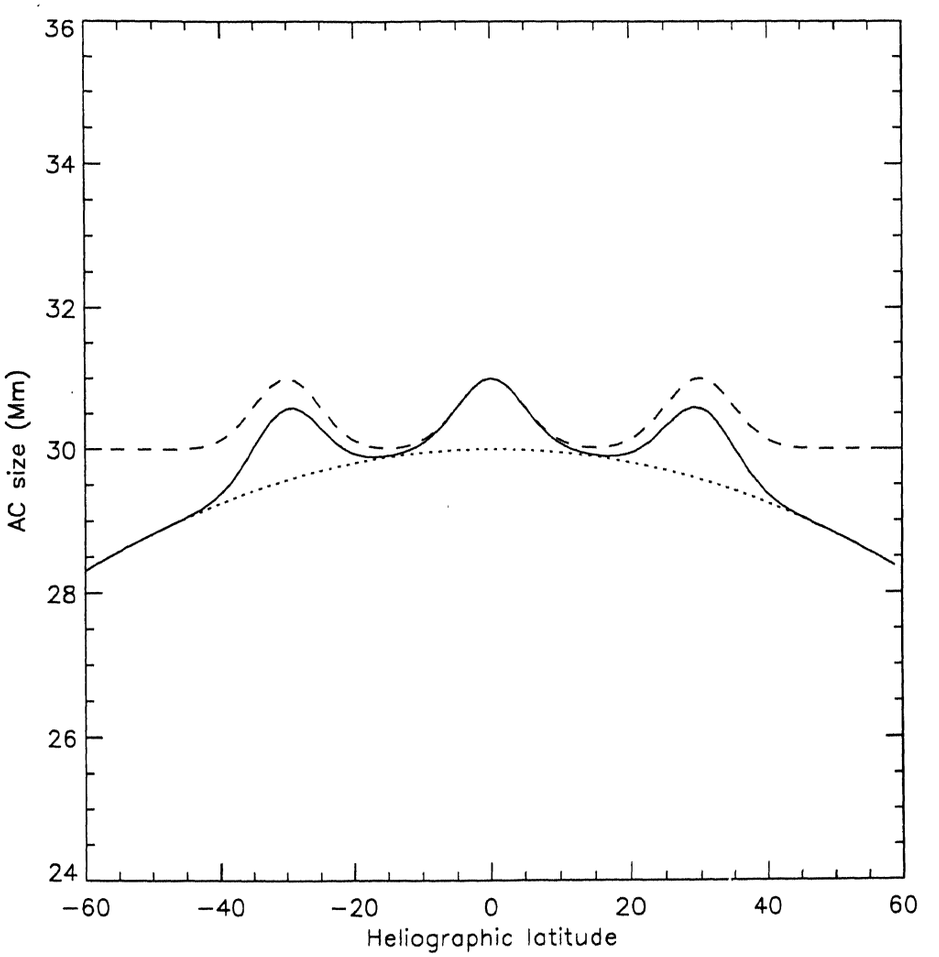

Figure 4.7: Composite latitude effect on autocorrelation size of network cells. The dashed line is due to a purely magnetic field effect, the dotted line entirely due to a possibly rotationally induced effect. The solid line is the resultant of their combined effect.

gives a reduction factor of 3.45% with respect to the equatorial size.

Another observation that is compatible with the composite model is the advancement of the minima that would be expected at ±15°. In Fig 4.7, the expected minima will be at ±15°, which are local minima of the purely magnetic profile. The solid line clearly shows the effect of the rotation-induced profile whereby the minima shift to the higher latitude level of ±19°. This happens because of the "filling up" of the valley in the magnetic profile in an uneven way by the rotation profile by the rotation profile.

The sizes at ±60° in Fig 4.7 are 0.91 times their equatorial values, which is comparable with the observed values obtained in Fig 4.6 and by Brune & Wöhl (1982), Münzer et al. (1988). This result also perhaps explains the apparent flattening of cell sizes in the direction perpendicular to the equator (Sýkora 1970).

4.4 Cell boundary thickness

Since magnetic fields are stronger in the network than in the interior, the dynamics of the network is expected to be different from the interior. The flocculi that constitute the cell walls evolve differently than the cell interior. Singh & Bappu (1981) and Raghavan (1983) report that cell boundary thicknesses do not show any appreciable variation during the course of the solar cycle. Skumanich et al. (1982) have noted no marked change in QS during the course of the solar cycle.

AC primary peak-width may be used as a rough estimate for cell walls. The AC curve is dependent on three factors: (a) mean cell sizes, (b) cell size scatter in the window, and (c) the cell boundary thickness (and other small scale structures). Mean intercell distance is reflected in the distance between successive peaks, and scatter of sizes by the lowness of secondary and later peaks. Small scale structures, which is the cell wall in our images, are reflected in the steepness of fall of the primary peak.

No.	FWHM (″) of Gaussian	SM (Mm)	FWHM (Mm) of PM
1	0.	28.50	13.8
2	1.65	28.50	15.5
3	2.48	28.50	17.62
4	3.30	28.50	19.9
5	4.95	28.50	26.8

Table 4.5: SM, primary peak FWHM, height H of SM, the height- difference ΔH between SM and the primary AC trough of the AC curves of Fig 4.8.

In Fig 4.8, we present the result of smoothing an image by convolving it with Gaussians of varying FWHM. The effect of smoothing is to reduce contrast by broadening bright structures like cell walls. However cell sizes remain unaffected. This is reflected by the increase in peak-width of the primary peak, and the contrastive constancy of SM. The results of the smoothing are presented in Table 4.5.

Cell wall defined as twice the length-scale corresponding to AC = 0.75 returns a value about 7000 km, roughly equal to existing cell-wall estimates (Singh and Bappu, 1981). Furthermore, most AC curves are smooth upto and slightly beyond the 0.75 value, which is important for a reliable interpolation.

Fig 4.9 is a close-up view of Fig 4.2. The shift corresponding to AC = 0.75 is obtained by linear interpolation, indicated by the dashed line. In Fig 4.9, this gives wall length-scale of 4.43×10^3 km, or a wall estimate twice that value.

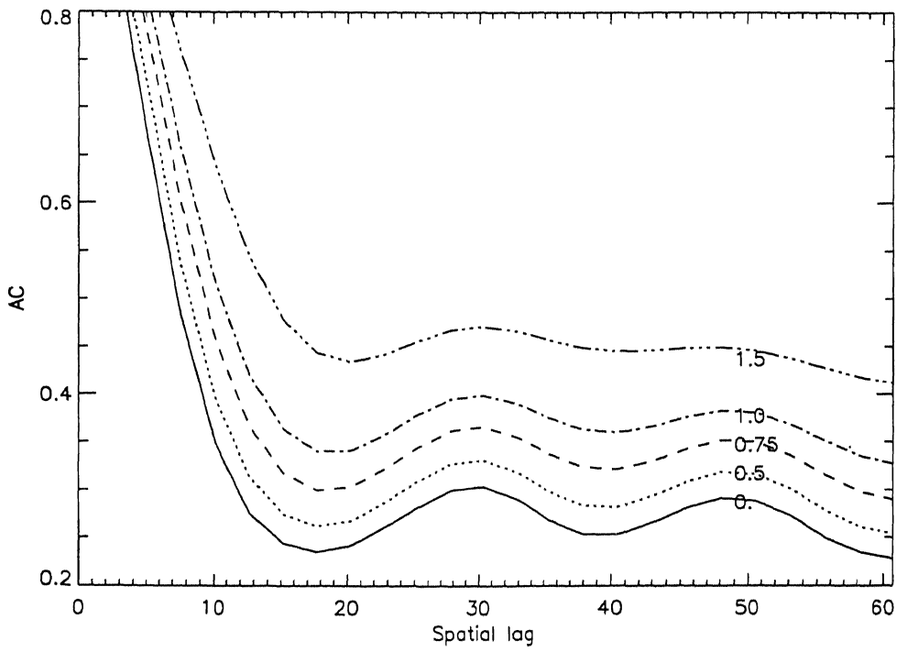

Figure 4.8: AC pattern for various smoothings on a 230″ x 230″ QS window. Labels of curves multiplied by pixel size give the FWHM of smoothing Gaussian. We note the stability of SM, which is considered as the charateristic mean length-scale. Spatial shift to the primary minimum, FWHM, peak height H of SM, and height difference ΔH between SM and primary trough change.

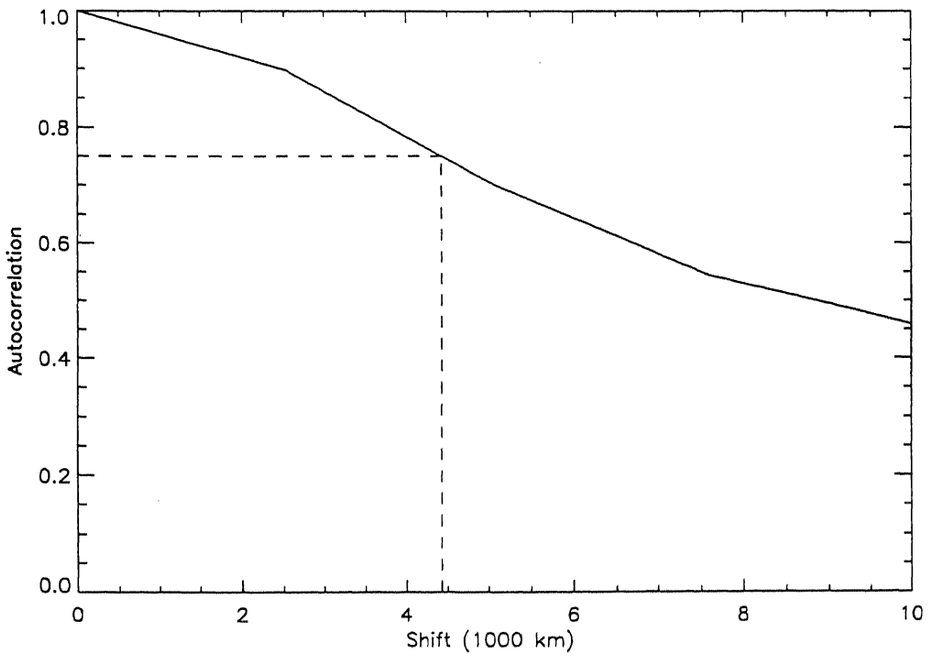

Figure 4.9: Close-up of the initial part of Fig. 4.2. The dashed line points to an AC length-scale of 4.43 Mm, corresponding to AC = 0.75.

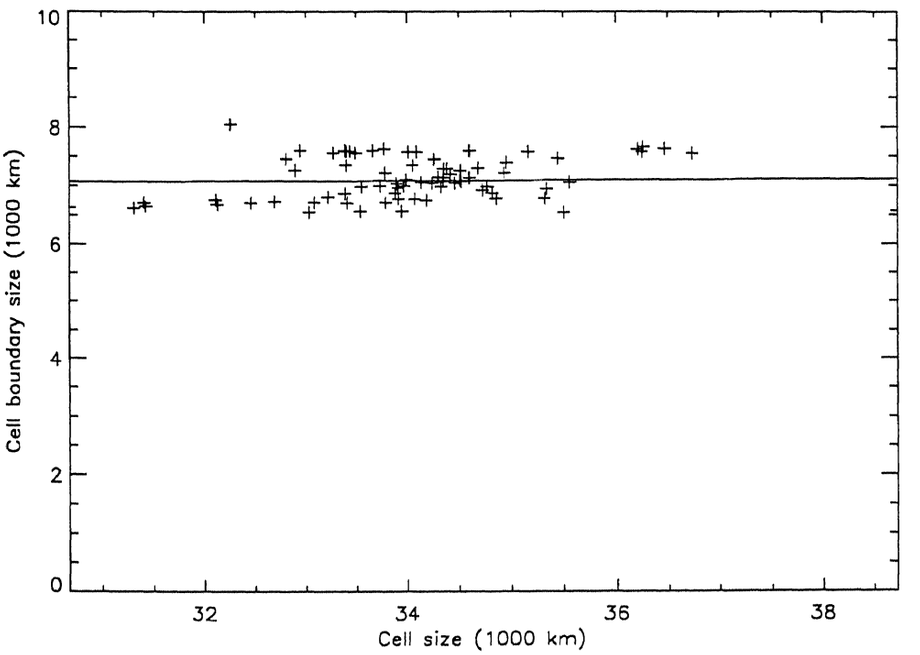

Figure 4.10: Cell boundary thickness, estimated as primary peak-width corresponding to correlation 0.75, as function of cell size. The two show little dependence

4.4.1 Dependence of peak-width on Activity

We have qualitatively distinguished three levels of activity: quiet, semi-active, and active regions (Chapter 5). The term semi-active refers to regions close to plage regions, which show an intermediate level of activity.

The cell-wall interprettation of peak-width cannot necessarily be extended to semi-active and active regions because of interference from the irregular plage regions. Instead, it can be thought of as an inverse measure of spatial fluctuation.

The peak-widths were all derived from small ($100'' \times 100''$) windows in order to confine the window to a single level of activity. Since the peak-

No	Region	AC peak width (km)
1	QS	6 000
2		6 600
3		6 680
3		6 700
4		6 800
5		7 030
	QS mean	6635
6	semi-active	8 300
7		9 300
8		10 300
	Semi-active mean	9 300
9	Active	12 300 km
10		12 700
11		12 900
	Active mean	12 630

Table 4.6: Peak widths of the AC primary peak at 0.75 correlation for different levels of activity

widths are sensitive to image quality, each value was derived as an average of values over about 1 hour. Results of this work are presented in Table 4.6.

We find that QS peak widths are smallest and active region ones are largest. Active peak widths are almost twice the QS value, while semi-active peak-widths are about 50% larger than the QS value. This implies that active region intensity topography is composed of low spatial frequency features.

4.4.2 Dependence of cell boundaries on cell size

Eighty two QS windows, measuring $160'' \times 160''$, were chosen to study the relation between cell size and cell wall thickness. Cell size in each window was derived as the average of AC SM for over 140 frames, while cell-widths were derived as the average of 0.75 peak width length-scale over the same images. The problem of alignment of the images is treated in section 5.2. The resulting scatter plot is given in Fig 4.10. It shows no obvious trend, with a correlation close to 0.0.

We note that the above null result, strictly speaking, applies to QS alone. In section 4.3 we argued that magnetic fields might affect cell sizes, and in section 4.4.1 that they affect peak widths, too. If these propositions are true, then this means that cell sizes and wall thickness should be correlated, at least as far as their dependence on magnetic fields is concerned. Nonetheless, this does not necessarily contradict the result of Fig 4.10 because, whereas the activity-dependence of peak-widths involves active regions, Fig 4.10 and the results of section 4.3 pertain to QS. According to the arguements presented in section 1.4.2, the effect of magnetic fields need not be similar in QS and active regions. The low magnetic field strengths and large size dispersion in cell sizes explain the negative result of Fig 4.10. This corroborates the the results of Singh & Bappu (1981) and Raghavan (1983) who find that cell walls remain unchanged during the solar cycle even though cell sizes vary.

Chapter 5

The evolution and lifetime of the chromospheric network

5.1 Introduction

Lifetime is an important CNC parameter. Assuming a convection model, lifetime allows us to make estimates on the velocity and temperature fields of SG. If SG velocity fields are indeed responsible for the diffusion of active region magnetic fields (Leighton 1964, 1968) then SG lifetime constrains the time-scale of break-up of active region (Duvall 1980). Studying lifetime dependence on other parameters like activity and length-scale can help us relate the dynamics of cells to their morphological properties.

Some of lifetime estimates are summarized in the in Table 5.1, where lifetimes derived from CN and SG have not been distinguished. Depending on the method chosen, observers have come up with values in the range 20–50 hr.

Lifetimes determined morphologically

In the method of Janssens (1970), Hα network cells in a control group were graded from 0 to 3 depending on how well they were formed. A total for

Investigators	Estimate (hours)	Method
Simon and Leighton (1964)	20	CC: Ca K spectroheliogram
Janssens (1970)	21	morphological study of Hα filtergram
Rogers (1970)	25/38	CC: Hα filtergram
Worden (1975)	30	CC: infrared images
Worden & Simon (1976)	36	CC: magnetic observations
Duvall (1980)	42	CC: Fe I 8688 Å
Wang (1988)	40	Hα Dopplergram
Wang & Zirin (1988)	> 50	Visual inspection
Singh et al. (1994)	22	morphological study of Ca K filtergram
Raju et. al. (1998a)	25	CC: Ca K filtergram

Table 5.1: Lifetime estimates of CNCs or SGs.

a group of cells is taken. Lifetime is determined by studying how this total changes.

Singh et al. (1994) estimate lifetime as the difference as between t_d, epoch of decay, and t_f, epoch of formation, the two epochs determined visually.

Correlation Lifetime

An objective way to quantify change of features in a pattern is through cross-correlation (CC). The lifetime obtained from CC represent a statistical or mean lifetime of the cells in the window. CC is insensitive to the type of changes undergone by the pattern; whether instrinsic changes or changes due to movement of fine structures (which can lead to change in shape, size or induce distortion): Wang & Zirin (1988) have noted that cells may retain their individuality, even though they may undergo shape changes, beyond the correlation lifetimes. Nonetheless, CC method is preferred for its obvious objectivity and because it can be automated.

One point worth noting is that lifetime derived directly from SG velocity fields tend to be larger and represent the true lifetime (Smithson 1973; Duvall 1980). CN is a "thin" system that does not represent the whole SG, but only its borders. Thus, minor shape changes will lead to considerable fall in CC, leading to an SG lifetime underestimate.

CC is calculated by setting $\Delta = 0$ in Eq. 2.1:-

$$\mathrm{CC}(\tau) = (1/N) \int_A I(t,r) I(t+\tau, r) dA, \tag{5.1}$$

where $I(t,r)$ and $I(t+\tau,r)$ refer to two different images seperated by time interval τ.

The CC method was applied to solar features first by Bahng & Schwarzschild (1961), in order to derive granular lifetimes. Simon & Leighton (1964) and Rogers (1970) have derived $1/e$ lifetimes from exponential fits. In addition

Rogers quotes twice half lifetime to straight line fits to the data (given as the second estimate of Rogers in Table 5.1). Raju, Srikanth & Singh (1998a) have estimated chromospheric network lifetimes similarly, though they derived CC digitally in place of the correlator machine used in analog methods.

5.2 Methodology

Alignment of the image-stack

During any correlation run, at least about 35 hour of data was taken. Part of the alignment was done by de-rotations on the digitizing platform (Section 2.4). Further de-rotation was done using sunspots as reference points and rotating images with respect to a provisional reference frame. The sunspot coordinates were determined by plotting intensity contours around the sunspots and selecting the intensity minimum point. The IRAF software package was used to rotate and/or translate images to bring them into register with a provisional reference image.

A further refinement in the alignment is done as follows using 2D spatial correlation. During CC runs, the window in the reference image is chosen to be slightly smaller than the windows on the "field images". The reference window is then slid across the field windows, and the shift that maximizes correlation is assumed to yield the required translation.

Choice of region

Because of image rotation, a de-rotated image may not have all regions in common with all other images in the image-stack. Windows were not chosen from such regions.

Choice of Reference Image

The reference image was always chosen such that the start of the 4 hour gaps in the time-series did not fall within the first 5 hours.

Size and shape of windows

The arguements for sizes of windows used in AC more or less apply here, too. Windows $198'' \times 198''$ in size were chosen for the correlation runs.

Computing the correlation lifetime

The first step is to cut out a time-sequence of windows from the image stack, once a suitable reference image has been chosen. A given run consisted of running correlation program on this window-sequence, reformatted as a text file.

Computationally, temporal correlation is calculated by setting $\Delta = 0$ in Eq. 2.3:-

$$\mathrm{CC}(\tau) = (1/N)\langle \delta I_t(r) \delta I_{t+\tau}(r) \rangle, \tag{5.2}$$

The normalization factor $1/N$ is given by:-

$$N = \sqrt{\langle \delta^2 I_t(r) \rangle \langle \delta^2 I_{t+\tau}(r) \rangle}$$

Plot of correlation against time lapse is given in Fig 5.1 for a typical quiet window. The gap between 11 hr – 15 hr corresponds to a gap in the data.

The CC in Fig 5.1 is a complicated function of τ (Title 1968). It shows a pattern of overall falling of the correlation with τ. In QS, CC flattens out at $\tau > 40$ hr, assuming near zero value. Correlation falls quickly from 1.0 at $\tau = 0$ to about 0.6 at $\tau = 10$ min. This is due to re-arrangement of smaller structures like dark mottles (Rogers 1970). In K line images, it is due to network and intranetwork bright points (BPs). Thereafter, the data

Fit	type	window 1	window 2
linear	2 × 1/2-life (hr)	34.5	30.6
	1/e-life (hr)	21.8	19.9
exponential	1/e-life (hr)	19.3	17.9

Table 5.2: Lifetimes using different fits

is clustered about a slightly curved line extending upto about $\tau = 35$ hour. Beyond 35 hour, the CC drops to below 0.2, in case of quiet windows.

The solid line in Fig. 5.1 is the exponential fit to the data. The fit has the form:

$$y_{fit} = A \cdot exp\left(\frac{-t}{t_0}\right).$$

where the A and t_0 are determined by the method of least squares linear fit taking the logarithm of correlation. The y-intercept is 0.53, while t_0 is found to be 23.6 hr, which is considered as the mean lifetime of the cells in the window.

The exponential fit models both the initial steep fall and the final flattening of the CC curve. Lifetime is estimated as the time-lapse needed for the function to fall to $1/e$ times its y-intercept. The dashed line in Fig 5.1 is the linear fit with a y-intercept of 0.51, and slope of -0.012. We note that the y-intercept of the exponential fit is higher. Lifetime is calculated as twice half-life, i.e, timelapse for CC to drop to half the y-intercept value; alternatively, as timelapse required to fall to $1/e$ times the y-intercept (Rogers 1970).

From the viewpoint of standard deviation, both fits seem equally suited.

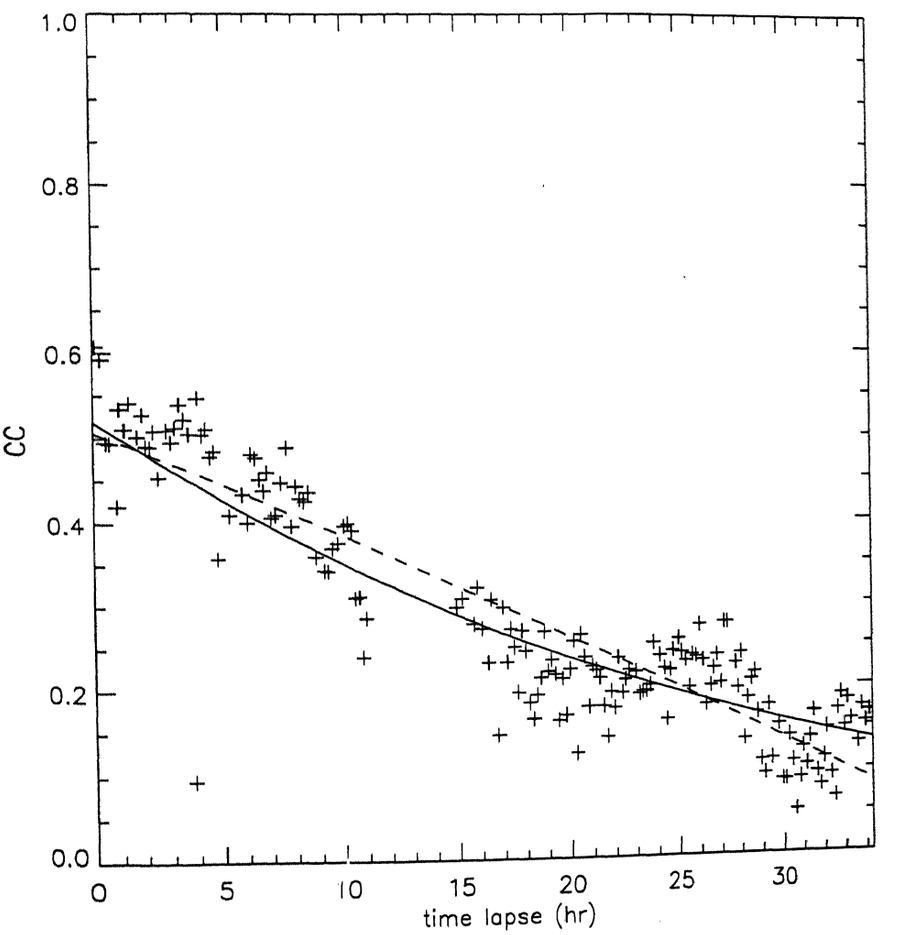

Figure 5.1: Plot of correlation against time lapse. The solid line represents an exponential fit and the dashed line a linear fit.

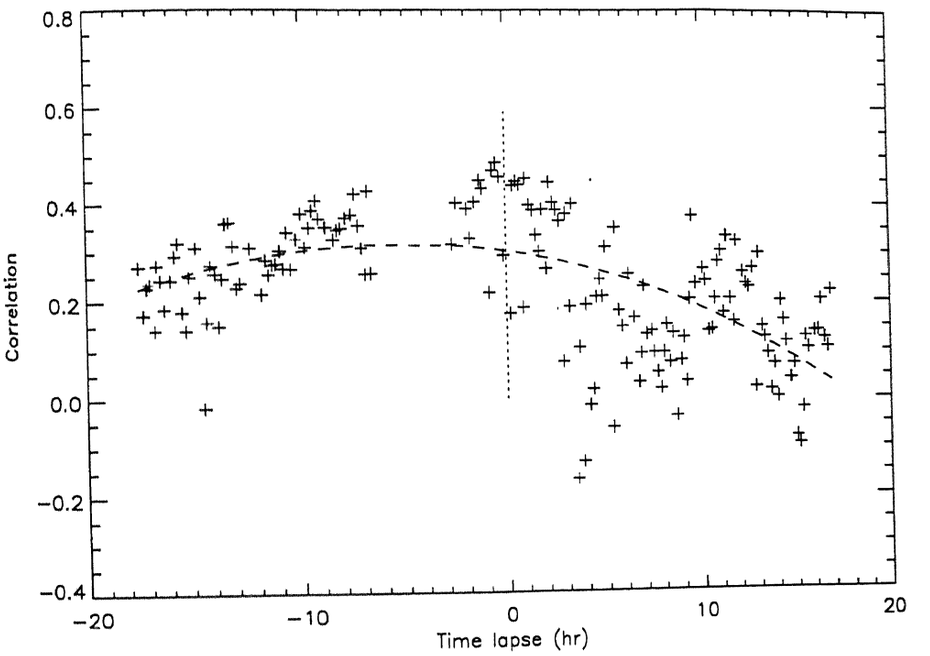

Figure 5.2: Temporal correlation of a $50'' \times 50''$ window with the images compared before and after the reference image. The dashed line gives a quadratic fit to the data. Note the large scatter in positive time which forces a time asymmetry in the correlation. The dotted line in the center represents the reference image for which $ACF = 1$.

For example, in Fig. 5.1, the σ of the exponential fit is 0.065 whilst that of the linear fit is 0.071. The interpretation of these fits depends on the underlying physical processes that drive cell evoltuion. For example, Bahng and Schwarzschild (1961) show that their CC for granules can as well be described by an exponential function as a sum of two exponential functions. Lifetimes returned by the two fits for two windows are given in Table 5.2.

Fig 5.1 shows that the observed CC is quite wiggly (eg., the wiggle between 3 to 4 hour), which might be an artefact. A surprizing feature of the CC are the long lasting undulations about the linear fit. We find that

the undulations dip around τ = 11 hr, 21 hr and 32 hr, and rise at τ = 28 hr and 34 hr. It is remarkable that for example CC(28 hr) > CC(20 hr), inspite of the 8 hr gap. Again, CC(28 hr) is approximately equal to CC(16 hr), inspite of the 12 hr gap.

The strong effect of these undulations can be gauged from Fig 5.2. The time-series of images used in Fig 5.2 is identical to that used in Fig 5.1, except that the reference frame has been shifted to an intermediate epoch of t = 17.5 hr. Since the window contains about as many as 25 CNCs, we expect a symmetric evolution of the window in both directions of time. In fact, the undulations of the latter figure about the linear (or exponential) fit are paralleled in Fig 5.2 by undulations about the second order fit (dashed line). For example, the great dip seen in Fig 5.1 at 20.5 hr, approximately corresponds to the great dip at 3.5 hr in Fig 5.2 must be ascribed to some long-duration event that is unevenly spread in time.

Possible artefacts due to insufficient de-rotation of images was ruled out by noting that for reference windows obtained from the same image, the undulations were not necessarily synchronized. Furthermore, the dependence of the undulations on activity (Section 5.6) suggests that they are intrinsic.

It may be of interest to note that Figs. 4a, 4b, 5a and 5b in Wang (1988a), which study solar magnetic fields, show a similar, though much weaker, trend. The data for that analysis came from the Big Bear Observatory videomagnetograms, not K line filtergrams. Still, given the close connection between K line emissions and the magnetic network, it may be related to our observations.

No.	Parameter	Value
1	Mean cell lifetime	26.4 hr
2	Most probable lifetime	25.0 hr
3	Maximum cell lifetime	37.6 hr
4	Minimum cell lifetime	20.6 hr

Table 5.3: Some correlation lifetime parameters of K line CNCs

5.3 Lifetime and decay of cells

5.3.1 Cell lifetime distribution

The 82 windows used for deriving length-scales and wall-sizes, mentioned in the Section 4.3, were used also to determine lifetime. Their histogram is given in Fig. 5.3.

Some of the intermediate bins in Fig. 5.3 are empty, probably due to insufficient sampling. The distribution varies between about 20 hr and 38 hr, with a most probable lifetime of 25 hr, and a mean of 26.4 hr. The cell-lifetime estimate is comparable with values cited by Hart (1956) and Leighton, Noyes and Simon (1962) and other values cited in the Table 5.1 of this chapter. Some results of the analysis are summarized in Table 5.3.

5.3.2 Cell lifetime dependence on activity

Cells fall into three types: active, semi-active and quiet cells. Active region cells are those found near the plages, and are magnetically dominated. They show some network structure, though it is not as pronounced as in the quiet

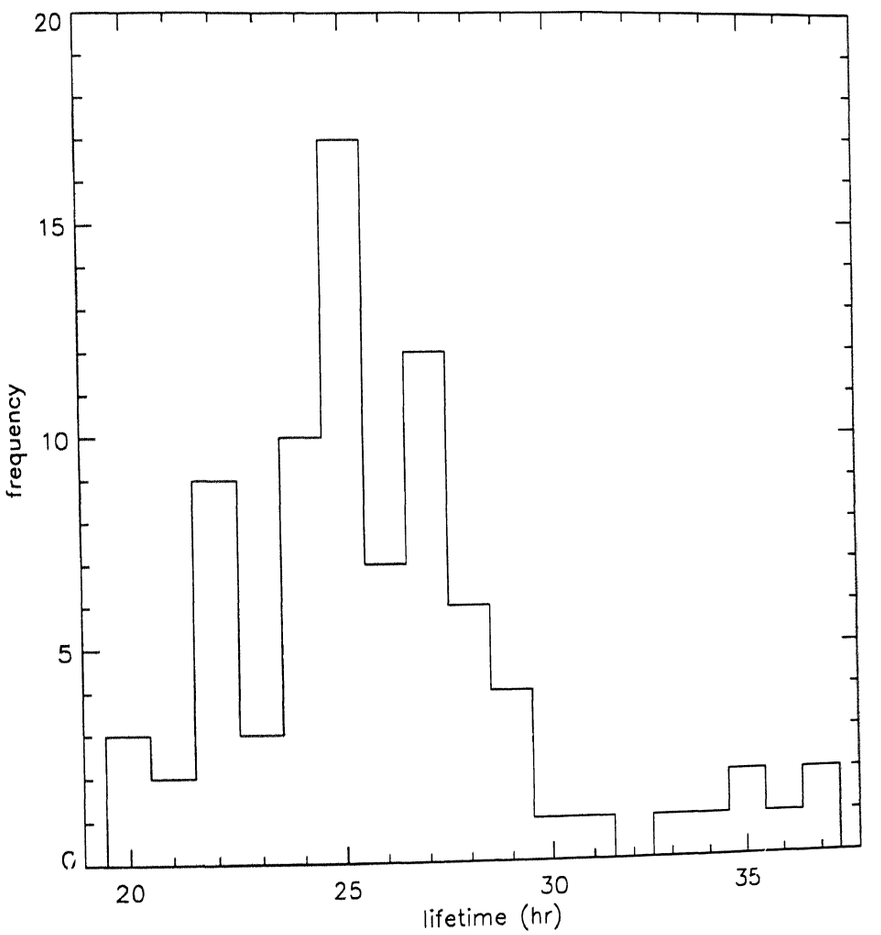

Figure 5.3: Histogram of the lifetimes of quiet cells.

regions. Quiet or quiescent cells are found far from regions of activity. Semi-active cells are found in the intermediate regions and show enhanced wall emission. In Fig 5.4, we present the CC function for the three levels of activity. The first two, marked 'q', are from quiet regions. Data-points from semi-active region are presented in the plot labelled 's', and those from active region 'a'. In Table 5.4, lifetime estimates for 10 windows of the different activity levels are given.

These results corroborate those of Wang (1988b). This is similar to the behaviour of granules which live longer near active regions (Title et al. 1989).

We note that the first two plots, representing QS, show more fluctuation and more broadening of the CC curve. Both these effects are minimized for the semi-active and active windows. This was one reason to suspect the undulations are intrinsic to the chromosphere, rather than artefacts of observation or measurement.

The difference in correlation lifetimes can be understood in terms of the interaction between magnetic fields and convection. Strong magnetic fields tend to inhibit convection (Biermann 1946) as evidenced by large outward moving flux close to sunspots (Wang 1988b). Another cause could be the phenomenon of magnetic confinement in regions with a greater activity level (Zwaan 1978). Confinement implies slower diffusion rates of magnetic and cell features which results in longer lifetimes, as discussed in the next subsection.

5.3.3 Decay of network cells

The fall in CC can be attributed to one or both of:

1. intrinsic changes in the network (appearance and disappearence of features; change in relative intensity and/or shape of features).

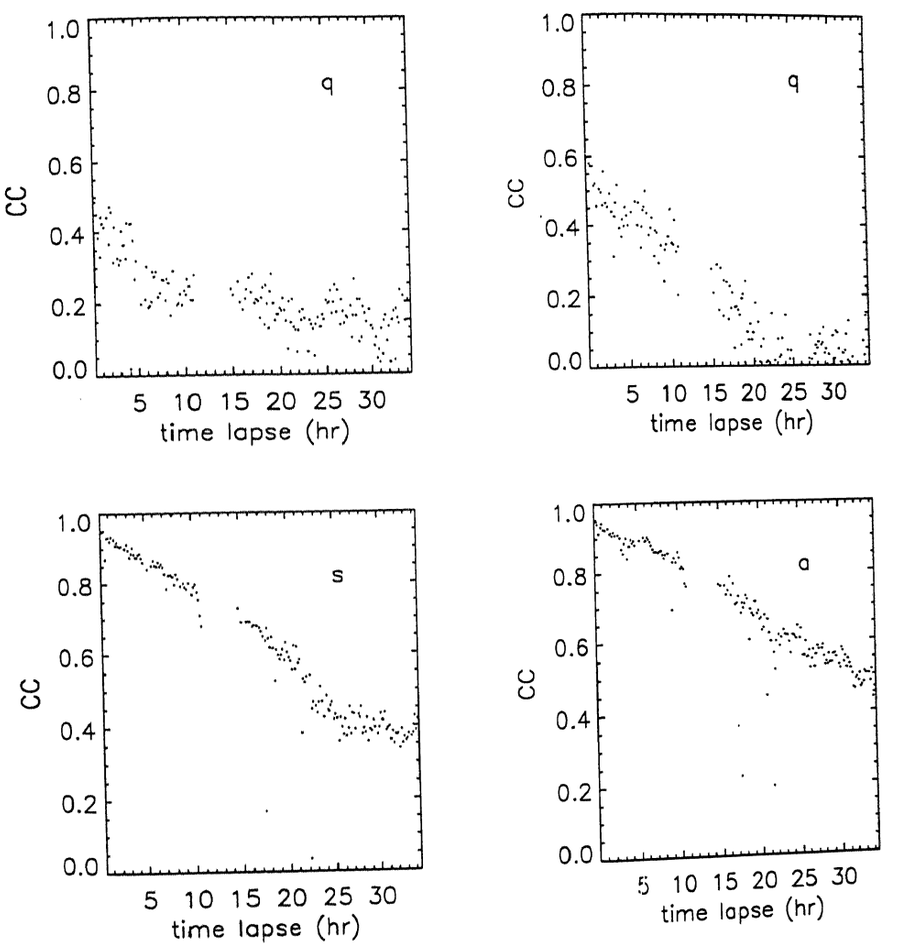

Figure 5.4: Temporal correltion for regions of varying activity level: the first two plots marked 'q' are from quiet windows; the third, marked 's' is from a semi-active window; the last, marked 'a' is from an active window. CC falls slowest in active regions and fastest in quiet regions. Thus, derived lifetimes are smallest in quiet windows.

No.	Region	lifetme (hr)
1	Quiet	21.6
2		24.4
3		24.6
4		27.7
5		28.1
6	Semi-active	39.9
7		44.6
8	Active	54.2
9		59.1
10		61.3

Table 5.4: Correlation lifetime estimates for CNCs from 10 windows obtained from different activity levels.

No	Region	AC(Δ) (km) = 0.75	CC(τ) (hr) = 0.75	Speed km/s
1	Quiet	6 635	12.1	0.15
2	Semi-active	9 300	18.1	0.14
3	Active	12 630	20.	0.19

Table 5.5: Time lapse for CC = 0.75 and spatial lag for AC = 0.75 for different activity levels, used to estimate the speed of motion of K line fluxtubes.

2. Movement of flux tubes.

At magnetic level, these changes are accompanied by the appearence, disappearence, splitting and merging of flux (Livi, Martin & Wang 1985; Martin & Wang 1985; Zirin 1987).

If the fall in CC is wholly due to intrinsic change, then as CC = 0.75 about quarter of the features have changed. If the fall is wholly due to movement of magnetic flux tubes, then an upper limit on the speed of the movement of the structures can be calculated using AC and CC as follows. We consider two similar characteristic features moving past each other. AC gives correlation as a function of their relative position. If this motion alone causes fall in CC, then the same value of correlation can be used to read off CC the time taken by the feature to move through the distance (Wang 1988a). The results for different levels of activity are summarized in Table 5.5. The choice of 0.75 is to enable a smooth interpolation of CC (section 4.4).

It is interesting to note that the above values are comparable to the speeds of fluxtubes observed in Dopplergrams in regions of different activity

in the Sun (Wang 1988b). The speed as deduced from the K line image is the same in both quiet and semi-active (enhanced network) region, while that for very active regions (close to spot-group) is greater. What is surprising is that in spite of their different magnetic structure, velocity fields in the quiet and semi-active regions can be similar. A reason for this could be that the fields are a resultant of convective motions and magnetic inhibition of motion. Both these factors are stronger in more active regions, leading to speeds similar to quiet regions.

Mosher (1978) has used CC and AC data to construct a model of diffusion of solar magnetic fields. Individual flux tubes are estimated to have diameter s given by:

$$s = (\mathrm{FWHM})_{AC}/1.6 \tag{5.3}$$

In the K line images, we assume that the flux tubes correspond to fine structure such as bright points and flocculi. In his model:-

$$\mathrm{CC}(t) = 1 - \left(\frac{\sqrt{\pi D t}}{1.7s}\right) \mathrm{erf}\left(\frac{1.7s}{\sqrt{\pi D t}}\right) \tag{5.4}$$

where D is the diffusion constant and erf is error function. Fitting this to data in K line (Simon 1964) and in Hα line (Rogers 1970), he derived, respectively, 200 km^2 s^{-1} and 400 km^2 s^{-1}. Applying the same technique to Dopplergrams, Wang (1988a) obtained a value of about 150 km^2 s^{-1}.

The solid line in Fig 5.5 gives a best fit to the data with a functional form given by Eq. (5.4). It corresponds to a diffusion rate of 125 km^2 s^{-1}; the lower dashed line lies below all the data, and hence gives an upper limit to diffusion constant and corresponds to 185 km^2 s^{-1}. In Fig 5.6, CC(τ) for semi-active region is given to determine diffusion rate. The solid line gives a best fit to the data with a functional form given by Eq. (5.4). It corresponds to a diffusion rate of 70 km^2 s^{-1}; the lower dashed line lies below all the data, and hence gives an upper limit to diffusion constant and corresponds to 100 km^2 s^{-1}.

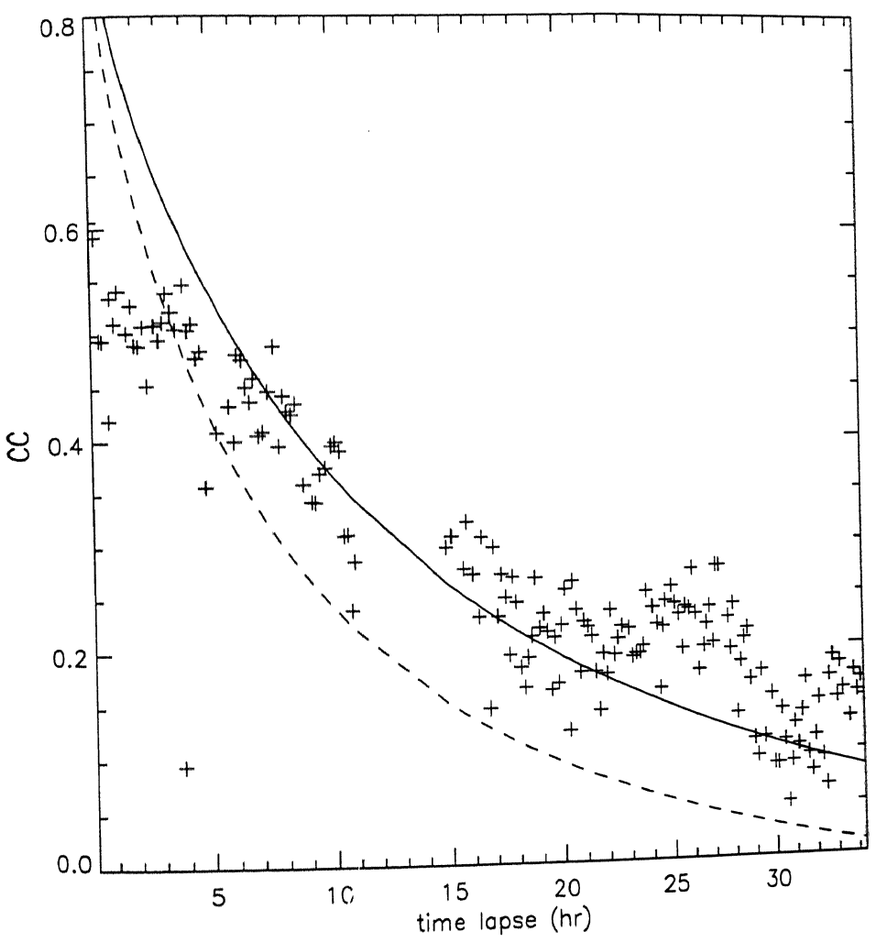

Figure 5.5: Fitting functions of form given by Eq. (5.4) to derive the diffusion constant for QS chromospheric features. The solid line represents the best fit to the data. The dashed line lies beyond most data-points, and provides an upper limit to diffusion constant.

region	fit type	Diffusion rate
QS	best-fit	125 $km^2\ s^{-1}$
	maximum	185 $km^2\ s^{-1}$
semi-active	best-fit	70 $km^2\ s^{-1}$
	maximum	100 $km^2\ s^{-1}$

Table 5.6: Diffusion rate in QS and semi-active regions. The longer lifetimes in the latter regions are due to slower diffusion rates.

Fig 5.6 overplots the errorfunction on the semi-active data. As before, the central solid line is the best-fit line corresponding to 55 $km^2\ s^{-1}$; the lower dashed line gives an upper limit to diffusion constant and corresponds to 80 $km^2\ s^{-2}$. The diffusion rate data is given in Table 5.6. Diffusion rate is seen to be lower in semi-active region than in QS, in conformance with the observed longer lifetimes in semi-active regions.

5.4 Dependence of lifetime on length-scales

Singh et al. (1994) have shown that in both active and quiet regions, larger cells appear to have longer lifetimes. An analogous situation exists for granules (Title et al. 1986). According to Leighton (1964), cells evolve with the diffusion of magnetic flux, hence larger cells are expected to live longer.

Simultaneous autocorrelation length-scale and correlation lifetime measurement were made in a collection of 82 windows (Section 4.3.1). Each

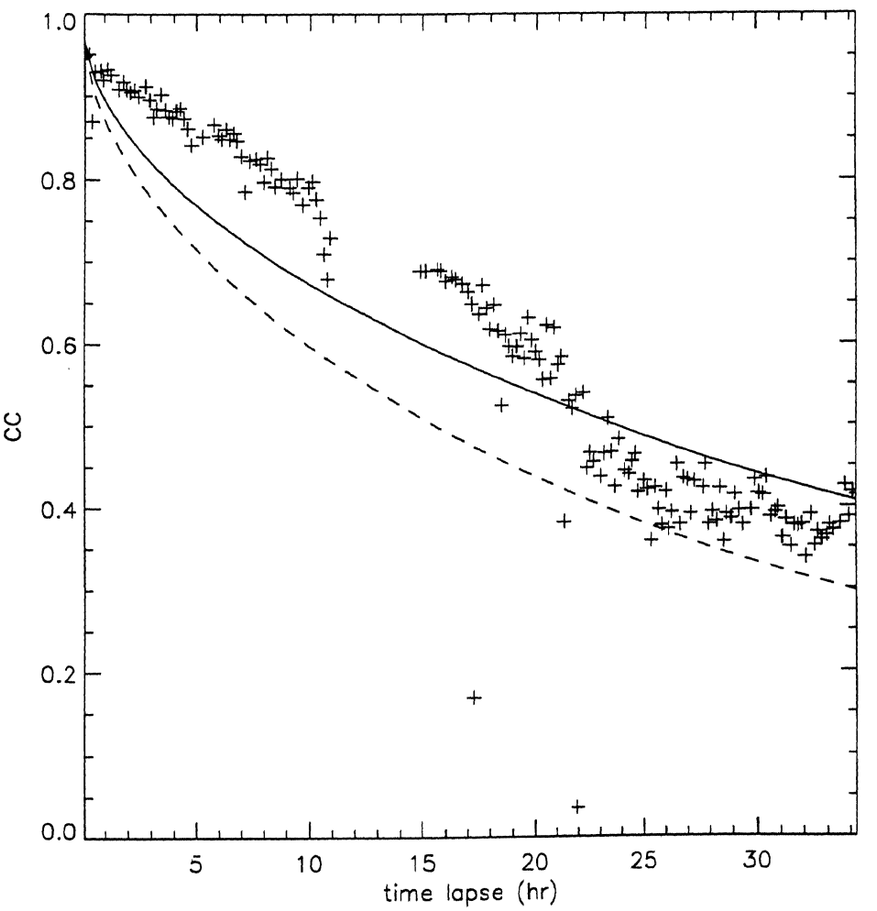

Figure 5.6: Fitting functions of form given by Eq. (5.4) to derive the diffusion constant for semi-active chromospheric features. The solid line represents the best fit to the data. The dashed line lies beyond most data-points, and provides an upper limit to diffusion constant.

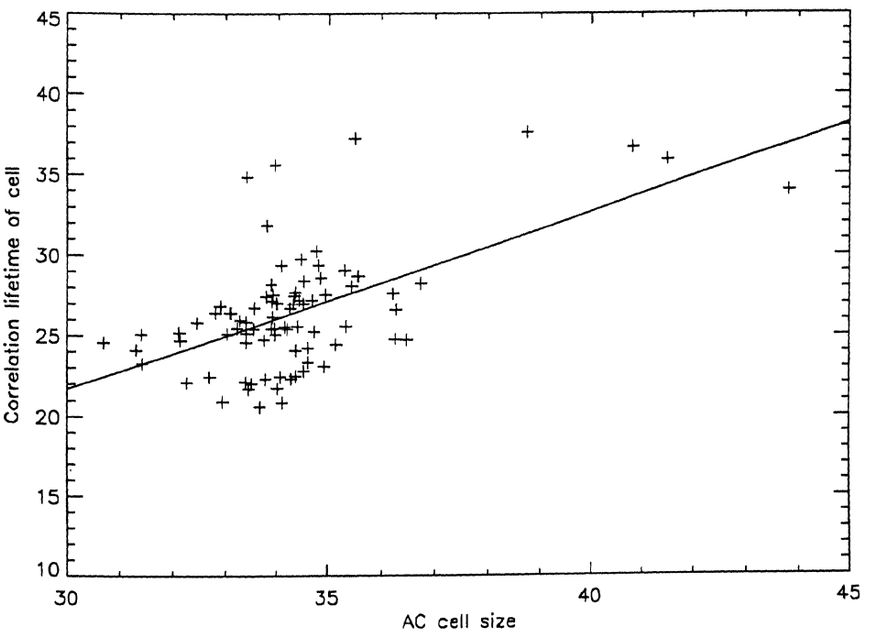

Figure 5.7: Plot of cell lifetimes against sizes. The sizes were derived from the SM of the AC and lifetimes as $1/e$ lifetimes from a linear fit to CC(τ). The solid line shows a linear least squares fit.

window-sequence extended over 35 hr, and to make the two parameters compatible, length-scales were derived as averages of the SM measurements over the whole window sequence. A plot of cell lifetimes against sizes is given in Fig. 5.7.

The correlation between the lifetimes and cell-sizes was 0.57, implying a significant inter-dependence of lifetime and cell-size.

From Fig 5.7, it would appear natural to fit lifetime against length-scale. Yet it turns out that a life-vs-cell-area relation also fits the data well (Singh et al. 1994). The above scatter plot is an insufficient guide to determine the functional form of the relation between length-scale and

No	Functional form of fit	Std. dev.
1	$y = a_1 x + a_0$	0.3357
2	$y = a_2 x^2 + a_0$	0.3353
3	$y = a_2 x^2 + a_1 x + a_0$	0.3353
4	$y = a_3 x^3 + a_2 x^2 + a_1 x + a_0$	0.328
5	$y = a_1 x^{1.36}$	0.338

Table 5.7: Various functional forms of fit to the life-size scatter plot Fig 5.7 and resulting standard deviations, where x and y denote length-scale and lifetime.

lifetime. Because of the short range of available data and the somewhat large scatter, various functional forms turned out to give equally good fits. In Table 5.7, we present the standard deviations for a variety of functional forms. Here x is the length-scale and y the lifetime.

The last function was obtained as the best fit power-law form by taking logarithms of size and lifetime. Clearly, none of the functional forms is significantly preferred over any other. To determine the form of this function, we adopt a statistical approach.

The distribution functions (probability density function) of lifetime and sizes must reflect their inter-relation. In the following account we describe a way in which, by comparing the statistical properties of size and lifetime, we can try to estimate the functional relation between the two parameters. Apart from mean and standard deviation, two statistical parameters that are frequently used are skewness (α_3) and kurtosis (α_4) (Hoel 1971). To begin with we assume that the distributions for lifetime and scales are fairly well

represented by their skewness and kurtosis, and that these two parameters are intrinsic to the distribution. For a distribution function $f(x)$, skewness is defined as the third moment of location about mean expressed as a dimensionless quantity.

$$\alpha_3 = \frac{1}{\sigma^3}\int_{-\infty}^{\infty}(x-\mu)^3 f(x)dx. \tag{5.5}$$

Skewness gives a measure of asymmetry about mean in the random variable x. Kurtosis is defined as the fourth moment of location about mean expressed as a dimensionless quantity.

$$\alpha_4 = \frac{1}{\sigma^4}\int_{-\infty}^{\infty}(x-\mu)^4 f(x)dx. \tag{5.6}$$

Kurtosis is a measure of peakedness in the random variable x. The advantage of using these statistical properties to estimate the form of the relation is that we are no longer constrained to generate both lifetime *and* size data, nor to use the same number of data-points for size and lifetime. Reported distributions in the literature may be used, for example, provided only that each data-set has been generated homogeneously.

We consider the distribution function $f(x)$ of a random variable X. Being normalized, f(x) satisfies:

$$\int_{-\infty}^{\infty} f(x)dx = 1 \tag{5.7}$$

Let $f(x)$ transform to $g(y)$ for a change of variables $Y = \phi(X)$ can be determined as follows. Let $X = \psi(Y)$. By definition:

$$\int_{x_1}^{x_2} f(x)dx = \int_{\phi(x_1)}^{\phi(x_2)} g(y)dy$$

Since the distribution function must always be positive definite, this implies:-

$$g(y)|dy| = f(x)|dx|$$

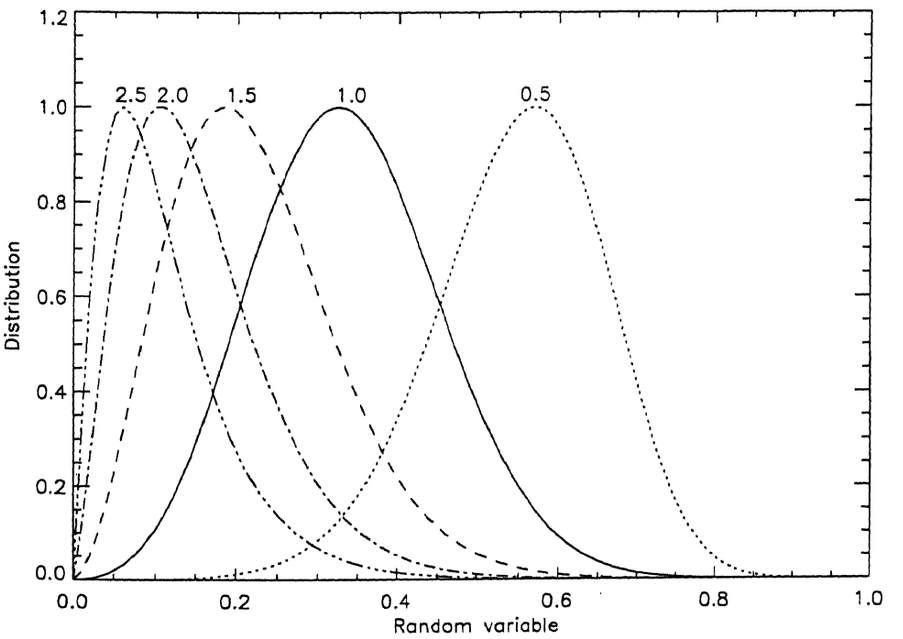

Figure 5.8: Resultant distributions under power-law transformations of a random variable obeying Gaussian distribution. Each resulting distribution has been labelled by the power of the parameter under which it was produced. We note the increase of asymmetry and peakedness of the distribution as power increases. For powers < 1, skewness becomes increasingly negative and peakedness increases.

so that:-

$$g(y) = f[\psi(y)]|\psi'(y)| \tag{5.8}$$

where the prime denotes derivative. Alternatively:

$$\begin{aligned} f(x)|dx| &= g(y)|dy| \\ &= g(y)|\phi'(x)dx| \end{aligned} \tag{5.9}$$

wherefrom:

$$g(y) = \frac{f(x)}{|\phi'(x)|}, \tag{5.10}$$

$$x = \psi(y)$$

We consider the length-scale L to be a random variable, and lifetime T as a random variable derived as a function $T = \phi(L)$. We denote by $f(l)$ and $g(t)$ the distribution functions for scales and lifetimes, respectively. For simplicity, we wish to confine $\phi(L)$ to a polynomial relation of the form:

$$T = aL^n + b \tag{5.11}$$

According to Eq. (5.10), this implies:

$$\begin{aligned} g(t) &\sim \frac{f(l)}{l^{n-1}} \\ l &= \phi(t) \end{aligned} \tag{5.12}$$

Here the constants are insignificant since the $g(t)$ has to be normalized. It is evident from Eq. (5.10) that the distribution density function does not change under the addition of some constant to the random variable. Likewise, under a multiplication of a constant factor, the distribution changes only upto the normalization constant, and not in shape.

In Fig 5.8 we plot the resultant disributions for various power-law transformations of a random variable with Gaussian distribution. The labels on each curve correspond to value of the power n, namely $n = 0.5, 1, 1.5, 2, 2.5$.

Clearly the distribution becomes more peaked and skewed as we transform to a higher power. This can be understood in terms of Eq. (5.12). Higher powers in the denominator will suppress $g(t)$ more at higher values of l, thereby tending to flatten the later part of the distribution, while at small values of l it becomes steeper.

In Fig 5.3, the mean being larger than the most probable lifetime reflects a skewness, or asymmetry in the distribution. The skewness is by definition positive since the distribution is skewed towards *larger* lifetimes. Using Eqs. (5.5) and (5.6), the skewness and the kurtosis of the lifetime

Field	Gaussian	Length-scale (km) distribution	Lifetime (hr) distribution
Skewness	0	0.65	1.13
Kurtosis	3	3.34	4.488

Table 5.8: Some statistics of the length-scale (Fig 5.9) and lifetime distribution (Fig 5.3) for the Ca II K network cells. The corresponding values of a Gaussian distribution are given for comparison.

histogram is found to be 1.13 and 4.488, repsectively. This indicates that the cell lifetimes are more crowded around the mean value than in the case of a Gaussian distribution ($\alpha_4 = 3.0$). For size distributions, we have used the AC scale distribution from Simon & Leighton (1964). The reason for doing it is twofold: (a) our datapoints are fewer in number by almost half; (b) our length-scales were obtained as time-averages over a cell lifetime span. This was done to make the sizes and lifetimes compatible for the scatterplot in Fig 5.7. However, sizes were found to show considerable variation in this time, and it is unlikely that the averaged sizes are appropriate for studying their distribution. However, line fits in scatterplots such as Fig 5.7 will not be as sensitive to the averaging as distribution functions will be. The Table 5.8 presents skewness and kurtosis from Figs 5.3 and 5.9.

The Table 5.8 shows that the cell lifetimes are distributed in a more asymmetric and lumped fashion in comparison with cell sizes. We suggest that the above values are characteristic of the length-scales and lifetimes of quiet Sun supergranules. We would like to determine n as the power-index in Eq. (5.11) that will transform size distribution to one that will be similar to that of lifetime.

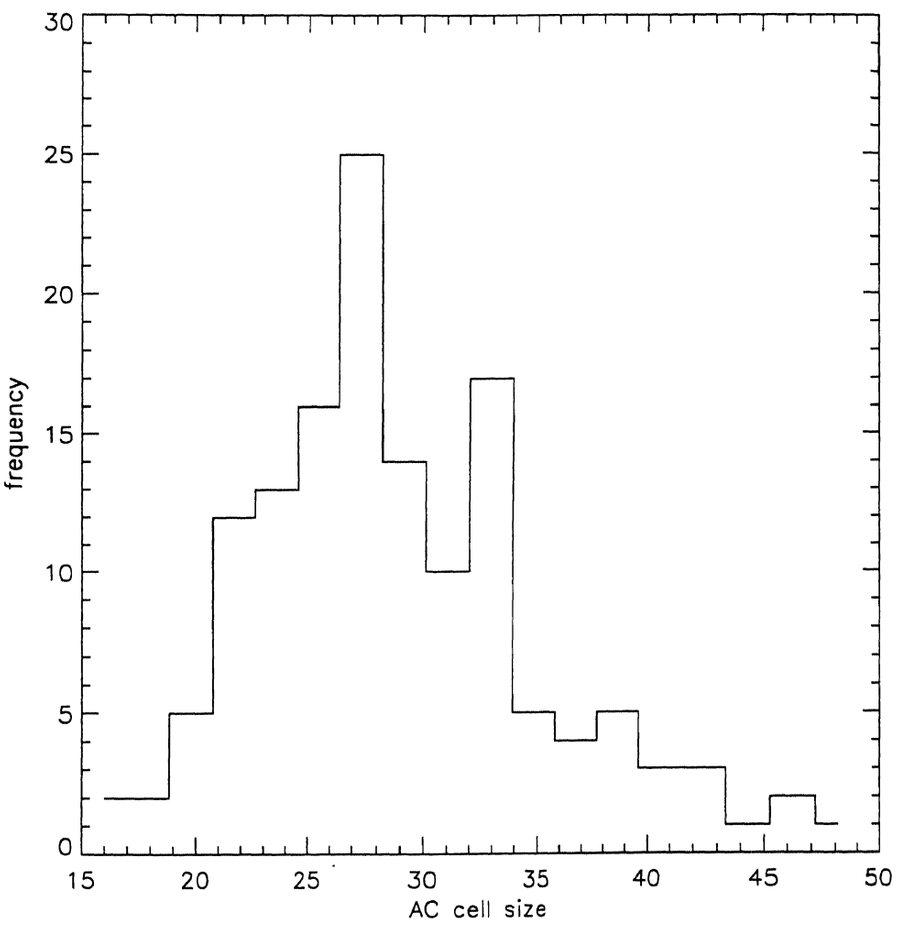

Figure 5.9: Histogram of lengthscales of supergranules. Adapted from Simon & Leighton (1964).

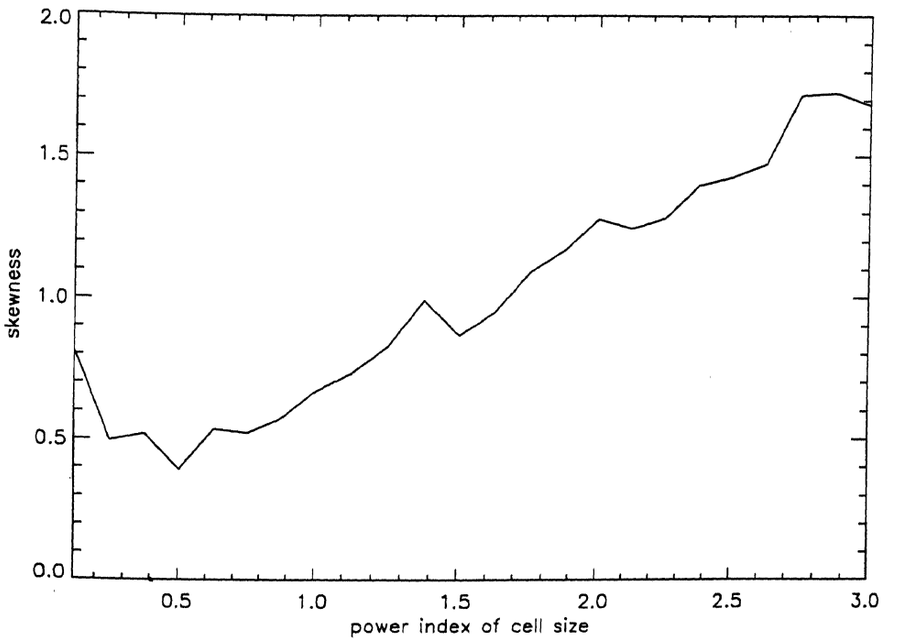

Figure 5.10: Plot of skewness of distribution for various powers of scale. The skewness of the lifetime is 1.13

In Fig 5.10 we plot the skewness of the resultant distributions for various powers of length-scale. The result is given in tabular form in Table 5.9. The powers vary from 0.125 to 2.5 in intervals of 0.125. We find that the power n of scales that produces the required skewness of distribution of 1.13 falls in the range 1.75–1.875.

To confirm this result, we check the value of n corresponding to a kurtosis match. In Fig 5.11 we plot the kurtosis of the resultant distributions for various powers of length-scale. We find that the power n of scales that produces the required kurtosis of distribution of 4.488 falls in the range 2.25–2.375.

It is interesting to note that the ridges in plots of Figs 5.10 and 5.11

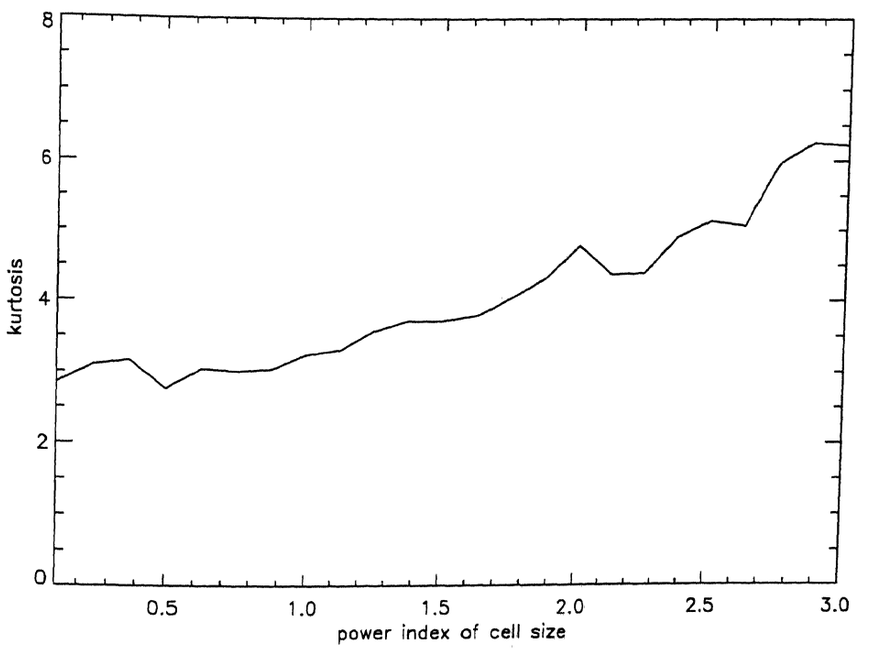

Figure 5.11: Plot of kurtosis of distribution for various powers of scale. The kurtosis of the lifetime is 4.488

appear to correspond to each other. The discrepancy in n as derived from skewness and kurtosis is probably due to the limited sample from which the distributional characteristics have been inferred.

We conclude that the value of n in Eq. (5.11) satisfies $1.75 \leq n \leq 2.25$. This agrees with the approach of Singh et al. (1994), who obtained a linear relation between area and lifetime. To compare our results with theirs, we have provisionally adopted $n = 2.0$. The least-squares fit could be described by the equation $T = 10.33 + 1.50\Sigma$, where $\Sigma = L^2$. Here lifetime T is given in hours and Σ in 10^8 km^2. The corresponding fit in Singh et al. (1994) has a slope $d\Sigma/dT = 3.4$, a value over twice the value of 1.50 obtained by us.

To resolve the discrepancy, we noted:

1. autocorrelation sizes are larger than visual examination sizes by over 40% (Singh & Bappu 1982; Hagenaar, Schrijver & Title 1997). In Section 4.2, we attributed this to intercellular spaces. In Singh et al. (1994) the mean scale obtained by visual inspection is about 24 500 km, whereas that in ours is about 34 500 km. This gives an inconsistency ratio of about 0.71. We factor our scales by this value.

2. We have taken area $= L^2$. Assuming circular instead of square cells decreases area by the factor $4/\pi$.

3. Their method of deriving lifetimes was different. Ours is obtained cross-correlationally, whilst theirs was obtained by inspection. In order to estimate the disparity, we note that the mode of their distribution is 22 hr whilst ours is 25 hr. To make our lifetimes estimates comparable, we factor our lifetimes by $22/25 = 0.88$.

The resulting scatterplot into which these compensations have been incorporated is given in Fig 5.12. A least squares fit to this plot is given by:-

$$T = 7.78 + 3.34\Sigma, \tag{5.13}$$

Power index	skewness	kurtosis
1.00000	0.668841	3.24498
1.12500	0.734167	3.31156
1.25000	0.830133	3.57794
1.37500	0.993915	3.71959
1.50000	0.869230	3.72335
1.62500	0.952674	3.79776
1.75000	1.09465	4.04655
1.87500	1.17268	4.32198
2.00000	1.28014	4.78859
2.12500	1.24752	4.37791
2.25000	1.28457	4.39340
2.37500	1.39970	4.90784
2.50000	1.42862	5.13874

Table 5.9: Skewness and kurtosis of the resulting distribution for various powers of cell length-scale with the distribution given in Fig 5.9

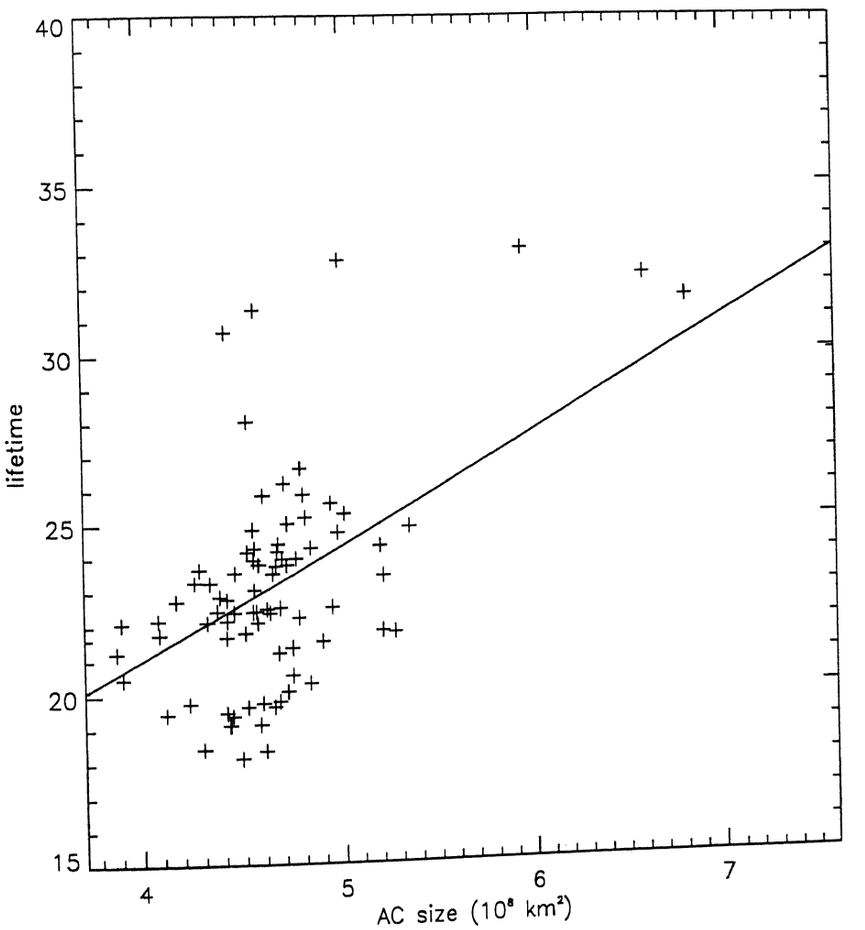

Figure 5.12: The scatterplot Fig 5.7 replotted with areas instead of scales in ordinate axis and after compensations have been made to related it to Singh et al. (1994).

where now Σ is the compensated area. This fit is very close to the one derived by Singh et al. We are thus able to corraborate their result that $d\Sigma/dT \approx 3.3$. From Eq. 5.13, we estimate the diffusion constant for SGs to be:

$$\begin{aligned} D_{SG} &= \frac{d\Sigma}{dT} \\ &\approx 8417 \ \mathrm{km^2 s^{-1}} \end{aligned} \tag{5.14}$$

An order of estimate of the diffusion constant can be made by assuming that the cell decays completely during its lifetime by random walk of its fine structures. For typical cell of size 30 000 km and lifetime 25 hr, we find this yields a $D_{SG} = 10^4$ km^2 s^{-1}, which is comparable to the estimate in Eq. 5.14.

To compare this with the diffusion constant D for fine structures derived in Section 5.5.2, we assume that a cell of size 30 000 km is filled with random walking fine structures of size s as given by Eq. 5.3. From Fig 4.2, we find $s = 3800$ km. Assuming a filling factor of 1, we find that about 62 such structures are packed into the cell. The total diffusion taking into consideration all these structures is then $D \times 62 = 7750$ km^2 s^{-1}. Conversely, using, D_{SG} as given by Eq. (5.14), we can estimate D to be about 135 km^2 s^{-1}, which is smaller than the upper limit of 185 km^2 s^{-1} estimated in Fig 5.5. Thus, our analysis supports the picture of a cell that evolves by diffusion caused by the motion of fluxtubes. The complete evolution can be modelled by considering also the intrinsic changes of fine structures with the cell.

Chapter 6

A tessellation technique applied to quiet chromosphere

6.1 Introduction

In this chapter we intend to study some morphological properties of the quiet chromosphere by tessellating it into intensity tiles. The algorithm used to tile it involves a minimization and clustering procedure which are described below. The technique was first applied to Ca II K images by Hagenaar, Schrijver and Title (1997) who obtained some interesting results. They have essentially identified the tiles with actual CNCs and SGs. We wish to investigate the appropriateness of this identification,

6.2 Optimization of functions

The aim of any optimization algorithm is to extremize (minimize or maximize) a function f. Passing from maximization to minimization is trivial. In the present context, we are in specific concerned with minimizing the 2-dimensional scalar function of intensity $I(x, y)$. The minimum can be global– that is, a true minimum of the function over the entire region in which it is

defined; or it can be local– where it is the lowest value of f in a finite local neighborhood excluding the boundary of that neighborhood.

In our case we have to find the local minima corresponding to the minimum intensity points inside CNCs. One problem here is to distinguish the desired minima from other local minima at smaller scales. The choice of minimization algorithm depends on the problem at hand (Press et al. 1979).

Many methods require a routine/function of line minimization, which returns the minimum along a direction. The line minimization algorithm can be stated as follows: given input vectors of position $\mathbf{x}_0$ and of direction $\mathbf{n}$, find the scalar λ such that it minimizes $f(\mathbf{x}_0 + \lambda\mathbf{n})$. Replace $\mathbf{x}_0$ by $\mathbf{x}_0 + \lambda\mathbf{n}$.

Minimization methods may be classed into those that require line minimization and those that don't. Steepest descent method, which we have adopted, does not require line minimization. Although methods that use line-minimization methods converge rapidly for a minimum located in quadratic valley, they may not be the best choice in a window which contains many desired local minima. Hence, we have preferred the Steepest Descent method (Hagenaar, Schrijver & Title 1997).

The algorithm used in steepest descent can be written as follows: starting from $f(\mathbf{x}_i)$ minimize $f(\mathbf{x}_{i+1})$ by computing the local gradient ∇f. Replace $f(\mathbf{x}_i)$ by $f(\mathbf{x}_{i+1})$.

6.3 Tessellation

Tessellation is the procedure for tiling a surface (in general, an arbitrary space) in a compact fashion. By "compact", it is meant that the tiles completely fill up the surface (or space) with no intervening gaps and no overlaps between tiles. Common examples of tessellations include bricks in a wall, or square, triangles or hexagons patterned on a surface (Fig 6.1). The tessellations shown Fig 6.1 are regular and involve only a single type of tile. In general, a combination of tiles could be chosen.

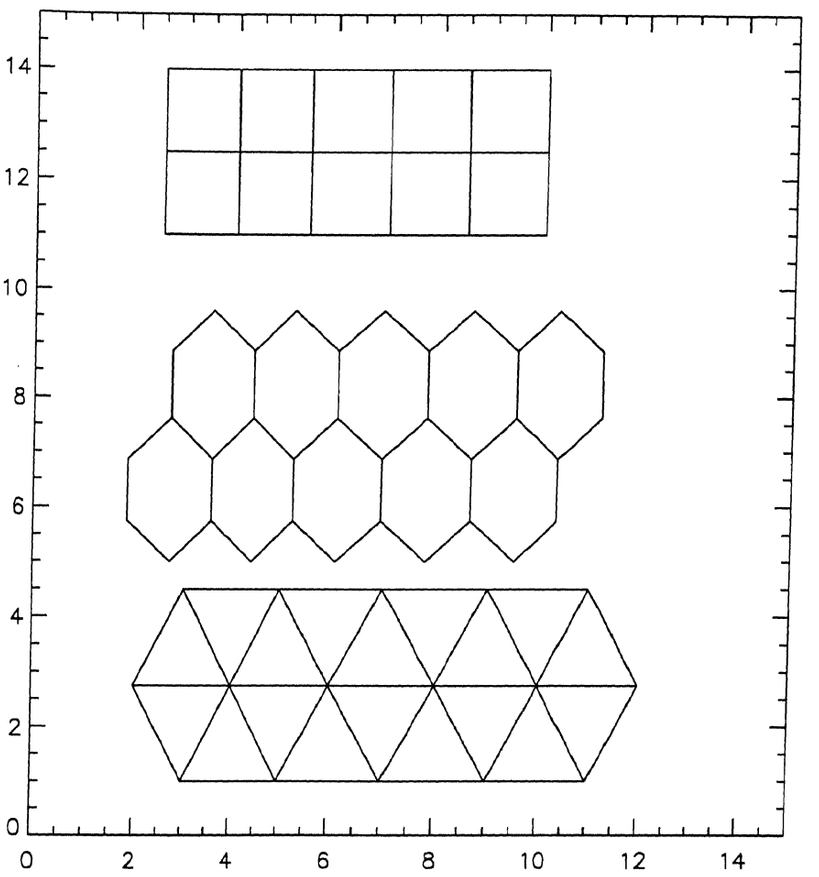

Figure 6.1: Tessallations of squares, hexagons and triangles.

We note that an equilateral triangle, a square and a hexagon have, respectively 60°, 90° and 120°, as their interior angles. Since these numbers are exact divisors of 360°, each of these shapes can be joined at a vertex compactly and hence tessellate in the Euclidean surface.

Tessellations find both pure mathematical and more practical use. Mathematically, they can be used to explore symmetries in rotation, translation, and reflection, and also for interpolation of data points scattered on a plane.

A case of non-regular tiles is Voronoi tessellation. The tiles in this case are polygons which surround data points. The local property of the tiles is that each point within a tile is closer to the data point it encloses than to any other data point. A consequence of this is that the line joining any two data points will intersect the intervening tile-boundary perpendicularly. The data points can act like 'seeds' to generate Voronoi tessellation. Hagenaar, Schrijver & Title (1997) find that the pattern of tiles obtained by tessellating the chromosphere by Steepest Descent method can be modelled as Voronoi tessellation.

6.4 Methodology

We describe a method which combines a minimum finding algorithm with a clustering algorithm.

6.4.1 Minimization

By way of anology we can consider the image as an intensity landscape. The walls of the cells are like hill ranges, and the cell interiors like valleys. One places tracer balls all over this landscape, and allows them to freefall, as it were. At each instant the direction of the balls (assumed to have no inertia) is determined by the steepness of the local surface gradient.

8	8	8	8	8	8	8	8	8	8
8	5	5	5	5	5	5	5	8	8
8	5	4	4	4	4	5	8	7	8
8	5	4	3	4	5	8	7	7	8
8	5	4	4	5	8	7	5	7	8
8	5	4	5	8	7	5	5	7	8
8	5	5	8	7	5	4	5	7	8
8	5	8	7	5	5	5	5	7	8
8	8	7	7	7	7	7	7	7	8
8	8	8	8	8	8	8	8	8	8

Table 6.1: A table representing part of an image with two cells, seperated along the diagonal. The cell maxima lie along the walls while the minimum lies in the interior.

Similarly, the program searches for the minimum intensity point around a given pixel and shifts to that point. The minimum search is repeated until there are no points of lesser intensity around the resultant point. This procedure is done for every pixel in the image.

In Table 6.1, a matrix of abitrary intensity points is given, which can be considered as part of an image. We note that the table contains a pattern of high intensity values (= 8) that delineate two cells by dividing them diagonally. Each cell has smaller values towards its approximate center: the top-left cell with a minimum value of 3 and the bottom-right cell with one of value 4. The minimization program starts at each point of the matrix, and keeps moving in the direction of the lowest valued neighbor until it reaches a minimum. For example, if one starts at the top left corner value of 8, the program goes through $8 \rightarrow 5 \rightarrow 4 \rightarrow 3$ to 3. The coordinate-position of the point with intensity value 3 is noted: (4,4). There is another minimum to be found at (7,7).

At this step the topology of the minimum is ignored. The minimum search ends even if the lowest intensity point around a minimum is of same

0	0	0	0	0	0	0	0	0	0
0	0	0	0	0	0	0	0	0	1
0	0	0	0	0	0	0	0	1	1
0	0	0	0	0	0	0	1	1	1
0	0	0	0	0	0	1	1	1	1
0	0	0	0	0	1	1	1	1	1
0	0	0	0	1	1	1	1	1	1
0	0	0	1	1	1	1	1	1	1
0	0	1	1	1	1	1	1	1	1
0	1	1	1	1	1	1	1	1	1

Table 6.2: The image that results after tiling the image given in Table 6.1

intensity as itself. Thus a broad minimum is treated as a disconnected minimum with as many apparent minima as it has pixels. The connecting of the minima-pixels into a single minimum is done at the next step.

6.4.2 Tiling

In the above analogy of balls rolling on a land-scape, the original positions of all balls converging to a single minimum are classed together as belonging to a single tile. The convergence point may be thought of as a tile "nucleus". Each such tile acts like a basin in the intensity landscape of the chromosphere, consisting of a minimum in the interior and a boundary or wall surrounding it.

The existence of two disconnected minima in Table 6.1, at the coordinates (4,4) and (7,7), implies the existence of two tiles. Each new minimum found is numbered starting from 0 upwards. Each tile is labelled according to its nucleus. The result of applying the tiling algorithm to Table 6.1 is the the matrix in Table 6.2.

By definition this method is surface filling with non-overlapping tiles,

Gaussian FWHM (″)	Mean (Mm)	Mode (Mm)	Maximum (Mm)
0.0	14.4	10.3	25.9
1.65	15.7	12.4	27.8
2.48	17.8	13.7	34.8
3.30	19.2	11.7	36.3
4.95	23.0	19.9	38.1
6.60	26.7	18.5	47.3

Table 6.3: Mean, mode and maximum values of the characteristic length of the tiles for various degrees of smoothing.

and can be considered as a tessellation. However, it is a tessellation wherein there is no a priori known geometric relation between the tiles. Hagenaar, Schrijver & Title (1997) report the interesting result that the tiles admit a tessellation that resembles Voronoi tessellation.

Often optimization is accompanied by a priori constraints on the independent variables. One constraint used by us involves tests to check for tiles that are reasonably large to be counted as supergranules (section 6.4).

The topology of the minimum can often be complicated: for example, a local maximum due to wall-element can induce a ring shaped minimum around it. The algorithm described above follows the steepest gradient from a point until it reaches a minimum. The presence of adjacent equal-valued

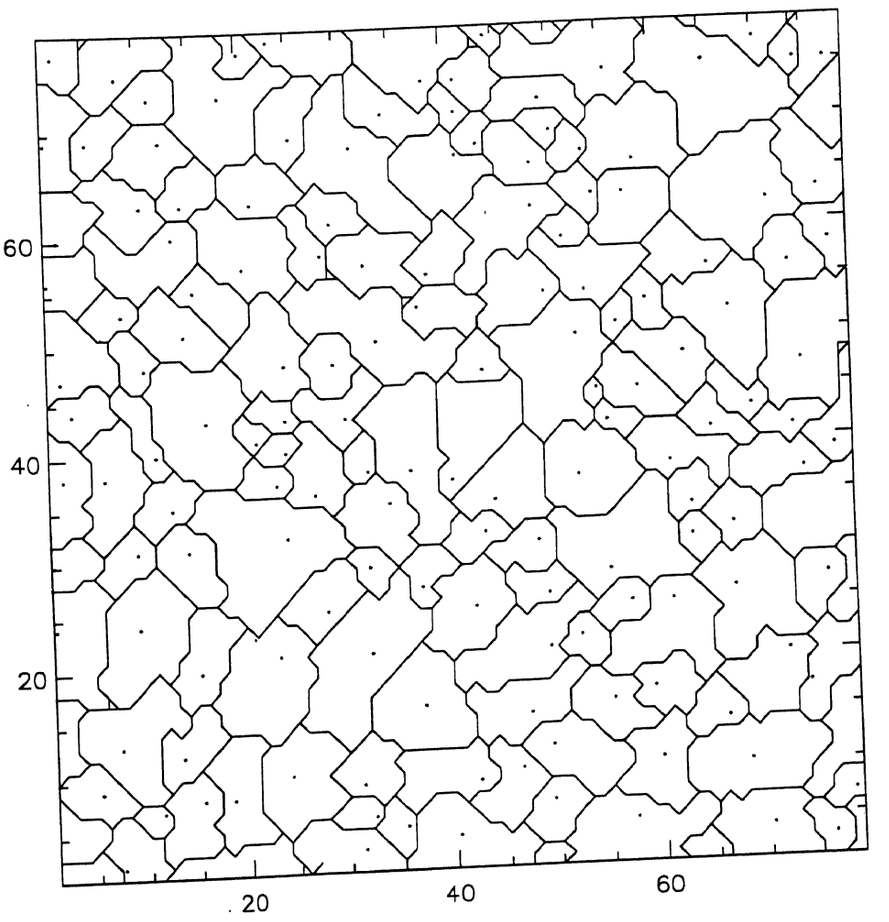

Figure 6.2: Tessellation of the chromosphere in units of 2.3 Mm, the pixel size. The mean size of the tiles is about 14 Mm. The dot within each tile is the "nucleus", or point of minimum intensity, within the tile, to which the minimization algorithm converges.

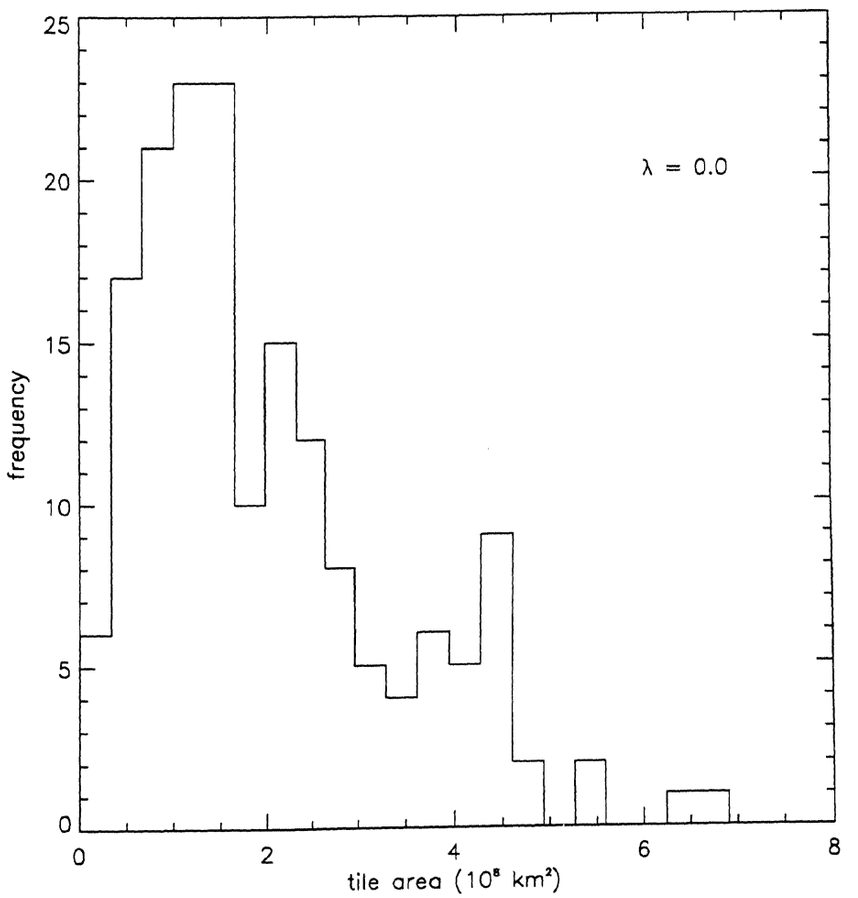

Figure 6.3: Area distribution of tiles extracted from a 264″ × 264″ unsmoothed image. λ is the FWHM of the smoothing Gaussian used to treat the image before tessellation.

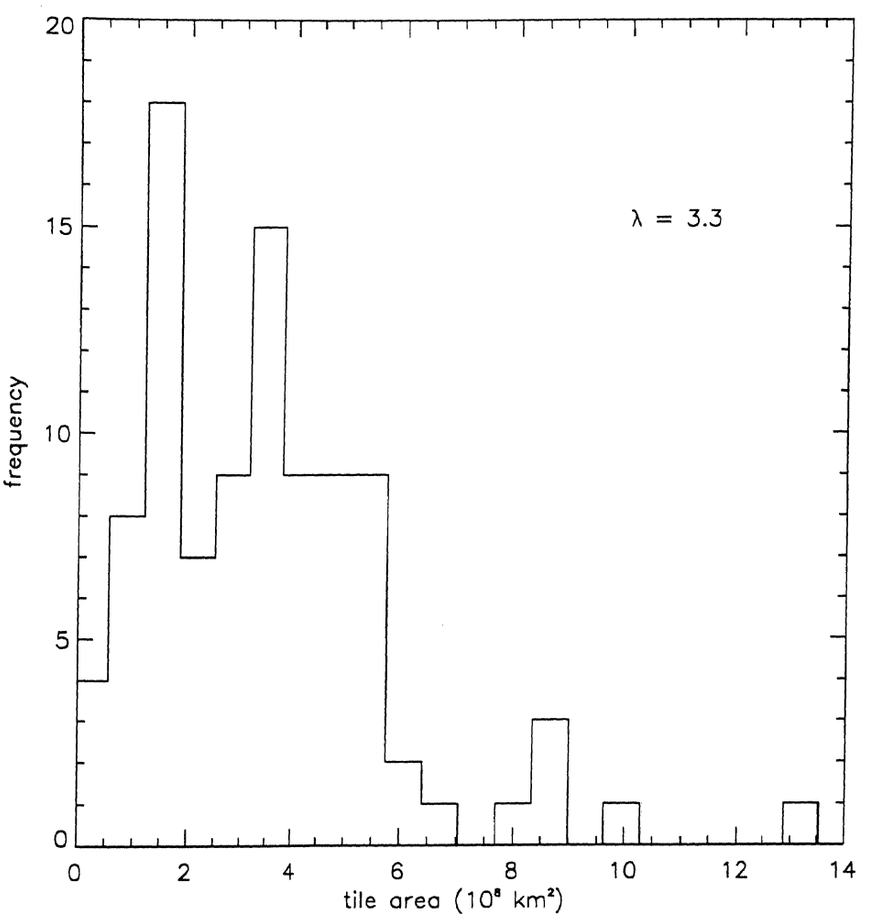

Figure 6.4: Area distribution of tiles for the same region as Fig 6.3 but smoothed with a Gaussian of FWHM given by $\lambda = 3.3''$

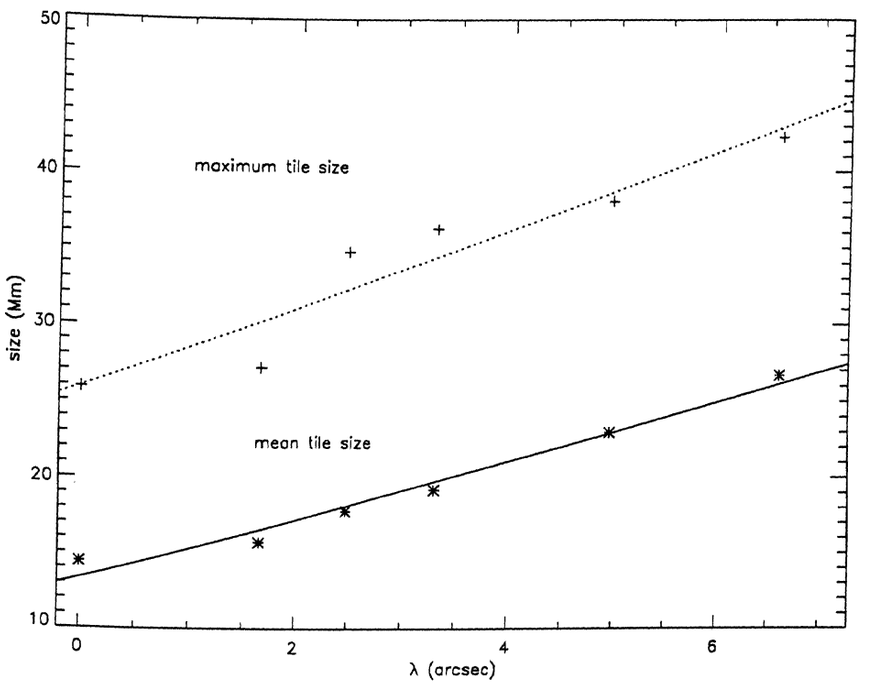

Figure 6.5: Result of smoothing on the mean and maximum tile length-scales. The mean values are indicated by asterisks and the maximum values by plus-signs. The solid and dashed lines are least squares fits to the mean and maximum length-scale data, respectively.

pixels at the minimum was not taken into account. This is done after the first step of tiling stage, when adjacent minimum pixels are connected, and the tiles centered on these minima are merged into a single tile. The position of the nucleus is taken as the average of the positions of the connected minima.

6.5 Effect of smoothing

A typical tessellation of the chromosphere is given in Fig 6.2 for a 264 × 264 QS window is given. The tiles are about 14 Mm in mean size. The spots

Gaussian FWHM (″)	skewness	kurtosis
0.0	0.62	3.17
1.65	0.46	2.63
2.48	1.09	5.61
3.30	0.84	4.98
4.95	0.83	3.26
6.60	0.66	3.23

Table 6.4: Skewness and kurtosis of the distribution of tile areas for various degrees of smoothing.

within the tiles are the points of convergence, or nuclei.

The distribution properties of the cells were studied under various degrees of smoothing. Smoothing was effected by convolving with Gaussians. The behaviour of the tiles under smoothing can shed light on the identity of cells vis-a-vis CNCs. In Figs 6.3 and 6.4, we give tile area distribution for $\lambda = 0$ and 2.5″, respectively, where λ is the FWHM of the smoothing Gaussian.

The results for mean, mode (most probable) and maximum area of the tiles for $\lambda = 0$, 1.65, 2.48, 4.95 and 6.60 are listed listed in Table 6.3.

From Table 6.3 it is evident that the maximum and mean of the length-scales of the tiles increase monotonically with smoothing. The increase of mode is not monotonic, with dips seen at $\lambda = 3.2'', 6.4''$, which are probably

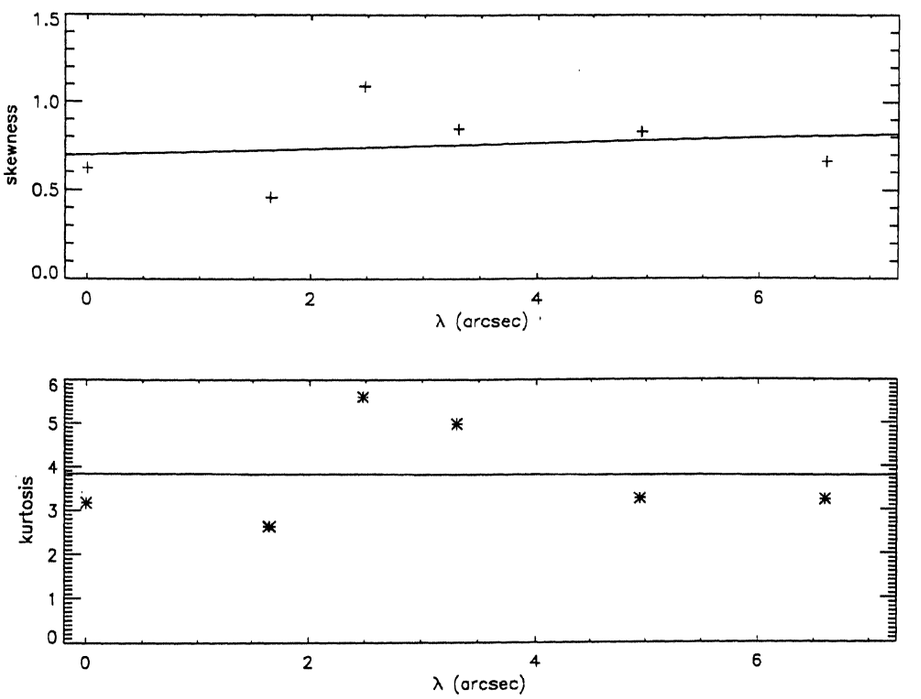

Figure 6.6: Result of smoothing on the skewness and kurtosis of the area distribution of the tiles in the quiet Sun. The solid lines are respective least square fits. An invariance of the form of the distribution function of the tile area is suggested by the almost zero slope of the fit.

scatters. A plot of mean and maximum length-scale of the tiles, extracted from Table 6.3, is given in Fig 6.5. Smoothing involves a local redistribution of intensity. As λ increases, features with small intensity excess over the background are lost. Usually, they are small scale structures, which merge into larger ones, with greater intensity contrast. As λ increases, larger structures are merged. This accounts for the increase in the mean, mode and maximum area of the resulting tiles.

The skewness (asymmetry about mean) and kurtosis (peakedness at

mean) of the distributions of tile areas for 5 values of λ are summarized in Table 6.4.

A plot of skewness and kurtosis of the area distribution of the tiles, extracted from Table 6.4, is given in Fig 6.6. The kurtosis shows considerable swing but on the whole its value appears to be constant; skewness, too, remains more or less constant. Interestingly, the mean value of skewness and kurtosis for the above data is not far from those of actual cells given in Table 5.8, namely $\alpha_3 = 0.65$ and $\alpha_4 = 3.34$. This appears to confirm the result of Hagenaar, Schrijver & Title (1997) that the distribution of the tiles remains invariant under smoothing.

The invariance could be attributed to the fact that as λ increases, the merger of cells proceeds in a linear way, as suggested by Fig 6.5. From Eq. 5.9, it is evident the distributional character of random variable X is not affected under linear transformations:

$$Y = aX + b \tag{6.1}$$

Under transformation (6.1), both skewness and kurtosis remain unchanged. Thus, Eq. (6.1) is a sufficient condition for the invariance of functional form of a distribution. In the present context we take the tile length-scales of the unsmoothed scales to be the basic random variable and the tile scales of the smoothed images to be random variables derived as function of it. The smoothing parameter λ defines the functional transformation. In other words, we have to determine $a = a(\lambda)$ and $b = b(\lambda)$. The mean size of the tiles can be used to estimate them. In Fig 6.5 we find that the slope of the mean area of the tiles is given by:

$$L_{mean} = 6.4\lambda + 13.3. \tag{6.2}$$

Thus, mean L in the absence of smoothing is 13.3 Mm, which is close to the actual value of 14.4 Mm given in Table 6.3. Accordingly, we estimate that $a = 1$ and $b = 6.4\lambda$ in Eq. 6.1. The self-similarity of the distribution

functions for the tile scales under smoothing is thus due to fact that as smaller tiles merge with bigger ones under smoothing in a linear fashion.

6.6 Physical significance of the tiles.

We ask the question: are the tiles identical to CNCs? If we do identify them as such, then according to Table 6.3, we are led to associate the mean value of 14.4 Mm as a typical value of CNCs and thus SGs (Hagenaar, Schrijver & Title 1997). They conclude that the true value of SGs should lie in the range 13 Mm–18 Mm.

One reason that weakens the case for this identification is that the tiles appear in the entire range of sizes from close to 0 to 30 Mm and higher. The mean value of 14.4 Mm is lowered by contributions to the average from these ultra-low size tiles. Some of these tiles easily fall into the mesogranular and granular size ranges (by definition). Thus, it seems unlikely that tiles sizes can be associated with CNC sizes in general. Furthermore, there are a number of measurements of SG and CNC obtained by direct visual inspection, such as in Chapter 3, that corroborate the traditional value of ~ 30 Mm.

Part of the aim of the morphological study discussed in chapter 3 was to measure cell sizes by direct visual inspection, in order that complications arising from the uncertainty of interpretations of more sophisticated methods be avoided. The smallest size measured was 17.1 Mm, but the average was as high as 26.1 Mm, which is closer to the traditional value of 30 Mm.

In Fig 6.7, a well-defined visually inspected CNC is superposed as a dashed line onto the tessellation obtained from a window in which it is present. The window is $59'' \times 74''$ in size. The cell has an area 6.4 $\times 10^8$ km^2, while tile M, the largest tile in the figure, has an area of 5.3 $\times 10^8$ km^2. It is evident that no tile is coincident with the cell. Yet, it wholly contains none of them, nor do any of the tiles wholly enclose the cell. The cell overlaps considerably 4 large tiles H, M, L and E.

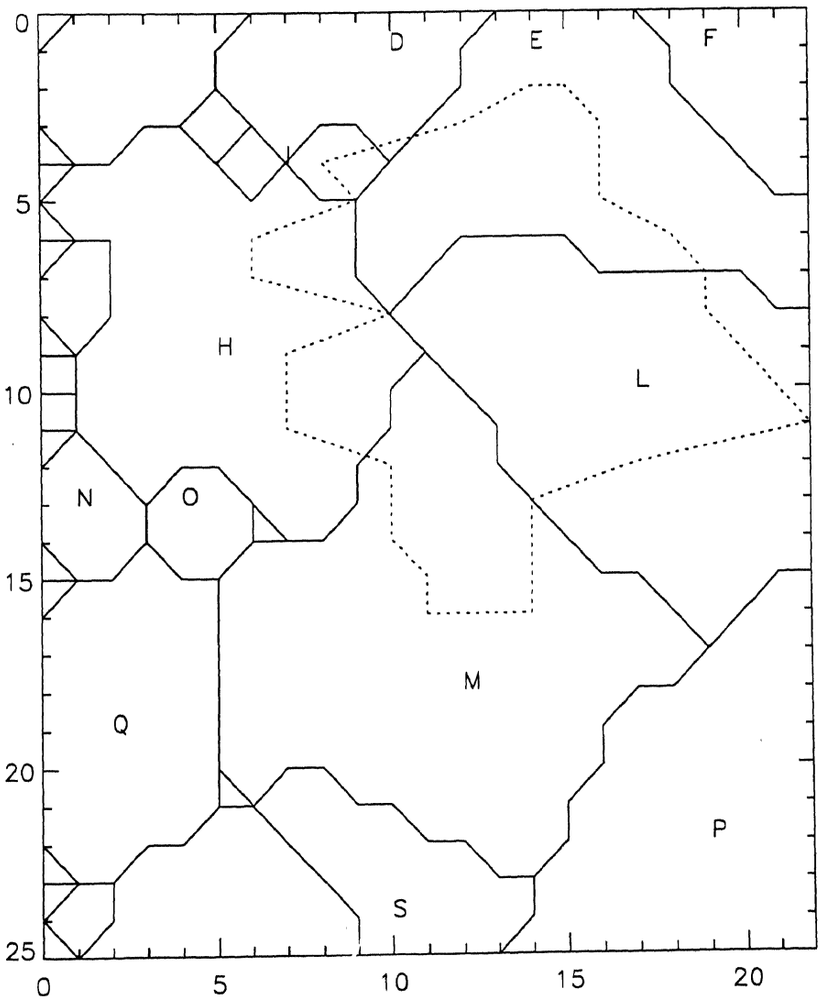

Figure 6.7: Outline of a QS cell as a dotted line superposed on the tessellation pattern. The window is 57″ x 48″ in size. The tiles are labelled at the position of their nuclei. We note that none of the tiles coincide with the cell. Minima of tiles that fall outside the box are not marked.

No	charactistic cell length (Mm)	AC on image (Mm)	largest tile size (Mm)	mean tile size (Mm)
1	21.7	23.0	16.6	11.4
2	25.2	27.6	23.1	13.2

Table 6.5: Comparative tile- and cell-scales from two windows containing a single complete cell.

Upon closer examination, it turns out that the tiles tend to coincide with wall-elements, which are diffuse lumps of local intensity enhancement along the cell wall. Although the tiles are essentially centered around minima and not maxima, the complexity of the intensity landscape and the nature of the tile clustering algorithm may produce maxima centered tiles as a side effect. This apprears to be the case with the lumps, which are local maxima and tend to induce local minima around them. These minima are then clustered into a single tile in this algorithm. As a result, one can have a maximum in a tile surrounded by minima. The actual cell showed 5 discontinuous lumpy wall-elements, that are clearly brought out by the contour plot in Fig 6.8, labelled A, B, C, D and E. A line drawn through these five contour "cells" represents the cell. Roughly speaking, the contour cells A, B and E in Fig 6.8 correspond respectively to the tiles H, M and E in Fig 6.7, while contour cells C and D correspond to tile L. The data for two cells is given in Table 6.5. Here characteristic length of the cell is the square root of its area; similarly, the tile sizes in columns 4 and 5 are obtained as square roots of the respective areas.

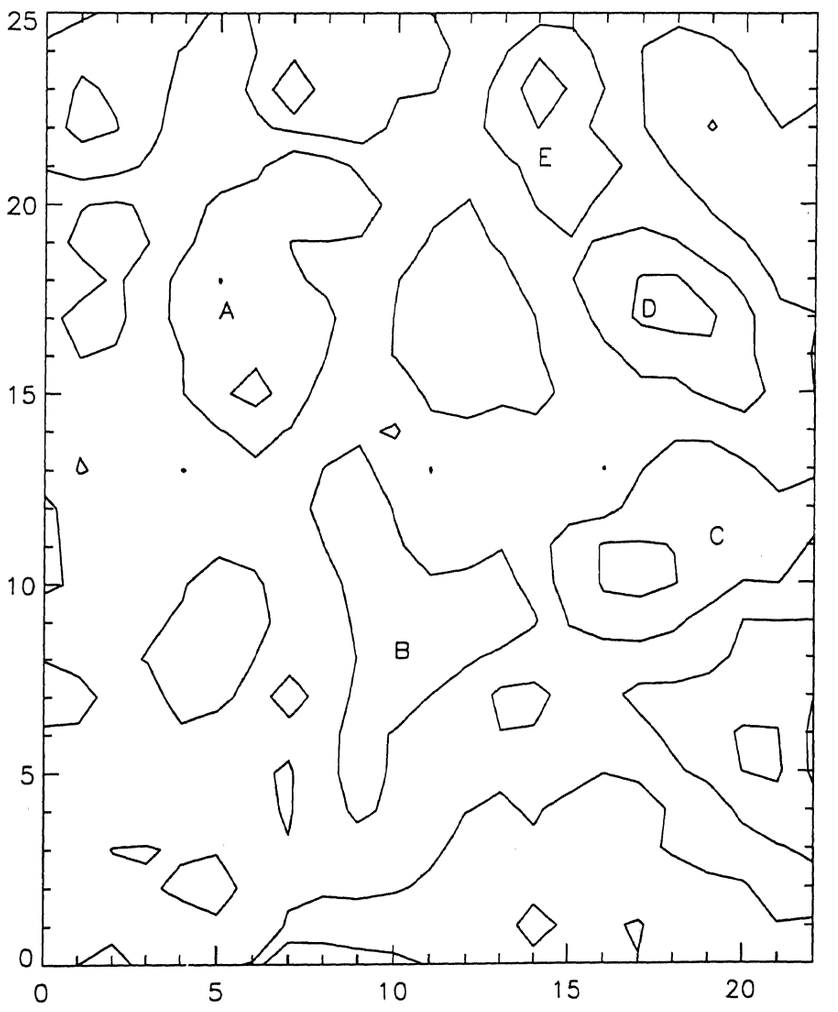

Figure 6.8: Contour plot of the window tiled in Fig 6.7. The clumps labelled A, B, C, D and E enclose the cell.

Further corroboration of this comes from Wang's report that the size of the magnetic elements is about 14 Mm, which is close to the average length-scale of the tiles. Moreover, the strong dispersion seen in tile length-scales is compatible with wide range of AC sizes observed in magnetogram data (Kömle 1979).

Fig 6.7 makes it clear that there are a number of small tiles that do are not CNCs themselves. They are local minima at lower scales than SG scales. Nonetheless, they bring down the mean area of the tiles, as evidenced by Table 6.5. It is worth noting that the presense of BPs and cell wall discontinuities can produce local maxima and minima at scales smaller than cell sizes (Chapter 3). Their identity as sub-cellular structures is evident under visual inspection. But, an algorithm that tessellates the chromosphere into basins of intensity may not identify them as such, but instead treat them as local minima at par with actual cells. The actual number of such undesired local minima will depend on the particular tiling algorithm chosen.

Hagenaar, Schrijver & Title (1997) attribute the discrepancy between the tile size and AC size to the fact that AC picks up the signal from the largest tile length-scales. Yet this does not appear to be the case, since, according to Table 6.5, the AC size is in both cases *larger* than the largest tiles in the image. We suggest that tile scales are not reflected in AC for the same reason that flocculi scales are not reflected in image AC. If the flocculi had been arbitirarily distributed, then AC would have returned flocculi scales. Instead, flocculi are distributed in a systematic manner at the borders of cells. Since the tiles follow the floccular pattern, it is not surprising that they their clustering property brings out SG or CNC scales.

Chapter 7

Concluding remarks

7.1 Summary

Morphological and dynamical properties of the chromospheric network cells have been studied using a 107 hr time-series of Ca II K images from Antarctica and also spectroheliograms from Kodaikanal solar observatory. Because the network cells are, as is commonly believed, manifestations of convective phenomena, they can shed light on the physical conditions in the convection zone of the Sun. Analytical tools such as autocorrelation to study scales, cross-correlation to study lifetimes, and a method of tessellation to study the intensity landscape of the chromosphere, have been used.

The possible relations between length-scales, lifetimes and magnetic fields have been studied. It is shown that shape and intensity contrast of cells show a dependence on cell scales. A latitude dependence of cell sizes is observed which is explained in terms of magnetic and rotational effects. Lifetime of cells shows a strong dependence on activity level, which is explained in terms of lower diffusion rate in more active regions. The relation between life and size of CNCs is deduced using the statistical technique of comparing their respective distribution functions. It is shown that diffusion mechanism in the cells can explain the observed relation.

Properties of the tiles obtained by tessellating the chromosphere using the Steepest Descent method have been studied. It is suggested that the tiles thus obtained correspond not to cells but to substructures of the cell, such as wall-elements.

7.2 Future works

Some of the morphological studies not requiring a long time-series of data, such as relations between size, shape and intensity contrast, may be repeated for a larger number of cells, using higher resolution data than the Antarctica data.

The evolution of cell shapes, size and temperature contrast during the evolution of cells is a problem that can be addressed using the Antarctica data. Similarly, also tessellation pattern can be studied. Diffusion rate in different kinds of cells needs to be studied directly using high spatial and temporal resolution velocitygrams obtained from satellites such as SOHO.

The undulations observed in the cross-correlation function needs to be investigated. Out preliminary investigations show that the undulations may not be of atmospheric or instrumental origin. Some issues to be taken up are: if the undulations are indeed intrinsic, what is the exact physical change that produces them? Finally, a theoretical explanation of the effect will be needed.

References

[1] Antia, H, M., Chitre, S. M.: 1979, Sol. Phys., 63, 67.

[2] Bahng, J. & Schwarzschild, M.: 1961, ApJ, 134, 312).

[3] Bappu, M. K. V.: 1967, Sol. Phys., 1, 151.

[4] Biermann, L.: 1946, Z. Astrophysik, 25, 161.

[5] Böhm-Vitense, E.: 1958, Zeit. Astrophys., 46, 108.

[6] Brandt, P. N., Scharmer, G. B., Ferguson, S., Shine, R. A., Tarbell, T. D., Title, A. M.: 1988, Nature, 335, 238.

[7] Bray, R. J., Loughead, R. E., & Durrant, C. J.: 1984, *The Solar Granulation*, 2nd ed., (Cambridge).

[8] Brune, R., & Wöhl, H.: 1982, Sol. Phys., 75, 75.

[9] Chandrasekhar, S: 1961, *Hydrodynamic and hydromagnetic stability*, Claredon Press (Oxford).

[10] Clark, A., Johnson, H. K.: 1967, Sol. Phys., 2, 433.

[11] Durrant, C. J., Mattig, W., Nesis, A., Reiss, G., & Schmidt, W.: 1979, Sol. Phys., 61, 251.

[12] Duvall, Jr., T. L.: 1980, Sol. Phys., 66, 213.

[13] Engvold, O: 1967, Sol. Phys., 2, 234.

[14] Frazier, E. N.: 1974, Sol. Phys., 38, 69.

[15] Giovanelli, R. G.: 1980, Sol. Phys., 67, 211.

[16] Hagenaar, H. J., Schrijver, C. J., & Title, A. M.: 1997, ApJ, **481**, 988.

[17] Hart, A. B.: 1954, MNRAS, 114, 17.

[18] Hart, A. B.: 1956, MNRAS, 116, 38.

[19] Harvey, K. L.: 1994, in R. J. Rutten & C. J. Schrijver (eds.) *Solar surface magnetism*, Kluwer Academic Publishers.

[20] Hoel, P. G.: 1971, *Introduction to Mathematical Statistics* (John Wiley & Sons).

[21] Howard, R.: 1991, Sol. Phys., 135, 327.

[22] Howard, R., & LaBonte, B. J.: 1981, Sol. Phys., 74, 131.

[23] Janssens, T. J.: 1970, Sol. Phys., 11, 222.

[24] Jordan, S. D.: 1981, *The Sun as a star*, ed. S. D. Jordan (NASA: monograph series on nonthermal phenomena in stellar atmospheres).

[25] Kalkofen, W.: 1990, ed. P. Ulmschneider, E. R. Priest, R. Rosner, *Mechanisms in chromospheric and coronal heating* (Springer Berlin 1990).

[26] Kömle, N: 1979, Sol. Phys., 64, 213.

[27] Krishnakumar, V., & Venkatakrishnan, P.: 1998, submitted to Solar Physics.

[28] Lebovitz, N. R.: 1966, ApJ, 146, 946.

[29] Leighton R. B.: 1964, ApJ, 140, 1547.

[30] Leighton, R. B., Noyes, R. W. & Simon, G. W.: 1962, ApJ, 135, 474.

[31] Linsky, J. L., & Avarett, E. H.: 1970, PASP, 82, 169.

[32] Livi, S. H. B., Wang, J., & Martin, S. F.: 1985, Australian J. Phys., 38(6), 855.

[33] Mein, N., & Mein, P.: 1980, A&A, 84, 96.

[34] Muller. R.: 1989, in R. J. Rutten & G. Severino (eds.), *Solar and stellar granulation*, Kluwer Academic Publications.

[35] Muller, R., & Roudier, Th.: 1994, Sol. Phys., 152, 131.

[36] Münzer, H., Schröter, E. H., Wöhl, H., and Hanslmeier, A.: 1989, Sol. Phys. 213, 431.

[37] Namba, O., & Diemel, W. E.: 1969, Sol. Phys., 90, 205.

[38] November, L. J., Toomre, J., Gebbie, K., & Simon, G. W.: 1979, ApJ, 227, 600.

[39] November, L. J., Toomre, J., Gebbie, K., & Simon, G. W.: 1981, ApJ, **243**, L123.

[40] Oda, N: 1984, Sol. Phys., **93**, 243.

[41] Pap, J.: 1992, A&A, **264**, 249.

[42] Raghavan, N.: 1983, Sol. Phys., 89, 35.

[43] Raju, K. P., Srikanth, R., & Singh, J.: 1998a, Sol. Phys., 178, 251.

[44] Raju, K. P., Srikanth, R., & Singh, J.: 1998b, Sol. Phys., in press.

[45] Rogers, E. H.: 1970, Solar Phys., 13, 57.

[46] Rogerson, J. B.: 1955, ApJ, 121, 204.

[47] Shaviv, G., & Salpeter, E. E.: 1973 ApJ, 184,191.

[48] Simon, G., Leighton, R. B.: 1964, ApJ, 140, 1120.

[49] Simon, G., Title, A., Topka, K. P., Tarbell, T., Shine, R. A., Ferguson, S. H., & Zirin, H., and the SOUP team: 1988, ApJ. bf 327, 964.

[50] Singh, J. & Bappu, M. K. V.: 1982, Sol. Phys., 71, 161.

[51] Singh, J., Nagabhushana, Babu, G. S. D., and Wahabuddin: 1994 Sol. Phys., 153, 157.

[52] Singh, J., & Prabhu, T. P.: 1985, 97, 203.

[53] Sivaraman, K. R.: 1990, eds. P. Ulmschneider, E. R. Priest, R. Rosner, *Mechanisms in chromospheric and coronal heating* (Springer Berlin 1990).

[54] Sivaraman, K. R., & Livingston, W. C.: 1982, Sol. Phys. 80, 227.

[55] Sivaraman, K. R., Singh, J., Bagare, S. P., Gupta, S. S: 1987, ApJ, 313, 456.

[56] Skochilov, V. G. & Teplitskaya. R. B.: 1997, Sol. Phys., 173, 275.

[57] Stein, R. F., & Liebacher, J.: 1974, Ann. Rev. Astron. Astroph. 12, 407.

[58] Smithson, R. C: 1973, Sol. Phys., 29, 365.

[59] Spiegel, M. R.: 1980, *Probablity and Statistics*, Schaum's Outline series (McGraw-Hill).

[60] Stenflo, J. O.: 1973, Sol. Phys., 32, 41.

[61] Stenflo, J. O.: 1988, Astroph. Space Sci., 144, 321.

[62] Schwarzschild, M.: 1948, ApJ, 107, 1.

[63] Sýkora, J.: 1970, Sol. Phys., 71, 161.

[64] Title, A., Tarbell, T., Topka, K., Ferguson, S., Shine R., & the SOUP team: 1986, ApJ, **336**, 475.

[65] Venkatakrishnan, P.: 1986, Nature, 322, 156.

[66] Vernazza, J. E., Avrett, E. H., & Loeser, R.: 1981, AJ (Suppl.), 45, 635.

[67] Wiehr, E.: 1978, A&A 69, 279.

[68] Wang, H.: 1988a, Sol. Phys. 116, 1.

[69] Wang, H.: 1988b, Sol. Phys. 117, 343.

[70] Wang, H., & Zirin, H.: 1988, Sol. Phys. 115, 205.

[71] Worden, S. P.: 1975, Sol. Phys, 45, 521.

[72] Worden, S. P., & Simon, G. W.: 1976, Sol. Phys, 46, 73.

[73] Zirin, H.: 1987, Sol. Phys. 110, 101.

[74] Zirin, H.: 1988, The Sun (Cambridge).

[75] Zwaan, C.: 1978, Sol. Phys., 60, 213.